COMBINED LASER, ULTRASOUND, AND ELASTICITY IMAGING FOR COMPREHENSIVE DIAGNOSIS OF CANCER

A Dissertation
Presented to
The Academic Faculty

by

Heechul Yoon

In Partial Fulfillment
of the Requirements for the Degree
Doctor of Philosophy in the
School of Electrical and Computer Engineering

Georgia Institute of Technology
December 2018

COMBINED LASER, ULTRASOUND, AND ELASTICITY IMAGING FOR COMPREHENSIVE DIAGNOSIS OF CANCER

Approved by:

Dr. Stanislav Y. Emelianov, Advisor
School of Electrical and Computer Engineering
Georgia Institute of Technology

Dr. Omer T. Inan
School of Electrical and Computer Engineering
Georgia Institute of Technology

Dr. F. Levent Degertekin
School of Electrical and Computer Engineering
Georgia Institute of Technology

Dr. Costas D. Arvanitis
Department of Mechanical Engineering
Georgia Institute of Technology

Dr. Brooks Lindsey
School of Electrical and Computer Engineering
Georgia Institute of Technology

Date Approved: 12 October 2018

ACKNOWLEDGEMENTS

First, I would like to thank my advisor, Dr. Stanislav Emelianov, for his thoughtful support and guidance. He has been always supportive to students including me, which was the most significant factor that I was able to keep pursuing my research.

I was truly lucky that I had a chance to become a member of the Ultrasound Imaging and Therapeutics Research Laboratory. Everyone in the lab was diversely knowledgeable, passionate, willing to help others, and creative. I am sure that without their help, I would not complete my research.

I would like to thank my thesis committee members, Dr. F. Levent Degertekin, Dr. Brooks Lindsey, Dr. Omer T. Inan, and Dr. Costas D. Arvanitis for their fruitful feedback on my research. Due to their effort, my depth of knowledge on my research has been improved.

Especially, I would like to thank my family for their endless and unconditional support throughout my journey. My wife, Sooyeon Lee, had to take care of two students in our family; one is our son Hyunkyu Yoon and the other is myself. Without her love and support, I would not finish my research for sure. I also would like to thank her parents' long-distance support from Korea. I would like to thank my sister and her husband who luckily lived close to us and were always helpful. Lastly, I would like to thank my parents who have always wished me good health, happiness, and success.

TABLE OF CONTENTS

LIST OF TABLES

LIST OF FIGURES

SUMMARY

As cancer is pathologically and biologically complex, identifying a variety of information on its morphology, functionality, molecular composition, and biomechanics is desired for precise and personalized diagnosis and treatment. Medical ultrasound imaging is a relatively safe, cost-effective modality that provides a cross-sectional image of anatomy in real-time, but it suffers from low contrast and does not provide quantitative functional information on tissue for better detection and assessment of a suspicious lesion. To circumvent this limitation, researchers have introduced shear-wave elasticity imaging, which noninvasively measures Young's modulus of tissue, spectroscopic photoacoustic imaging, which quantifies chromophores distribution in tissue, phase-change contrast agents, which are useful in imaging extravascular targets, and super-resolution imaging, which provides unprecedented spatial resolution beyond the diffraction limit for molecular imaging. This research engineers these methods to further improve their respective imaging capabilities. In addition, based on the improvements in each imaging method, this research introduces combined laser, ultrasound, and elasticity (CLUE) imaging that is uniquely capable of simultaneous and synergistic probing of acoustic, optical, and mechanical imaging contrast of tissue to provide comprehensive soft tissue assessment.

CHAPTER 1. INTRODUCTION

1.1 Cancer and Medical Imaging

Cancer is a major cause of death in the United States. In 2017, nearly one of every four Americans are expected to die of cancer, which is surpassed only by heart disease [1]. Early diagnosis and timely management of cancer is known to improve survival rates. Researchers have developed various medical imaging techniques, which have played an essential role in the detection, diagnosis, and treatment of cancer [2]. However, as cancer progresses, it undergoes complex pathological and biological changes. Thus, precise diagnosis and personalized treatment of cancer necessitates a variety of information on its morphology, functionality, molecular composition, and biomechanics [3-5]. It is desirable to gauge all of these various aspects of cancer to improve its detection, staging, treatment, and management [2, 6].

However, none of the currently used stand-alone biomedical imaging modalities provides this broad information on cancer, which has led to the development of hybrid or multi-modal approaches [2, 7, 8]. For example, a combination of positron emission tomography (PET) and computed tomography (CT) referred to as PET/CT synergistically complement each other, as PET offers metabolic contrast that can be superimposed on the superior anatomical visualization of CT. However, nuclear medicine-based imaging techniques are hamstrung by their reliance on the use of ionizing radioisotopes for contrast.

Ultrasound (US) is a safe, noninvasive, real-time, portable, and cost-effective imaging modality. Thus, as a first-line screening tool, US imaging has been widely used in

the clinic to aid detection of cancers, such as breast, liver, thyroid, prostate cancer and others [9-13]. However, its sensitivity and specificity to cancerous tumors are relatively low compared to other imaging modalities, as the acoustic properties of a tumor and its surrounding tissue are similar [9]. Furthermore, US imaging is often operator dependent [14]. To address these limitations, various US-based imaging methods, including shear-wave elasticity imaging (SWEI), spectroscopic photoacoustic (sPA) imaging, and contrast-enhanced US imaging, have been rigorously investigated to provide mechanical, molecular, and functional images of cancer, supplementing the anatomical information given by traditional gray-scale B-scan images [15-19].

1.2 Ultrasound-based Imaging Techniques

This sub-chapter introduces various ultrasound-based imaging techniques including SWEI, sPA imaging, and US imaging with contrast agents that could be respectively useful in characterizing a tumor in different perspectives.

SWEI can quantify elastic properties of tissue noninvasively. As the pathological condition of cancer is closely related to its stiffness in many solid lesions, SWEI has shown great potential in differentiating benign and malignant tumors [20-22]. In principle, SWEI relies on shear waves generated by the application of acoustic radiation force (ARF). The propagation of the shear waves is then observed to estimate their velocity, as a shear-wave velocity (SWV) is associated with the shear modulus of tissue. Since SWEI was introduced by Sarvazyan *et al.* [23], many related methods have been developed to improve SWEI [24-28]. Furthermore, SWEI has been applied to several clinical applications, showing promising capabilities in cancer diagnosis and monitoring [20, 29, 30]. In addition, the

mechanical heterogeneity of cancer, which can be visualized by SWEI, is of interest, as it could indicate the malignancy of the tumor [31].

Photoacoustic (PA) imaging offers optical contrast from endogenous and/or exogenous absorbers in tissue based on the PA effect, creating acoustic signals in response to pulsed-laser irradiation and subsequent thermal expansion [32-34]. For example, hemoglobin in blood is a strong absorber providing adequate PA signals compared to other surrounding chromophores; Thus, hemoglobin contrast from PA has been used to identify the formation of vessels surrounding a tumor, as the structural complexity of tumor neovasculature is often an indicator of tumor malignancy [35]. Furthermore, the level of blood oxygen saturation (SO_2), the ratio of oxygenated to total hemoglobin concentrations, is known to be highly associated with the pathological state of a tumor [36, 37]. Multi-wavelength (i.e., spectroscopic) PA imaging, also referred to as sPA imaging, can estimate quantitative concentrations of multiple chromophores, and oxygenated and deoxygenated hemoglobin have unique optical absorption spectra. Thus, sPA imaging has been widely studied to measure the SO_2 level in tumors. Malignant tumors and metastatic sentinel lymph nodes have been shown to have a lower level of SO_2 compared to normal tissue [38-43].

Microbubbles are a clinically-approved contrast agent widely used in the clinic, as they provide superior contrast over traditional gray-scale US images [44-47]. Pulse inversion-based methods are typically used to detect the nonlinear response of microbubbles to an applied acoustic field. Recently, to further expand the utility of microbubbles, sub-micrometer-sized phase-change contrast agents that can form microbubbles *in situ* in response to an acoustic or optical trigger (i.e., perfluorocarbon

nanodroplets) have been introduced [48-53]. Because of their relatively small size, they have the potential to extravasate from endothelial fenestrations in cancer neovasculature and are thus capable of imaging extravascular targets. Our group and others have focused on optically-triggered perfluorohexane nanodroplets (PFHnDs) that can repeatedly vaporize and recondense, providing repeatable high-contrast PA and US signals [52, 54-56]. These agents have shown great potential in contrast-enhanced imaging and super-resolution imaging for lymph node localization and brain vasculature mapping. High-frame-rate US imaging is typically required to capture the temporal response of the PFHnDs because their vaporization and recondensation process is transient and stochastic [57].

1.3 Research Goals

Traditional ultrasound B-mode images can provide real-time morphological information of tissue with excellent spatial resolution at great depths noninvasively, which helps physicians to identify various tissue abnormalities [58]. However, because the contrast of ultrasound imaging is relatively low, accessing anatomical information of the tissue is not always enough to detect and characterize many complex diseases, such as cancer.

SWEI, sPA imaging, contrast-enhanced ultrasound imaging, and super-resolution ultrasound imaging are emerging ultrasound-based imaging techniques capable of quantifying mechanical, functional, and molecular signatures of tissue noninvasively. Thus, the overall goals of this research are 1) to further advance these emerging imaging methods to improve their respective imaging capabilities, and 2) to develop an imaging

platform and imaging sequence capable of combining all of these imaging methods that can be potentially used for comprehensive diagnosis of cancer.

CHAPTER 2. DUAL-PHASE TRANSMIT FOCUSING FOR MULTIANGLE COMPOUND SHEAR-WAVE ELASTICITY IMAGING

Shear-wave elasticity imaging (SWEI) can assess the mechanical properties of tissue quantitatively and noninvasively. To obtain the superior quality of SWEI images, the effective generation of acoustic radiation force is essential. Consequently, various transmit beamforming and pulse-sequencing methods have been investigated. This chapter introduces a technique referred to as "multi-angle compound SWEI" (MAC-SWEI) using simultaneous multi-angular push beams created by dual-phase transmit focusing to further improve the efficiency of shear wave generation, and therefore, to increase the quality of SWEI. Dual-phase transmit focusing creates both main and grating lobes (i.e., multi-angular push beams for pushing) to adequately generate shear waves with multiple wave-front angles by applying two phases alternately on array elements. Then, the generated multi-angular shear waves propagating are separated by multi-directional filtering, enabling the reconstruction of corresponding multiple shear-wave velocity (SWV) maps. To form a single image with a full field-of-view (FOV), these maps are combined, while pushing regions are omitted. Overall, we developed and tested the MAC-SWEI method using Field II beam simulations and phantom experiments with a programmable ultrasound

imaging system. Our results suggest that MAC-SWEI with dual-phase transmit focusing may improve the quality and the reliability of elasticity maps.

2.1 Introduction

Reducing the number of push beam excitations while maintaining the image quality would be one of the remaining challenges in SWEI. For example, to reconstruct an SWV map with an entire FOV, multiple push beams should be applied subsequently at different lateral locations because the propagation of shear waves inside the push regions cannot be observed [21]. Moreover, the push beams applied on the stiff inclusion may result in overestimated SWVs [59]. However, the frame rate of SWV images is limited with this multiple push beam-based approach, which may cause motion artifacts resulted from physiological motion such as carotid artery pulsation, respiration, and cardiac activity [60]. In addition, the repeated generation of long push beams may raise safety concerns for patients, shorten the ultrasound transducer life time, and require a longer cooling time of the transducer [61, 62]. Therefore, fewer push events are desired.

This chapter aims to address these tradeoffs by introducing simultaneous multi-angular push beams. Specifically, in a single pushing and tracking event, by creating the shear waves of various wave-front angles, which can be separated by multi-directional filtering [63-65], we simultaneously obtain multiple SWV maps corresponding to shear waves with different orientations and propagating in different directions. Thus, similar to CUSE methods [27, 66, 67], our method applies multiple push beams simultaneously and creates multiple SWV maps through multi-directional filtering. However, we use multi-angular push beams instead of parallel push beams, to allow us to omit undesired regions, where the push beams are applied, before combining SWV maps. Furthermore, because of the angular compounding effect, we achieve the improved quality of SWV maps.

To effectively create simultaneous multi-angular push beams, we introduce a new transmit beamforming technique called "dual-phase transmit focusing," which alternatively applies two phases of ultrasound waves on every element of an array transducer. Dual-phase transmit focusing generates both main and grating lobes that can be as effective angular pushing beams. An overall imaging method that both uses simultaneous multi-angular push beams created by dual-phase transmit focusing and combines multiple SWV maps after eliminating undesirable SWV in the pushing regions, is referred to as "multi-angle compound SWEI" (MAC-SWEI). The developed MAC-SWEI approach, not only improves the quality of elasticity images because of angular compounding, but also suppresses overestimated SWV in the pushing regions, because MAC-SWEI can remove these unreliable regions before combining SWV maps.

2.2 Materials and Methods

2.2.1 Dual-phase Transmit Focusing for Multi-angular Pushing

Grating lobes, caused by the discrete nature of array transducers, obstruct the identification of the exact positions of targets and have been regarded as unwanted artifacts in ultrasound imaging [68]. If the spatial sampling distance of the array elements is not short enough, grating lobes appear in the imaging plane periodically as a function of the incident angles θ_{m} as

$$\sin\theta_m = m\frac{\lambda}{d}, \qquad m = \pm 1, \pm 2, \ldots \tag{1}$$

where λ is the wavelength of an ultrasound wave, d is the inter-element pitch (or spacing) of the transducer, and m represents the periodicity of the grating lobes [69, 70]. For example, if λ is 385 μm (i.e., if the sound speed of 1,540 m/s and the wave frequency of 4 MHz are assumed), and d is 300 μm (i.e., typical spacing in clinical linear array

transducers), the grating lobes are formed outside of the imaging FOV. Therefore, the ultrasound array transducer, operating within its typical frequency range, is designed to avoid the grating lobes. However, if the element spacing is doubled similar to the sparse-array techniques (i.e., if d becomes 600 μm) [70], then the incident angles of the first grating lobes (i.e., $m = \pm 1$) are about ±40° according to Equation 1, indicating that the sparse-array approach can create grating lobes within the FOV. However, the sparse-array approach suffers from significant loss in acoustic energy because it uses only half the number of elements when transmitting waves. More importantly, the relative magnitudes between grating lobes and a main lobe are not adjustable.

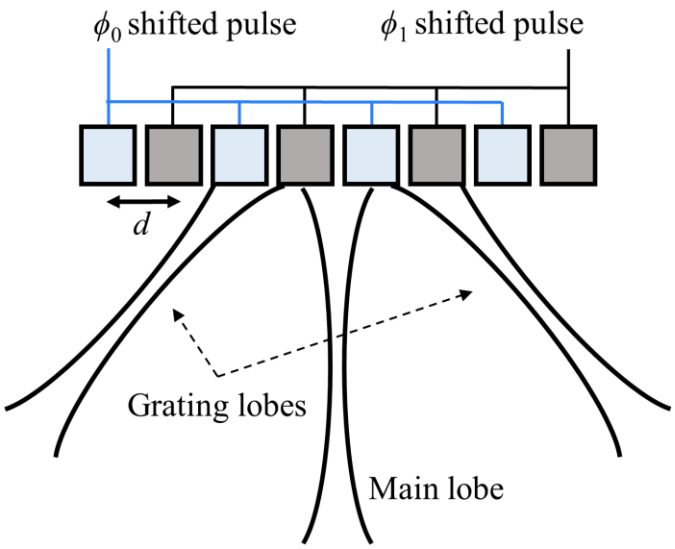

Figure 1 – Generation of multi-angular push beams using the dual-phase transmit focusing approach.

To generate multi-angular push beams adequately and simultaneously, we introduce an effective way of creating both grating lobes and a main lobe, referred to as "dual-phase transmit focusing." Unlike conventional focusing, which assigns the same phase on time-delayed transmit pulses to all array elements for coherent focusing, dual-phase transmit focusing alternatively applies two phase-shifted (by ϕ_0 and ϕ_1) push pulses on the transducer, as depicted in Figure 1. In other words, in dual-phase transmit focusing,

transmitted pulses are focused at the same focal point as in conventional focusing; however, the pulses have two different alternating phases (i.e., the phase is the same on every other element and there is a constant phase difference between two adjacent elements). As a result of this repetitive phase difference between two adjacent elements, dual-phase transmit focusing produces the grating lobes at the same angles and positions as the sparse-array technique does. However, unlike the sparse-array technique, dual-phase transmit focusing can adjust the magnitude of grating lobes, because the grating lobes become a function of the dual-phase difference. Thus, dual-phase transmit focusing enables the adequate generation of both main and grating lobes with equivalent magnitudes. Note that the phase difference in dual-phase transmit focusing only determines the magnitudes of the grating and main lobes. The incident angles of grating lobes (θ_m) are determined by Equation 1 and the focus of the grating lobes is determined by the focus of the main lobe.

Table 1 – Parameters used in the Field II simulation.

	Parameter	Value
Transducer (L7-4)	Element pitch (mm)	0.298
	Element width (mm)	0.250
	Element height (mm)	7.0
	Elevational focus (mm)	25
	−6dB bandwidth (MHz)	3.5 to 6.5
	Number of elements	128
Excitation pulse	Center frequency (MHz)	4.0
	Sampling frequency (MHz)	100
	Pulse duration (μs)	10
	Pushing Focus (mm)	20
	f-number	1.4
	Apodization	Hanning window
Medium	Attenuation coefficient (dB/cm/MHz)	0.5
	Speed of sound (m/s)	1,540
	Parameter	Value

According to the phase difference, defined as $\Delta\phi = |\phi_0 - \phi_1|$ and ranging from 0° to 180°, a variety of pushing configurations can be realized. For example, for $\Delta\phi = 0°$, because of the same phase applied to the push pulses, this configuration produces only the main lobe, as in the conventional pushing strategy. By contrast, if $\Delta\phi = 180°$, there is barely any amplitude of the main lobe at the focus because of the cancellation of two waves with opposite phases. Instead, we obtain two strong grating lobes. Overall, as $\Delta\phi$ increases from 0° to 180°, the magnitude of the main lobe decreases; however, the magnitudes of the two grating lobes increase, indicating that the magnitudes of the grating lobes and the main lobe can be adjusted based on the value of $\Delta\phi$. To assess dual-phase transmit focusing, we simulated acoustic fields using a Field II program [71, 72]. A transducer modeled for the simulation was the same as the linear array transducer used in experiments (L7-4, Philips Healthcare, Andover, MA, USA). All relevant simulation parameters are listed in Table 1. To evaluate the pushing ability of dual-phase transmit focusing, we obtained 181 fields with varying $\Delta\phi$ from 0° to 180° with 1° increment.

2.2.2 Multi-Angle Compound Shear Wave Elasticity Imaging

Through dual-phase transmit focusing, which effectively produces simultaneous multi-angular push beams, we implemented multi-angle compound SWEI (MAC-SWEI). Like other SWEI-based methods, MAC-SWEI also consists of three steps, shown in Figure 2: (1) pushing the tissue to generate shear waves, (2) tracking the propagation of shear waves, and (3) reconstructing and compounding SWV maps. The main difference between MAC-SWEI and other SWEI-based techniques is that MAC-SWEI employs grating and main lobes created simultaneously by dual-phase transmit focusing as pushing sources, generating the shear waves with various wave-front angles. Multi-directional filtering was used to separate these angular shear waves, leading to the reconstruction of corresponding individual SWV maps. Since we know the exact location of push regions and the fact that the SWV values in push regions have the potential to be unreliable, our method excludes

all SWV values in each push region before combining them. Thus, this approach can result in a reliable SWV map, spanning a full FOV in a single pushing and tracking event.

A programmable ultrasound research machine (Vantage 256^{TM}, Verasonics Inc., Redmond, WA, USA), equipped with the L7-4 linear array transducer (see Table 1) was used in this study. The ultrasound system was used to generate push pulses and to record post-beamformed IQ data. The acquired data were processed offline using MATLAB (The MathWorks Inc., Natick, MA, USA). To create the multi-angular push beams (one main and two left/right grating lobes), we applied $\Delta\phi$ of 140° for dual-phase transmit focusing. Additionally, we used $\Delta\phi$'s of 0° and 180° to analyze how the choice of $\Delta\phi$ affects the generation of shear waves.

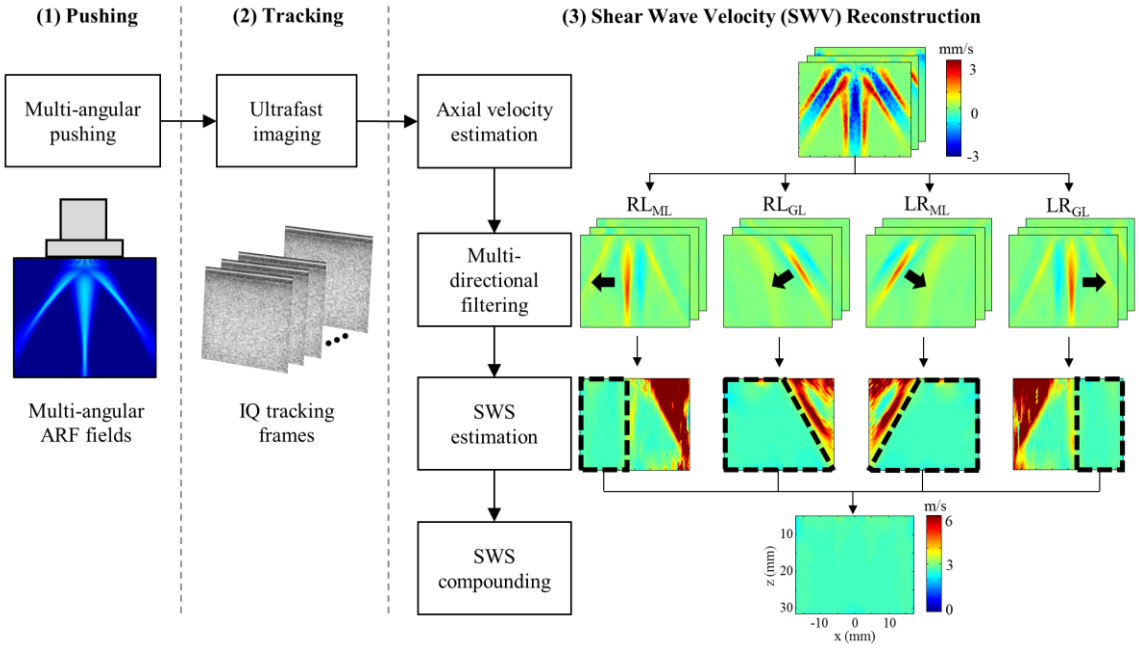

Figure 2 – Overall procedures of multi-angle compound SWEI (MAC-SWEI).

To realize the phase shift $\Delta\phi$, we delayed the signals on every other element. The corresponding time delay $\tau_{\Delta\phi}$ was defined as

$$\tau_{\Delta\phi} = \frac{1}{f_0} \cdot \frac{\Delta\phi}{360°}, \quad (2)$$

where f_0 is the center frequency of a push pulse. For example, for f_0 = 4 MHz and $\Delta\phi$ = 140°, the required time delay $\tau_{\Delta\phi}$ was about 97.2 ns. Due to a master clock of 250 MHz in the Verasonics system, $\tau_{\Delta\phi}$ applied in the system was 96 ns (i.e., the closest multiple of 4 ns time resolution), indicating that $\Delta\phi$'s of 138.24° and 178.56° were used in the system on behalf of ideal $\Delta\phi$'s of 140° and 180°, respectively.

In experiments, the duration of the excitation pulse was 600 μs while in the Field II simulation, we used a pulse duration of 10 μs to decrease the computational time. All other parameters were the same as listed in Table 1. After applying the push pulse, the generated shear waves were recorded using ultrafast plane wave imaging [73]. The three angles of the plane waves, whose center frequency was 4.3 MHz, were −4°, 0°, and 4°. Their pulse-repetition frequency (PRF) was 10 kHz, and thus, the effective PRF was 3.33 kHz.

To visualize the propagation of shear waves, we estimated axial particle velocities from acquired IQ sequences using a two-dimensional auto-correlation approach [74, 75]. The number of ensembles was three, and the length of the auto-correlation kernel was 2λ. Then, we applied multi-directional filtering [64, 65, 76], originally introduced in magnetic resonance elastography [63], to multi-angular shear waves to separate them in space and time. To design the multi-directional filter, we calculated the angles of two grating lobes, ±40°, from Equation 1. Although our dual-phase configuration generated six shear waves from three push beams (i.e., one main and two left/right grating lobes), we eliminated two shear waves that were traveling toward the upper right and upper left corners of FOV because of their small propagation distances. Thus, MAC-SWEI utilized four shear waves: right-to-left from the left grating lobe (RL_{GL}), right-to-left from the main lobe (RL_{ML}) left-

to-right from the right grating lobe (LR_{GL}), and left-to-right from the main lobe (LR_{ML}), depicted in Figure 2.

From the four shear-wave sequences (RL_{GL}, RL_{ML}, LR_{GL}, and LR_{ML}), four corresponding SWV maps were reconstructed using a two-dimensional cross-correlation approach [76, 77]. Here, the distance between the cross-correlating shear wave signals in both lateral and axial directions was 2.1 mm. Thereafter, the reconstructed SWV maps were filtered using a two-dimensional median filter (1.0 mm x 1.0 mm). Before combining these four SWV maps, because we know the positions and the angles of all pushing sources, the regions excited by push beams were excluded. Thus, we defined the binary maps R(*x*,*y*,*n*) (indicated by black dashed regions in four estimated SWV maps in Figure 2), which determined the SWV maps that will be combined. Here, *x* and *y* represent the lateral and axial positions and *n* denotes the order of the SWV maps used for compounding (*n* = 1,2,3,4). R(*x*,*y*,*n*) = 1 or 0 represents an SWV value of the *n*th SWV map at *x* and *y* that is included or excluded, respectively, in the combined SWV map. To produce a combined single SWV map, a weighted summation of four SWV maps was used as

$$\mathrm{SWV}_{\mathrm{CMPND}}(x,y) = \frac{\sum_{n=1}^{4} \mathrm{SWV}(x,y,n) \cdot \mathrm{R}(x,y,n)}{\sum_{n=1}^{4} \mathrm{R}(x,y,n)}, \tag{3}$$

where $SWV_{CMPND}(x,y)$ is the compounded SWV map, and *x* and *y* represent the lateral and axial positions. SWV(*x*,*y*,*n*) contains four SWV maps acquired from their corresponding angular shear waves. Because the push regions can be eliminated, the combined MAC-SWEI-based SWV maps are bias-reduced and reliable. Furthermore, by combining multiple SWV maps resulting from the shear waves, oriented differently and propagating in different directions, MAC-SWEI improves the quality of an SWV map similar to angular-spatial compounding used in the B-mode or strain elastography [78].

In addition to MAC-SWEI with the shear waves with four wave-front angles, created by applying $\Delta\phi$ of 140°, we realized two more configurations with $\Delta\phi$'s of 0° and 180° for comparison (Figure 3). First, $\Delta\phi$ of 0° generated only the main lobe, resulting in two SWV maps from RL_{ML} and LR_{ML}. By contrast, $\Delta\phi$ of 180° created only the two grating lobes, resulting in two SWV maps from RL_{GL} and LR_{GL}. With $\Delta\phi$ = 140°, four SWV maps from all three lobes were generated. Thus, for $\Delta\phi \neq 0°$, the two shear waves from the two grating lobes (RL_{GL} and LR_{GL}) propagate the push regions of each other (i.e., RL_{GL} travels to the region where LR_{GL} is created, and vice versa), allowing for the reconstruction of SWV maps with an entire FOV.

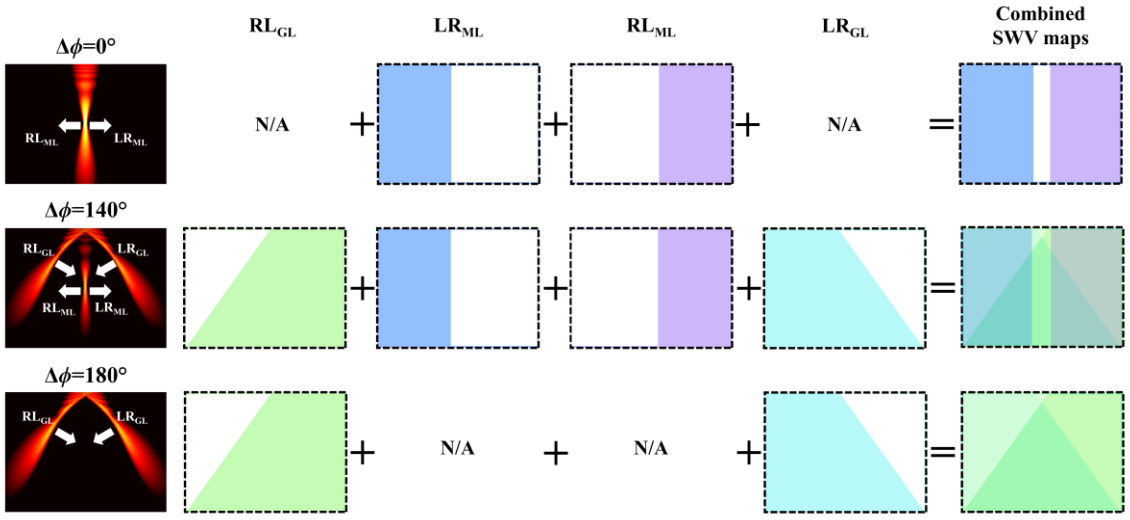

Figure 3 – Three available pushing configurations by dual-phase transmit focusing and combining of corresponding SWV maps.

2.2.3 Phantom Experiments and Assessment Metrics

To assess the performance of MAC-SWEI, we imaged a quality assurance elasticity phantom (Model 049, CIRS Inc., Norfolk, VA, USA) containing several spherical inclusions within a homogeneous background. The nominal SWV values of the stiffest inclusion and the background are 5.11 m/s and 2.86 m/s (80 kPa and 25 kPa in terms of Young's modulus), respectively. To verify and compare various available configurations

of dual-phase transmit focusing, the stiffest inclusion and the homogeneous background were evaluated with three $\Delta\phi$'s—0°, 140°, and 180°—, which create one main lobe, three lobes, and two grating lobes, respectively. In addition, we placed the inclusion at two locations: the center of the image and +10 mm to the right from the center (i.e., the inclusion was positioned at the same depth, but it was displaced laterally). For quantitative evaluation, we calculated the mean and the standard deviation (STD) of the SWV values in a region-of-interest (ROI). For the homogeneous background, when $\Delta\phi$ = 0°, the means and the STDs were estimated only in the non-pushing regions, but when $\Delta\phi$ = 140° and 180°, all of the SWV regions were used. Two circular ROIs at the same depth covering the inclusion and the background region were used. We also assessed a blind area (BA) to explore the amount of unacceptable outliers in the SWV map [79]. Here, we classified an SWV value larger than (mean+3·STD) or less than (mean−3·STD) as an unacceptable SWV value and then computed the BA by the number of unreliable pixels in the SWV map, divided by the number of all pixels. Furthermore, we evaluated a contrast-to-noise ratio (CNR) [67] and % error defined as

$$\mathrm{CNR} = \frac{|\mu_\mathrm{I} - \mu_\mathrm{B}|}{\sqrt{\sigma_\mathrm{I}^2 + \sigma_\mathrm{B}^2}}, \tag{4}$$

$$\%\ \mathrm{error} = \frac{C_\mathrm{E} - C_\mathrm{N}}{C_\mathrm{N}} \times 100, \tag{5}$$

where μ_I and μ_B, and σ_I and σ_B in Equation 4 indicate the means and the STDs of the SWV values in the inclusion and background regions, respectively. For % error in Equation 5, c_E and c_N represent the estimated and nominal SWV values in the ROI, respectively.

2.2.4 Safety Measurements

To ensure the clinical applicability of the MAC-SWEI technique, we measured acoustic parameters, including the mechanical index (MI), the spatial peak temporal average intensity (I_{SPTA}), and the spatial peak pulse average intensity (I_{SPPA}). Currently, the Food and Drug Administration (FDA) limits the MI, the I_{SPTA}, and the I_{SPPA} to 1.9, 720 mW/cm^2, and 190 W/cm^2, respectively. The MI, the I_{SPTA}, and the I_{SPPA} are defined as follows [80]:

$$\mathrm{MI} = \frac{P_{r,derated}}{\sqrt{f_c}}, \tag{6}$$

$$\mathrm{I_{STPA}} = \mathrm{PII_{derated}} \cdot \mathrm{PRF}, \tag{7}$$

$$\mathrm{I_{SPPA}} = \frac{\mathrm{PII_{derated}}}{\mathrm{PD}}, \tag{8}$$

where $P_{r,derated}$ is the derated peak rarefactional pressure at the focus of the main and grating lobes (MPa), and f_C is the center frequency (4.0 MHz). $\mathrm{PII_{derated}}$ is the derated pulse intensity integral (μJ/cm^2), PRF is the pulse-repetition frequency of the pushing pulse (1 Hz was assumed), and PD is the pulse duration (600 μs). Here, P_r and PII are defined as

$$P_r = \frac{|\min(v(t))|}{\mathrm{M_l}(f_c)}, \tag{9}$$

$$\mathrm{PII} = \frac{\int_{t_1}^{t_2} v^2(t)dt}{\rho c \mathrm{M_l^2}(f_c)}, \tag{10}$$

where $v(t)$ represents the measured voltage. The sensitivity of a hydrophone is denoted by $\mathrm{M_l}(f_C)$, where f_C is the center frequency of a pulsed wave. The beginning and end times of the pulse are denoted by t_1 and t_2, ρ is the density of water (1,000 kg/m^3), and c is the speed of sound in water (1,484 m/s). To reflect the attenuation of ultrasound in tissue, we derated

the recorded waveforms with an attenuation coefficient of 0.3 dB/cm/MHz. We used a 0.2-mm needle hydrophone (Precision Acoustics Ltd., Dorchester, Dorset, UK) and a DC coupler (DCPS233, Precision Acoustics Ltd., Dorchester, Dorset, UK) to acquire acoustic pressures, recorded by an oscilloscope (PicoScope 3406D, Pico Technology Ltd., St Neots, Cambridgeshire, UK).

2.3 Results and Discussion

2.3.1 Multi-Angular Acoustic Radiation Force Fields

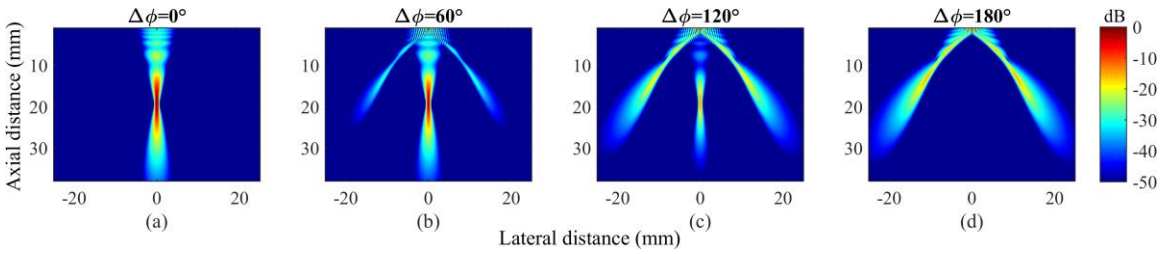

Figure 4 – Simulated multi-angular acoustic pressure fields created by dual-phase transmit focusing with $\Delta\phi$'s of (a) 0°, (b) 60°, (c) 120°, and (d) 180°.

Field II simulation results of normalized acoustic pressure fields created by dual-phase transmit focusing with four selected $\Delta\phi$'s (0°, 60°, 120°, and 180°) are shown in Figure 4. In total, 181 fields (from 0° to 180°) were simulated, and an average execution time for each field was 165.8 s on a desktop computer with Intel(R) Core(TM) i7-6700K at 4.0 GHz. For $\Delta\phi$ = 0°, dual-phase transmit focusing created only the main lobe (Figure 4 (a)). However, for $\Delta\phi \neq 0°$, the periodic incoherency in the transmit phases introduced the grating lobes in the FOV. As $\Delta\phi$ increased from 0° to 180°, the magnitudes of the grating lobes increased, while that of the main lobe decreased. Finally, because $\Delta\phi$ of 180° canceled the main lobe at the focus, only the two strongest grating lobes are observed (Figure 4 (d)).

Figure 5 shows the maximum acoustic pressure of the main and grating lobes as a function of $\Delta\phi$. Again, as $\Delta\phi$ increased, the magnitude of the main lobe decreased whereas those of the grating lobes increased. The intersection of the main and grating lobe curves (a red circle in Figure 5) indicates that the value of phase difference ($\Delta\phi$ is around 130°) could generate three push beams of equal magnitude. Therefore, the phase difference $\Delta\phi$ determines the distribution of the acoustic energy between the main and grating lobes in dual-phase transmit focusing. These results suggest that the magnitude of the multi-angular push beams can be delicately controlled.

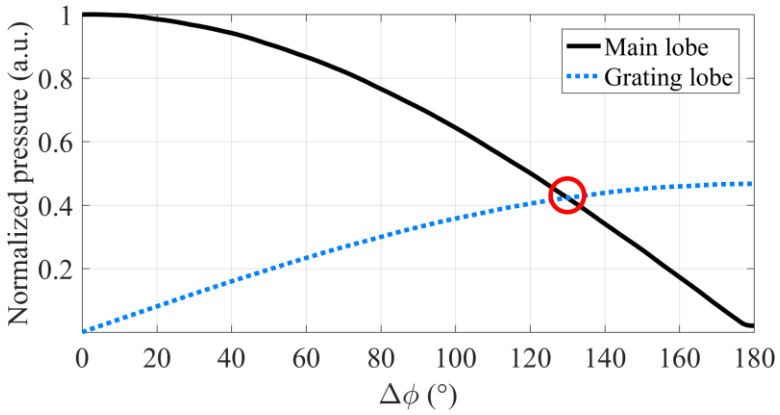

Figure 5 – Normalized acoustic pressure of the main lobe and the grating lobes as a function of $\Delta\phi$.

2.3.2 Shear Waves Created with Dual-Phase Transmit Focusing

The generation and the propagation of shear waves, created by dual-phase transmit focusing with three $\Delta\phi$'s (0°, 140°, and 180°) in the homogeneous background region of the phantom as a function of time, are shown in Figure 6. Here, we applied three $\Delta\phi$'s to demonstrate that dual-phase transmit focusing generates shear waves as expected. Indeed, $\Delta\phi$ = 0° generated two shear waves from the main lobe, similar to conventional SWEI; $\Delta\phi$ = 140° created one main and two grating lobes that induced the shear waves of three distinct angles. As the shear waves induced by the grating lobes traveled a greater distance than those induced by the main lobe in the FOV, we applied 140° (instead of 130°, as indicated

in Figure 5) of $\Delta\phi$, which resulted in the slightly stronger grating lobes compared with the main lobe. Finally, for $\Delta\phi$ = 180°, only two grating lobes were produced, and thus, propagation of two tilted shear waves were observed from the third row images in Figure 6.

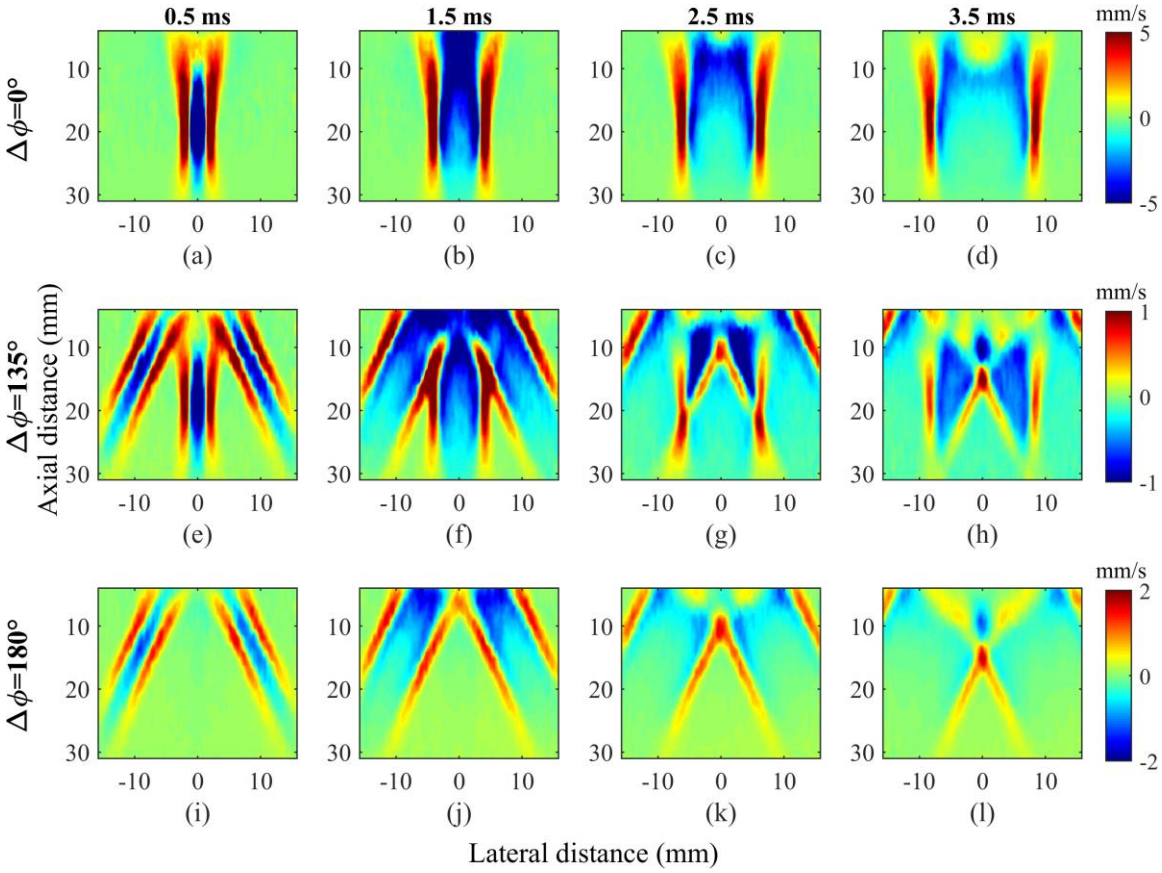

Figure 6 – Estimated axial velocity sequences in the homogeneous region of the phantom with multiple choices of $\Delta\phi$'s at various time points. Rows represent three $\Delta\phi$'s (0°, 140°, and 180°). Columns represent four time points (0.5 ms, 1.5 ms, 2.5 ms, and 3.5 ms) after pushing.

2.3.3 Homogeneous Region

From three sets of shear-wave sequences (Figure 6) created by three pushing configurations ($\Delta\phi$'s of 0°, 140°, and 180°), we reconstructed the final combined SWV maps, as shown in Figure 7. To obtain the SWV maps in Figure 7, we first applied multi-directional filtering that separates shear waves with several angles, leading to the

reconstruction of corresponding SWV maps. Thereafter, these SWV maps were combined, allowing us to obtain final SWV maps covering a full FOV, as shown in Figure 7. For $\Delta\phi$ = 0°, none of the two shear waves (RL_{ML} and LR_{ML}) from a main lobe propagated through the pushing region, and a final SWV map had a limited FOV (Figure 7 (b)). By contrast, for $\Delta\phi \neq 0°$ (i.e., $\Delta\phi$ = 140° and $\Delta\phi$ = 180°), shear waves covered the pushing regions of each other, and a final SWV map had a full FOV (Figure 7 (c) and (d)). However, because multi-directional filtering cannot completely separate different angles of shear waves, slightly overestimated SWV values were observed in the regions where the two grating lobes were generated. To reduce these possible artifacts, multi-directional filter masks should be carefully designed according to the angle and the bandwidth of the shear waves.

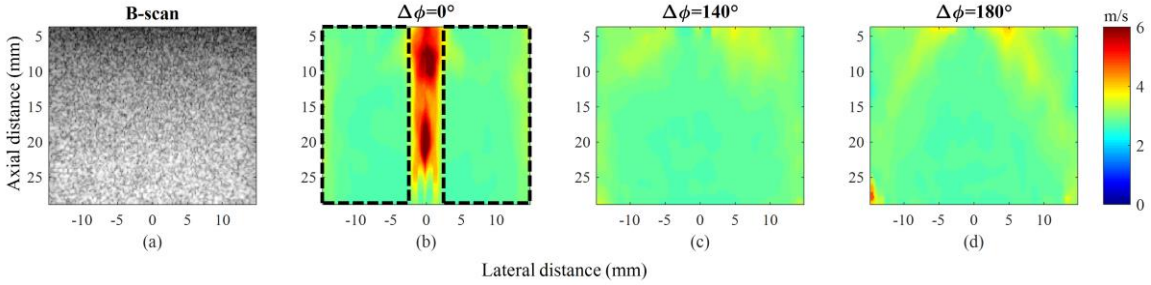

Figure 7 – Experimental results on the homogeneous region. (a) B-scan image and reconstructed SWV maps with $\Delta\phi$'s of (b) 0°, (c) 140°, and (d) 180°.

Table 2 – Quantitative assessment results in the homogeneous background.

	$\Delta\phi$ = 0°	$\Delta\phi$ = 140°	$\Delta\phi$ = 180°
Mean ± STD (m/s)	2.84 ± 0.15	2.85 ± 0.14	2.86 ± 0.16
% error (%)	−0.86	−0.28	0.07
Blind area (BA) (%)	15.28	0.62	2.26

For the quantitative evaluation, we computed the mean, the STD, the % error, and the BA of the SWV maps in the homogeneous background regions (Table 2). Here, for $\Delta\phi$ = 0°, the mean and the STD were estimated only in the non-pushing regions (as indicated by dotted black boxes in Figure 7 (b)), but for $\Delta\phi$ = 140° and $\Delta\phi$ = 180°, all of the SWV

regions were used. However, for computing the BA, the entire region of the SWV maps was used. The differences among the means, the STDs, and the % errors obtained from the three $\Delta\phi$'s were not noticeable. The BA indicates that $\Delta\phi$ of 140° yields the most reliable SWV map with the widest FOV coverage. For $\Delta\phi$ of 0°, accurate reconstruction of the SWV map within the pushing region was not possible due to artifacts, resulting in the largest BA among the three pushing schemes.

2.3.4 Single Hard Spherical Inclusion within Background

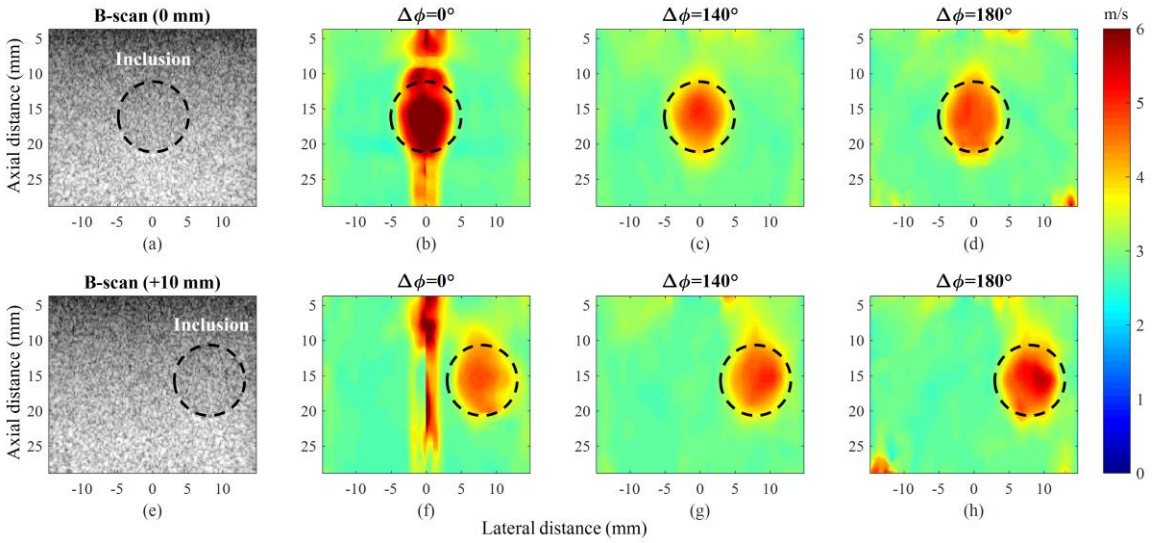

Figure 8 – Experimental results from the region of the phantom containing a single stiff inclusion at two lateral positions (0 mm and + 10 mm). (a) B-scan image where the inclusion is located at 0 mm and the corresponding SWV maps obtained with $\Delta\phi$'s of (b) 0°, (c) 140°, and (d) 180°. (e) B-scan image where the inclusion is located at +10 mm and the corresponding SWV maps obtained with $\Delta\phi$'s of (f) 0°, (g) 140°, and (h) 180°.

Figure 8 shows the reconstructed SWV maps of a region with a single hard spherical inclusion at two positions (0 mm and +10 mm) using three $\Delta\phi$'s (0°, 140°, and 180°). As a result, the measurement at $\Delta\phi$ = 0° failed to reliably reconstruct the inclusion in the pushing region (Figure 8 (b)), but once the push beam was off the inclusion, the inclusion was appropriately reconstructed in the SWV map (Figure 8 (f)). However,

regardless of the inclusion location, both $\Delta\phi$'s of 140° and 180° consistently and reliably reconstructed the SWV maps for both lateral positions at 0 mm and +10 mm. The dotted black circles (10 mm diameter) in Figure 8 outline the position and the size of the inclusion. Overall, the shape and the size of the inclusion obtained, based on the SWV map values, show good agreement with the actual characteristics of the inclusion. However, the size of the inclusion in the SWV maps appears to be slightly smaller than the actual size of the inclusion. This is partially due to the kernel length of correlation used for estimating SWV values.

Table 3 – Quantitative assessment results in the phantom with a stiff spherical target.

Inclusion position			$\Delta\phi$ = 0°	$\Delta\phi$ = 140°	$\Delta\phi$ = 180°
0 mm	Mean ± STD (m/s)	Inclusion	6.36 ± 0.64	4.71 ± 0.19	4.69 ± 0.13
		Background	2.81 ± 0.12	2.87 ± 0.08	2.87 ± 0.04
	% error (%)	Inclusion	24.39	−7.87	−8.19
		Background	−1.91	0.33	0.46
	CNR		5.44	8.77	13.20
+10 mm	Mean ± STD (m/s)	Inclusion	4.56 ± 0.15	4.73 ± 0.16	5.09 ± 0.28
		Background	2.79 ± 0.11	2.82 ± 0.05	2.85 ± 0.06
	% error (%)	Inclusion	−10.81	−7.35	−0.43
		Background	−2.33	−1.23	−0.49
	CNR		N/A	11.22	7.85

Table 3 summarizes the quantitative assessment of the SWV maps presented in Figure 8 using the mean, the STD, the % error, and the CNR. First, for the inclusion located at the center (0 mm), the measurement with $\Delta\phi$ of 0° suffered from overestimation of SWV within the inclusion region (% error is 24.39%) while $\Delta\phi$'s of 140° and 180° led to relatively stable reconstruction of SWV both within the inclusion region and the background. Furthermore, the CNR improvements of $\Delta\phi$'s of 140° and 180° over that of 0° were 61.21% and 142.65%, respectively. For the inclusion displaced +10 mm laterally,

none of the methods suffered from an overestimation of SWV within the inclusion region. The overall % error results merely show slight underestimation of SWV in the inclusion, which may be due to a measurement error in the nominal value (±5%) or the spherical shape of the inclusion [81]. The CNR values of the three methods were similar, but $\Delta\phi$ of 140° yielded the highest CNR. Overall, at two positions of inclusion, the measurements with $\Delta\phi$ of 140°, compared to the other measurements, showed the most consistent means and STDs.

2.3.5 Safety Measurements

Table 4 – Measured safety parameters with three $\Delta\phi$'s (0°, 140°, and 180°).

$\Delta\phi$	MI	ISPTA (mW/cm2)	ISPPA (W/cm2)
0°	1.73	70.49	117.48
140°	0.77	11.40	19.00
180°	0.72	9.45	15.76
FDA limit	1.9	720	190

The MI, the I_{SPTA}, and the I_{SPPA}, measured for three $\Delta\phi$'s (0°, 140°, and 180°) at the foci of the main and grating lobes (Table 4), indicate that the measured safety parameters were below the FDA regulatory limits. It is important to note that although we induced the same voltage (80 Vpp) and used the same number of active elements (i.e., the same f-number) to generate ultrasound waves for the three pushing configurations, the distribution and the concentration of acoustic energy within FOV varied according to $\Delta\phi$. As illustrated in Figure 5, the acoustic pressure of the grating and main lobes is a function of $\Delta\phi$. For $\Delta\phi$ = 0°, all acoustic energy is concentrated mostly in a main lobe, thus the acoustic outputs are the highest but within the FDA guideline. By contrast, pulses with $\Delta\phi$'s of 140° and 180° divided the total acoustic energy into more than one push beam and, therefore, may

further reduce the safety concerns, thus providing another benefit of dual-phase transmit focusing.

2.3.6 Two Potential Candidates for Creating Simultaneous Multi-Angular Push Beams

We can produce simultaneous multi-angular push beams in two more ways. One approach is to arrange and excite differently steered beams using the sub-divided apertures of an ultrasound transducer. This overall concept is similar to CUSE [76], but the introduced steering angles of the push beams are different, as shown in Figure 9 (a). However, a typical linear array transducer (e.g., L7-4, Philips Healthcare, Andover, MA, USA) has an element spacing of about 300 μm, which is similar to a wavelength of 4-5 MHz ultrasound, unwanted grating lobes could appear in the FOV once the ultrasound beams are steered. These undesirable grating lobes cause the loss of acoustic energy and obscure the appropriate formation of acoustic radiation force fields. In addition, the sub-divided, reduced size of sub-apertures broadens the width of each beam and degrades the pushing efficiency. Another way is to apply the sparse array technique that drives ultrasound waves using only every other element of an array, which deliberately brings two desirable grating lobes into the FOV for angular pushing, is illustrated in Figure 9 (b). However, as only half of the elements are used, half of the acoustic energy is lost accordingly. Furthermore, not only are we unable to control the magnitudes of the grating lobes, but their magnitudes are also much weaker than that of the main lobe [82]. Therefore, this approach may be ineffective in the creation of multi-angular push beams.

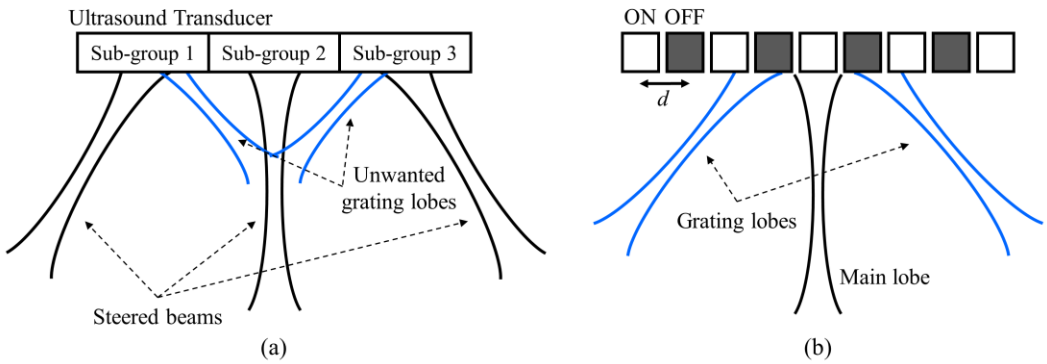

Figure 9 – Two possible ways of generating simultaneous multi-angular push beams: (a) steering with sub-divided apertures and (b) a sparse array technique.

Field II simulated acoustic pressure maps, produced with these two methods (i.e., steering with sub-apertures and the sparse array technique), are shown in Figure 10. For fair comparison, the same parameters, as listed in Table 1, were used for push pulses (except their arrangements on the transducer). First, for the steering angles of ±10°, no grating lobes appeared (Figure 10 (a)). However, as the steering angle increased from ±10° to ±40°, the grating lobes started to appear. As the steering angles became ±40°, which is desirable to separate the resultant multi-angular shear waves, the magnitudes of the unwanted grating lobes became similar to those of their main lobes (Figure 10 (c)). The sparse array technique simultaneously created desirable grating lobes and a main lobe (Figure 10 (d)). However, the magnitude of the grating lobes, compared to the main lobe, was considerably weaker and intractable. Dual-phase transmit focusing, which applies two phases on every other element (Figure 4), effectively overcame these limitations. According to the selected phase difference, dual-phase transmit focusing distributed the total acoustic energy to one main and two grating lobes, and unlike the sparse array technique, the approach did not suffer from energy loss. In addition, the dual-phase transmit approach uses an entire aperture (not sub-divided apertures) to create multi-angular push beams, and thus, the width of the push beams, unlike those produced by sub-apertures, does not widen.

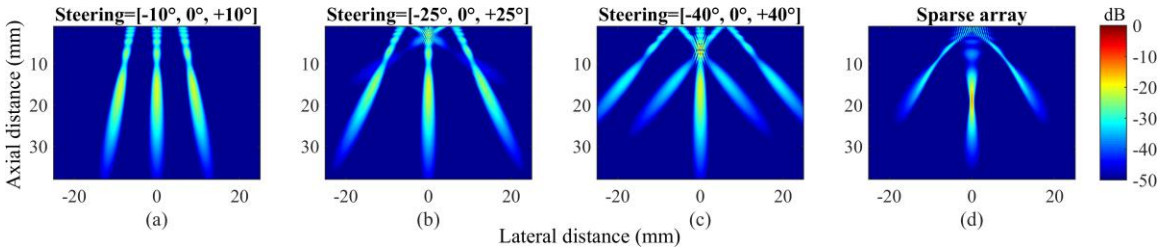

Figure 10 – Simulated multiangular acoustic pressure fields created by the subdivided aperture approach with steering angles of (a) −10°, 0°, +10°, (b) −25°, 0°, +25°, (c) −40°, 0°, +40°, and (d) sparse-array technique.

Table 5 summarizes the results of the quantitative assessment of angular push beams based on Field II simulations. Here, we compared three methods (i.e., steering with sub-apertures, the sparse array technique, and dual-phase transmit focusing) with push beams of the same angles (±40°). For dual-phase transmit focusing, we applied $\Delta\phi$ of 140°. First, steering with sub-apertures caused energy loss because of undesirable grating lobes, and the reduced size of sub-divided apertures yielded the lowest peak pressure in both the main lobe and the angular beams. In addition, although the sub-aperture approach produced the longest depth of focus (DOF), the larger f-number of sub-divided apertures broadened the lateral beam width, and thus, increased the full width at half maximum (FWHM). The sparse array technique yielded a narrower FWHM than those of the sub-divided apertures, but the peak pressure of the angular beams, compared to that of the main lobe, became less than half. Overall, dual-phase transmit focusing maintained the lateral beam width while preserving peak pressures, which could be ideal in the simultaneous creation of multi-angular push beams. Nevertheless, further studies on optimizing the angular push beams are necessary for the clinical translation of this technique, because our approach distributes the given acoustic energy into three lobes, which lowers the magnitude of shear wave signals compared to single push-based SWEI approaches.

Table 5 – Quantitative assessment results of push beams created by three methods.

	Main lobe			Angular beams		
	Peak pressure (a.u.)	FWHM (mm)	DOF (mm)	Peak pressure (a.u.)	FWHM (mm)	DOF (mm)
Steering with sub-apertures	0.36	2.21	10.82	0.20	3.30	13.54
Sparse array technique	0.50	0.91	6.41	0.23	1.67	9.61
Dual-phase transmit focusing	0.42	0.91	6.43	0.42	1.65	9.56

2.3.7 Computational Complexity

Computational complexity of MAC-SWEI, requiring multi-directional filtering and reconstruction of four SWV maps, could be one of the concerns for real-time imaging. However, many SWEI-based methods have already adopted (multi-) directional filtering to remove reflected shear waves from boundaries of inclusions or targets [27, 64, 65, 76]. In addition, unlike single-push SWEI methods, MAC-SWEI completes the final reconstruction of an SWV map within a single pushing-tracking event; if a PRF of a push pulse is 1 Hz, then the frame rate of SWV maps created by MAC-SWEI is also 1 Hz. However, in conventional SWEI methods, the frame rate could be ½ Hz to ¼ Hz (depending on the number of push beam applications at different locations). Thus, although MAC-SWEI requires four-fold more computations to create a final SWV map, it provides a two- to four-fold faster frame rate. Therefore, for the given frame rate of SWV images, both MAC-SWEI and single-push SWEI methods will have similar computational complexity in terms of the number of estimation of SWV maps. Furthermore, single-push SWEI methods could require longer overall computation times due to additional processes, including beamforming and image formation, for multiple sets of data acquired.

2.4 Conclusion

This chapter introduced a new way of creating multi-angular push beams, referred to as "dual-phase transmit focusing." By alternatively applying two phases on every other element, dual-phase transmit focusing efficiently and simultaneously creates one main and two grating lobes as pushing sources, which realizes multi-angle compound SWEI (MAC-SWEI). We found that the phase difference $\Delta\phi$ determines the energy distribution to these three lobes. We investigated three representative configurations with $\Delta\phi$'s of 0°, 140°, and 180°, and quantitatively assessed the performance of MAC-SWEI using an elasticity phantom with a single stiff inclusion. Our results suggest that MAC-SWEI can be used to visualize SWV maps reliably, and with improved image quality. An additional study is required to optimize the dual-phase transmit focusing as the choice of optimal $\Delta\phi$ may depend on size, shape, or location of a lesion. Thus, our future work will be focused on the optimization of dual-phase transmit focusing and the clinical translation of this technique.

CHAPTER 3. IMPACT OF DEPTH-DEPENDENT OPTICAL ATTENUATION ON WAVELENGTH SELECTION FOR SPECTROSCOPIC PHOTOACOUSTIC IMAGING

The chapter was reproduced and reprinted with permission from H. Yoon, G. P. Luke, and S. Y. Emelianov, "Impact of depth-dependent optical attenuation on wavelength selection for spectroscopic photoacoustic imaging", Photoacoustics, October, 2018. The reference can be found in [83].

An optical wavelength selection method based on the stability of the absorption cross-section matrix to improve spectroscopic photoacoustic (sPA) imaging was recently introduced. However, spatially-varying chromophore concentrations cause the wavelength- and depth-dependent variations of the optical fluence, referred to as spectral coloring, which degrades the accuracy of quantitative sPA imaging. This chapter introduces a depth-optimized method that determines an optimal wavelength set minimizing an inverse of the multiplication of absorption cross-section matrix and fluence matrix to minimize the errors in concentration estimation. This method assumes that the optical fluence distribution is known or can be attained otherwise. We used a Monte Carlo simulation of light propagation in tissue with various depths and concentrations of deoxy-/oxy-hemoglobin. We quantitatively compared the previous and current approaches, indicating that the choice of wavelength is critical, and our approach is effective especially when quantifying deeper imaging targets.

3.1 Introduction

Blood oxygen saturation (SO_2), the ratio of oxygenated to total hemoglobin concentrations in the blood, provides useful functional information on many pathological conditions including cancer. Since oxygen deficiency (hypoxia) in a tumor is strongly associated with a tumor malignancy, metastasis, and resistance to various therapies, the non-invasive estimation of the SO_2 level is essential for tumor characterization and treatment planning [36, 37, 84]. Naturally, to explore tumor hypoxia, researchers have investigated various medical imaging and sensing techniques such as needle electrodes, near-infrared spectroscopy (NIRS), positron emission tomography (PET), blood oxygen level-dependent (BOLD) magnetic resonance imaging (MRI), and electron paramagnetic resonance imaging (EPRI) [85, 86]. However, none of these techniques offers non-invasive and real-time measurements of SO_2 with high sensitivity and fine spatial resolution at clinically relevant depths.

As an effective alternative, photoacoustic (PA) imaging is becoming a promising biomedical imaging modality since it provides high optical absorption contrast from endogenous chromophores and exogenous contrast agents with ultrasonic resolution [32, 33, 87]. This ability of PA imaging shows substantial potential in the characterization of tumors, atherosclerotic plaque, and brain functionality [33, 88-91]. Moreover, spectroscopic photoacoustic (sPA) imaging can quantify the concentrations of multiple absorbers. Since each optical absorption spectrum is a unique function of optical wavelength, multiple tissue chromophores can be separated using a multi-wavelength set of PA images [92-94]. Thus, because of its ability to unmix concentrations of multiple absorbers, sPA imaging has been extensively used in many applications including the measurement of SO_2 and nanoparticle deposition [41, 90, 95-98].

To estimate the concentrations of various absorbers, we have to solve optical and acoustic inverse problems [32, 95]. The solution of optical inverse problem requires a multi-wavelength or spectroscopic set of PA images. However, sPA imaging extends data acquisition time and, therefore, degrades temporal resolution and increases motion artifacts. In addition, a tunable laser system is less cost-effective in comparison to a small set of single-wavelength lasers. Thus, the careful choice of wavelengths is imperative. To select an optimal set of wavelengths, a method of capturing the unique spectral features of absorbers under a given number of wavelengths was developed previously [99]. In this approach, we used the stability of the absorption cross-section matrix under a pseudoinverse operation as a criterion and selected a set of wavelengths whose absorption cross-section matrix has the largest minimum singular value as the optimal set. The developed method showed the promising potential in the wavelength selection for *in vivo* imaging [98].

Because chromophores vary spatially, optical fluence is a function of position and wavelength. Thus, the amount of light fluence reaching the region-of-interest (ROI) needs to be taken into account through analytical or numerical modeling of light transport in tissue. This study investigates the impact of optical wavelength selection in the presence of light fluence variations in tissue. Under the assumption that the fluence distribution in the tissue is known, we introduce a depth-optimized wavelength selection method that accurately estimates the concentrations of absorbers. In practice, the fluence distribution can be determined by an independent measurement [100, 101], or accounted for in an inversion scheme that uses a light transport model [95, 102-104]. For verification of our approach, we use a Monte Carlo (MC) simulation of light propagation in tissue with a

blood vessel containing various SO_2 levels at multiple depths. For a quantitative evaluation, we compare the proposed and previous methods by applying the various levels of additive white Gaussian noise and computing the root-mean-square errors (RMSE) of oxy- and deoxy- hemoglobin concentrations.

3.2 Theory of Spectroscopic Photoacoustic (sPA) Imaging

The photoacoustic effect describes the generation of sound waves following light absorption and thermoelastic expansion, resulting in a peak local pressure rise, p_0. Here, p_0 is a function of optical wavelength λ and determined by the combination of three quantities (Grüneisen coefficient Γ (the PA efficiency), optical absorption coefficient μ_a, and light fluence Φ) as follows [95]:

$$p_0(\lambda) = \Gamma \mu_a(\lambda) \Phi(\lambda). \tag{11}$$

Three wavelength-dependent quantities and the Grüneisen coefficient in Equation 11 (i.e., p_0, μ_a, Γ and Φ) are all also spatially variant, but for the simplicity, their position vector is not used in this chapter. Here, μ_a is generally a linear combination of absorber concentrations, and thus, can be represented as

$$\mu_a(\lambda) = \sum_{i=1}^{I} \varepsilon_i(\lambda) C_i, \tag{12}$$

where I is the number of absorbers of interest, ε_i is the molar absorption cross section of the ith absorber, and C_i is the concentration of the ith absorber. We assume that the Grüneisen coefficient is constant and the light fluence distribution is known. In practice, modeling of light fluence is challenging because of unknown optical properties of tissue in

general [95, 102, 105-108]. In addition, although the reconstruction of the acoustic signals received by an ultrasound transducer, depending on tissue heterogeneity, acoustic properties, and detector geometry, is not trivial, here we assume that p_0 can be accurately reconstructed [109]. Then, the local ultrasound pressure (p_0 in Equation 11) can be converted to $\mu_{a,est}$ by assuming that the light fluence distribution over wavelength at every spatial location is known.

$$\mu_{a,est}(\lambda) = \frac{p_0(\lambda)}{\Gamma\Phi(\lambda)}. \tag{13}$$

Then, by combining Equation 12 and 13 and using vector notation, a set of linear equations is formulated as

$$\boldsymbol{\mu}_{\mathbf{a,est}} = \boldsymbol{\varepsilon}\mathbf{C}, \tag{14}$$

where $\boldsymbol{\mu}_{\mathbf{a,est}}$ is the M-by-1 vector with reconstructed absorption coefficients (M is the number of wavelengths used in sPA imaging), $\boldsymbol{\varepsilon}$ is the M-by-I absorption cross-section matrix, and $\mathbf{C}$ is the I-by-1 vector of absorber concentrations (I is again the number of optical absorbers of interest). Then, when M is equal to or greater than I, the concentrations can be computed by

$$\mathbf{C}_{\mathbf{est}} = \boldsymbol{\varepsilon}^{+}\boldsymbol{\mu}_{\mathbf{a,est}}, \tag{15}$$

where $\mathbf{C}_{\mathbf{est}}$ is the estimates of true concentrations ($\mathbf{C}$) and $\boldsymbol{\varepsilon}^{+}$ is the pseudoinverse of $\boldsymbol{\varepsilon}$. Here, to prevent concentration estimates from becoming less than 0 or larger than 1, further constraints, including a non-negativity constraint, can be applied in Equation 15 [96, 110].

3.3 Materials and Methods

3.3.1 A Depth-Optimized Wavelength Selection Method

Although the use of extra wavelengths typically allows us to obtain more precise estimates of concentrations in the presence of noise (but, in the absence of motion), it is desirable to keep the number of wavelengths to as few as possible to avoid motion artifacts, to improve temporal resolution, and to accelerate image acquisitions. To reduce the redundancy in the choice of wavelengths while preserving accuracy, this study introduces an algorithm that finds an optimal set of wavelengths for accurate concentration estimation. Then, with the consideration of the thermal and electronic noise in the system, local acoustic pressure p_0, in Equation 11 can be redefined by adding white Gaussian random noise n:

$$p_0(\lambda) = \Gamma \mu_a(\lambda) \Phi(\lambda) + n. \tag{16}$$

Dividing both sides of Equation 16 by the Grüneisen coefficient and the optical fluence yields

$$\frac{p_0(\lambda)}{\Gamma \Phi(\lambda)} = \mu_a(\lambda) + \frac{n}{\Gamma \Phi(\lambda)}. \tag{17}$$

By presenting Equation 17 as a simpler vector form, we obtain the following equation:

$$\boldsymbol{\mu}_{\mathbf{a,n}} = \boldsymbol{\mu}_{\mathbf{a,est}} + \frac{\boldsymbol{\Phi}_{\mathbf{D}}^{-\mathbf{1}}\mathbf{n}}{\Gamma}, \tag{18}$$

where $\boldsymbol{\mu}_{\mathbf{a,n}}$ is the M-by-1 vector of the reconstructed absorption coefficients, $\mathbf{n}$ is the M-by-1 noise vector, and $\boldsymbol{\Phi}_{\mathbf{D}}$ is the M-by-M diagonal matrix where $\boldsymbol{\Phi}_{\mathbf{D}}(j,j) = \Phi(j)$. Like Equation

15, the noise-corrupted estimates of concentrations $\mathbf{C_{est,n}}$ can be obtained by taking the pseudoinverse of $\boldsymbol{\varepsilon}$.

$$\mathbf{C_{est,n}} = \mathbf{C_{est}} + \frac{\boldsymbol{\varepsilon}^{+}\boldsymbol{\Phi}_{\mathbf{D}}^{-1}\mathbf{n}}{\Gamma}. \tag{19}$$

From Equation 19, $\mathbf{C_{est,n}}$ becomes $\mathbf{C_{est}}$ if and only if the noise-related second term becomes 0. Therefore, to remove errors in all concentrations, the following equation needs to be minimized:

$$\left\|\boldsymbol{\varepsilon}^{+}\boldsymbol{\Phi}_{\mathbf{D}}^{-1}\mathbf{n}\right\|. \tag{20}$$

Then, since $\mathbf{n}$ is a random variable (zero-mean Gaussian noise), Equation 20 can be modified as

$$\left\|\boldsymbol{\varepsilon}^{+}\boldsymbol{\Phi}_{\mathbf{D}}^{-1}\mathbf{1_M}\right\|, \tag{21}$$

where $\mathbf{1_M}$ is an *M*-by-1 vector containing all 1's. Our goal is to find a set of wavelengths that minimizes the Equation 21 under the given number of wavelengths (*M*). In other words, a set of wavelengths minimizing Equation 21 (i.e., the noise-related second term in equation (9)) makes $\mathbf{C_{est,n}}$ as close as to $\mathbf{C_{est}}$ (i.e., the noise-free ideal concentration estimates). In addition, it is clear that the Equation 21 relies on two quantities: $\boldsymbol{\varepsilon}^{+}$ (i.e., the pseudoinverse of absorption cross-section matrix) and $\boldsymbol{\Phi}_{\mathrm{D}}^{-1}$ (i.e., the inverse of diagonal fluence matrix). Given the absorbers of interest, the absorption cross-section matrix can be assumed to be known, but the fluence matrix is generally unknown. Thus, in order to solve the Equation 21, the fluence matrix should be modeled in practice. In this study, a Monte Carlo model was used to model the fluence as described below in the following section. Note that accurate modeling of fluence distribution still remains a concern, which impacts

the accuracy of our method. In the minimization process, because the wavelengths typically used in sPA imaging are finite and discrete (wavelengths from 680 nm to 970 nm with a one nm step size are used in this study), every possible set of wavelengths was applied to find an optimal set of wavelengths where the objective function (i.e., Equation 21) is globally minimized. Here, note that $\boldsymbol{\varepsilon}^{+}\boldsymbol{\Phi}_{\mathbf{D}}^{-1}$ in Equation 21 can be rewritten as $(\boldsymbol{\Phi}_{\mathbf{D}}\boldsymbol{\varepsilon})^{+}$ and the term $\boldsymbol{\Phi}_{\mathbf{D}}\boldsymbol{\varepsilon}$ is maximized in the method to minimize the noise-related error in solving a spectral unmixing problem. Here, note that after a set of optimal wavelengths is selected by this approach, any spectral unmixing methods can be applied to obtain the concentrations of chromophores.

3.3.2 Monte Carlo Study Parameters

To investigate our approach under various conditions, the recently introduced MC program (mcxyz.c) [109] was used, which allows us to obtain precise optical fluence maps, including a blood vessel with various SO_2 levels. Figure 11 shows tissue models that consist of air, epidermis (600-μm-thickness), dermis (with a blood volume fraction of 0.2 %), and blood. The blood vessel (500-μm-diameter) was placed at three depths (0.4 cm, 1.0 cm, and 1.6 cm) with five SO_2 levels (0.00, 0.25, 0.50, 0.75, and 1.00). Here, the SO_2 level of blood in dermis is the same as that in the blood vessel. The laser beam applied was uniform and had a radius of 0.4 cm. Figure 12 shows the absorption coefficients of oxy-, deoxy-hemoglobin, water, and melanin used in our study. For oxy- and deoxy-hemoglobin, typical values of the concentration ratio of hemoglobin in blood (150 g/L) and molecular weight of hemoglobin (64,500 g/mol) were used. The software and the detailed optical parameters of the tissue model, including anisotropy, absorption, and scattering coefficients, were obtained from the OMLC website (please refer to makeTissueList.m and spectralLIB.mat files at https://omlc.org/software/mc/mcxyz/index.html). Tissue

parameters for epidermis, dermis, blood, air, and water used in this study were the same as those listed in the website while SO_2 levels were varied.

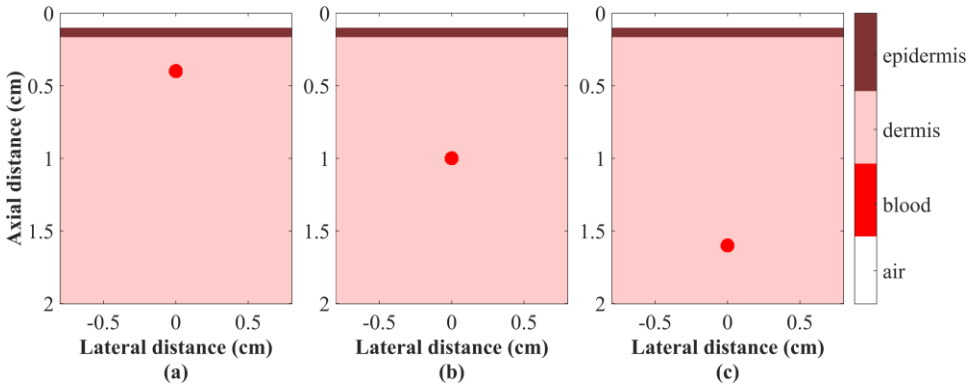

Figure 11 – Tissue models with air, epidermis, dermis, and 500-µm-diameter blood vessels at three depths: (a) 0.4 cm, (b) 1.0 cm, and (c) 1.6 cm.

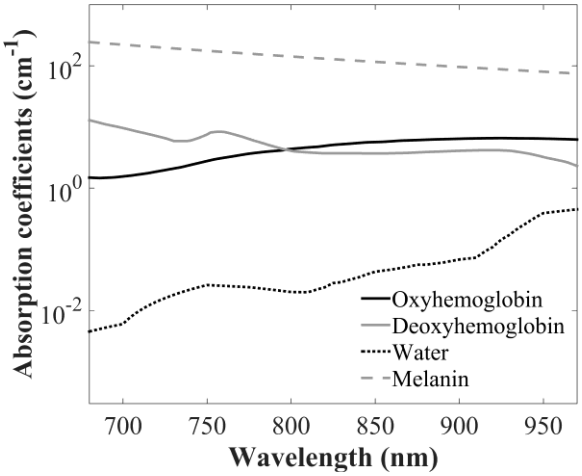

Figure 12 – Absorption coefficients of oxy- and deoxy-hemoglobin, water, and melanin (data obtained from the spectralLIB.mat file available at https://omlc.org/software/mc/mcxyz/index.html).

To collect the light fluence from the program, a three-dimensional array with 800x640x2 bins, each 25 µm was created. The optical wavelengths of light ranged from 680 nm to 970 nm with a one nm step size (thus, 291 wavelengths). Therefore, 291x5x3 light fluence maps corresponding to the number of wavelengths, SO_2 levels, and vessel positions, respectively were acquired. Each simulation time of the light fluence of an individual wavelength was 90 minutes (resulting in an average number of photons of

$1.5x10^6$), so this study required a 291x5x3x1.5-hour simulation. To expedite the simulation, 15 cores of an Intel Xeon processor (Intel Corp., Santa Clara, CA) were utilized simultaneously, allowing us to simulate all fluence maps in 291x1.5 hours. Overall, the MC program was used to acquire various optical fluence maps with multiple wavelengths (680 nm to 970 nm), five SO_2 levels (0.00, 0.25, 0.50, 0.75, and 1.00), three depths of a blood vessel (0.4 cm, 1.0 cm, and 1.6 cm), which took approximately 18 days.

3.3.3 Data Handling

After obtaining optical fluence maps, the fluence signals in each blood vessel at each individual wavelength were first averaged and one-dimensional optical fluence spectra with respect to the wavelength was constructed. Then, the averaged optical fluence signals were multiplied by the known absorption coefficients, which reconstructs the PA spectrum. To build the noise-added PA spectrum as in Equation 16, various amounts of zero mean white Gaussian random noise were generated and added to the reconstructed PA spectrum. In this study, we used the simple noise model by assuming the frequency response of the transducer is ideally flat as typically adopted in other studies for brevity [111, 112]. Here, the standard deviations (STD) of noise ranged from 0.0 to 0.1, which results in a reasonably wide range of the signal-to-noise ratio (SNR) in the PA spectrum (about 10.7 dB to 85.1 dB. See Figure 17.). In addition, to obtain statistical results, adding this random noise onto the PA spectrum and estimating concentrations were repeated 10^4 times.

3.3.4 Assessment

For the quantitative evaluation, this study used the root-mean-squared error (RMSE) of the concentration estimates (i.e., the concentrations of oxy-hemoglobin (HbO_2), deoxy-hemoglobin (Hb)) as follows:

$$\mathrm{RMSE} = \sqrt{\frac{\sum_i^T \left(C_{est,n}(i) - C(i)\right)}{T}}, \tag{22}$$

where $C_{est,n}$ represents a concentration estimate, C is a ground-truth concentration set in the MC simulation, and T is the number of noise trials (here, T=10^4). Note that $C_{est,n}$ in Equation 22 is any element of $\mathbf{C_{est,n}}$ in Equation 19. The RMSE of two estimates: the concentrations of HbO_2 and Hb used to quantify SO_2 at various vessel depths and SO_2 levels as a function of the noise STD were computed. To investigate the robustness of our method under the various amounts of noise, the white Gaussian random noise was repeatedly applied.

In this study, M was set to two (i.e., the minimum number of wavelengths to identify the distribution of two chromophores). Given this condition, we compared two wavelength selection methods: the proposed noise minimization approach and the previous minimum singular value-based approach [99]. Here, these methods are referred to as $n_{\min}$, and $\sigma_{\min}$, respectively. In addition, we applied two methods to reconstruct concentrations: linear least squares with non-negativity constraints (the lsqnonneg function in MATLAB) and without any constraints (referred to as CLLS and LLS, respectively). Although two linear least squares methods were used in this research, both wavelength selection methods are not restricted to any spectral unmixing method. In summary, two wavelength selection approaches ($n_{\min}$ and $\sigma_{\min}$) with and without non-negativity constraints (thus, total four methods) were used to estimate the concentrations of HbO_2 and Hb at three depths of a vessel and five SO_2 levels as a function of noise levels. For quantitative comparisons, the RMSE of the estimates and the average of corresponding SO_2 were computed.

3.4 Results and Discussion

Figure 13, Figure 14, and Figure 15 show the optical fluence maps containing a blood vessel at three depths: 0.4 cm, 1.0 cm, and 1.6 cm. All the fluence maps (in the unit

of J/cm^2 per J delivered or 1/cm^2) are displayed on a logarithmic scale. The rows of each figure represent the fluence maps of three representative optical wavelengths (680 nm, 875 nm, and 970 nm) selected from 291 maps, which range from 680 nm to 970 nm with a 1-nm step size. The columns represent five SO_2 levels (0.00, 0.25, 0.50, 0.75, and 1.00) in blood vessels. Figure 13, Figure 14, and Figure 15 show that the optical fluence varies according to the optical wavelength and the SO_2 level. These variations in the fluence indicate that the choice of wavelengths affects the strength of the fluence, which determines the SNR. Furthermore, because of light attenuation, the deeper the vessel is located in tissue, the more the overall fluence decreases. Therefore, the optical wavelength selection becomes more challenging and crucial, particularly when imaging deeply located targets.

To investigate the wavelength- and depth-dependent characteristics of optical fluence, we first averaged the fluence signals of each individual wavelength within each blood vessel as one-dimensional optical fluence functions with respect to wavelengths (Figure 16). According to optical wavelength, SO_2, and depth, the fluence signals vary substantially. As a notable example, the fluence patterns of 0.4-cm and 1.6-cm vessels clearly differ. In contrast to the fluence at the 0.4-cm vessel, the fluence at the 1.6-cm vessel abruptly decreases and becomes negligible as the wavelength increases. This observation suggests that avoiding using higher wavelengths (> 950 nm) when estimating SO_2 in the far region is desirable.

To construct the noise-added PA spectra in Equation 16 and to investigate the robustness of our approach, we added various amounts of white Gaussian random noise to PA spectra reconstructed from the averaged one-dimensional fluence signals and the known absorption coefficients. The standard deviations (STDs) of noise spanning from 0 to 0.1 created the wide range of SNR. We repeated this process 10^4 times to find the mean SNRs of the PA spectra. Figure 17 shows the mean SNRs over the noise STD. As the noise STD increases, the mean SNRs decrease. In addition, three mean SNR functions are plotted

according to three depths of a vessel. The deeper the vessel, the more SNR decreases. After all, we use these noise-added PA spectra to assess two wavelength selection methods ($n_{\min}$ and $\sigma_{\min}$).

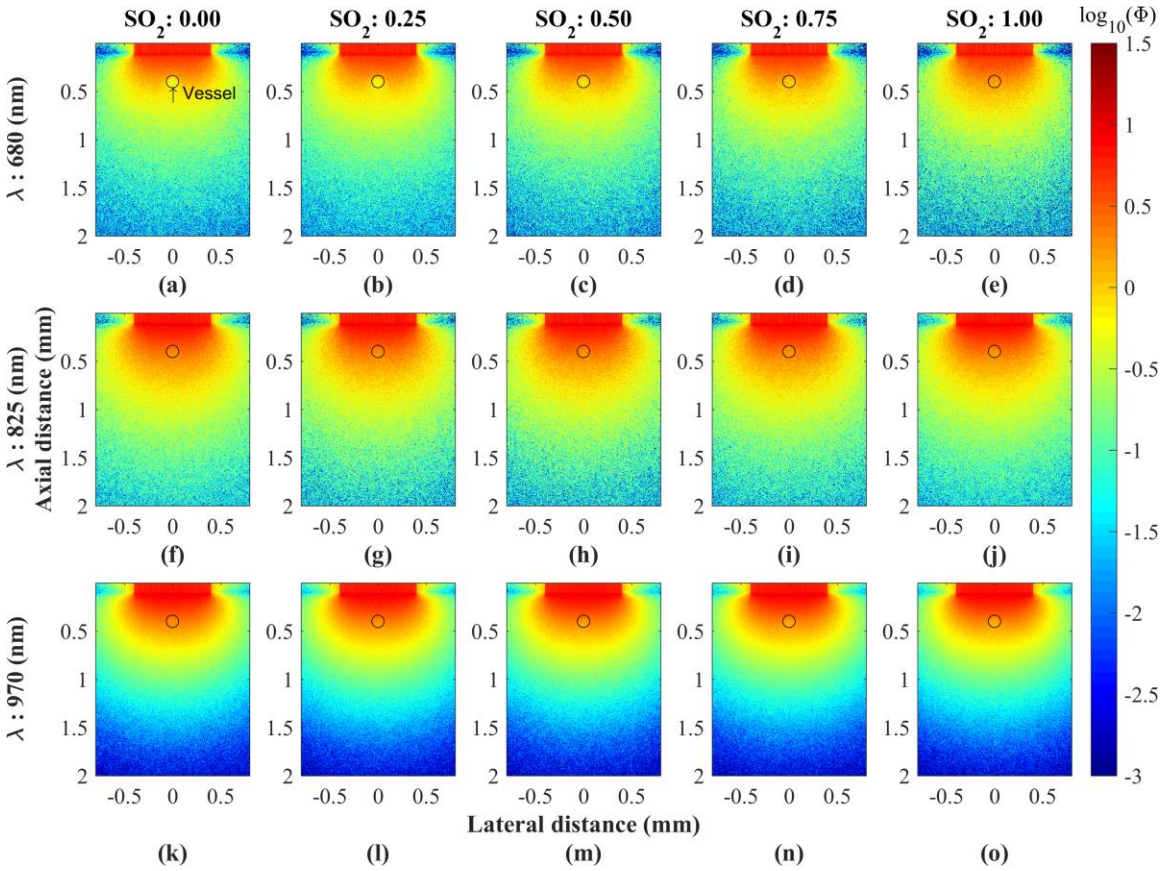

Figure 13 – Representative optical fluence maps of the tissue model containing a blood vessel at a 0.4 cm depth. Rows represent wavelengths of light, 680, 875, and 970 nm, and columns represent five levels of oxygen saturation in the blood vessel, 0.00, 0.25, 0.50, 0.75, and 1.00. The unit of fluence Φ is J/m^2 per J delivered or 1/m^2.

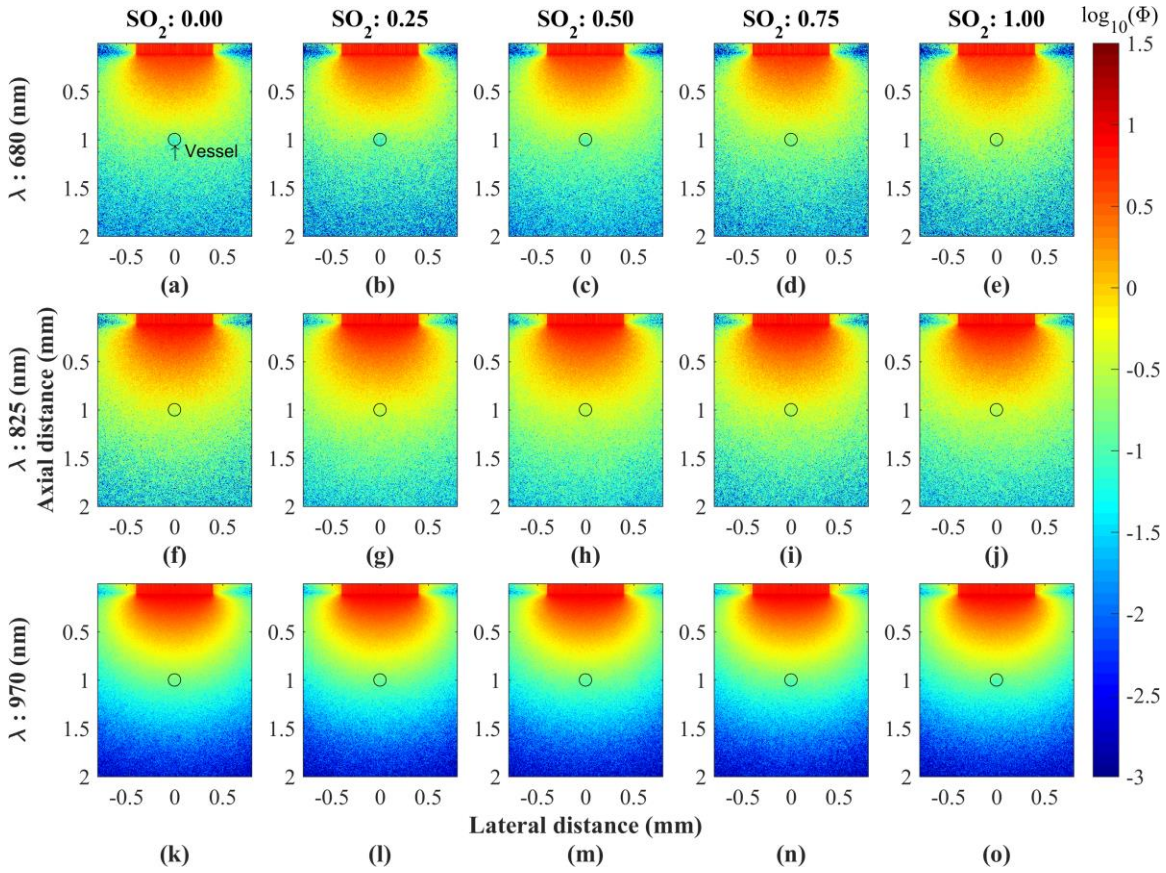

Figure 14 – Representative optical fluence maps of the tissue model containing a blood vessel at a 1.0 cm depth. Rows represent wavelengths of light, 680, 875, and 970 nm, and columns represent five levels of oxygen saturation in the blood vessel, 0.00, 0.25, 0.50, 0.75, and 1.00. The unit of fluence Φ is J/m^2 per J delivered or 1/m^2.

To estimate two concentrations of HbO_2 and Hb to quantify SO_2 levels, this study uses two optical wavelengths (M=2, the minimum number of wavelengths to solve the optical inverse problem.) selected by the proposed and the previous methods: $n_{\min}$ and $\sigma_{\min}$. $n_{\min}$ finds two wavelengths that minimize the added noise term whereas $\sigma_{\min}$ finds two wavelengths that maximize the minimum singular value of the absorption cross-section matrix. Therefore, the former minimizes the noise-related errors, and the latter allows the selected absorption cross-section matrix to have unique spectral features. As a result, $\sigma_{\min}$ selects two wavelengths: 680 nm and 970 nm. Here, since $\sigma_{\min}$ relies on only the stability of absorption cross-section matrix, we use the same set of wavelengths, regardless of the

depth or the concentration of chromophores. However, since n_{min} exploits the optical fluence distribution and the optical fluence varies according to the imaging depth or the concentration of absorbers, our approach adaptively offers optimal sets of wavelengths as presented in Table 6.

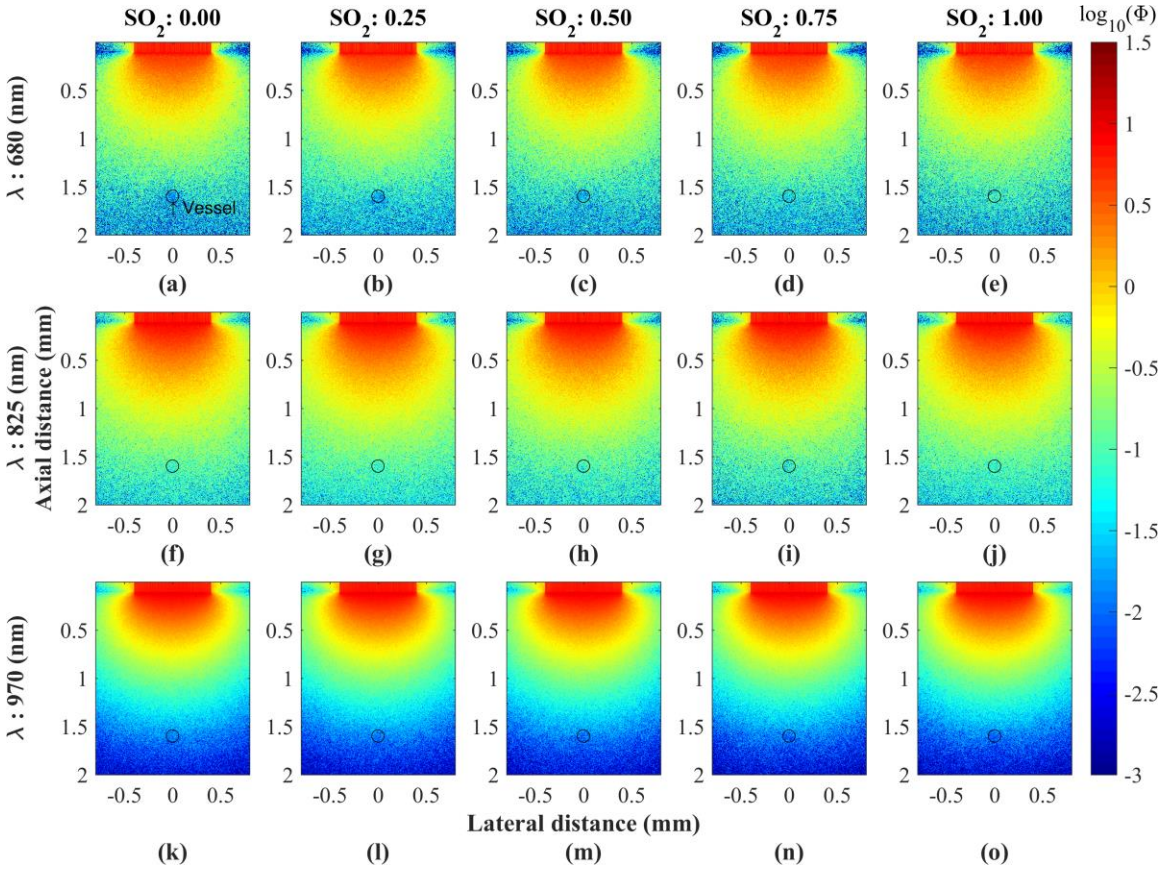

Figure 15 – Representative optical fluence maps of the tissue model containing a blood vessel at a 1.6 cm depth. Rows represent wavelengths of light, 680, 875, and 970 nm, and columns represent five levels of oxygen saturation in the blood vessel, 0.00, 0.25, 0.50, 0.75, and 1.00. The unit of fluence Φ is J/m^2 per J delivered or 1/m^2.

Table 6 describes the selected sets of wavelengths via the proposed method (n_{min}). First, where the vessel depth is 0.4 cm, the PA spectrum has relatively high SNR as shown in Figure 17, and the optical fluence hardly fluctuates or decreases over the wavelength as shown in Figure 16. Therefore, most of the sets of wavelengths (first column in Table 6)

are similar to those (680 nm and 970 nm) chosen by σ_{min}. Nevertheless, small shifts in the wavelength are observable. As SO_2 decreases from 1.00 to 0.00, the optical fluence at 680 nm decreases. Hence, n_{min} tends to select the wavelength with higher optical fluence to satisfy the Equation 21. As a result, the first wavelength increases from 681 nm to 692 nm as SO_2 changes from 1.00 to 0.00. The second wavelengths used for the 0.4-cm vessel mostly remain at around 970 nm, except when SO_2 is 1.00. Since the optical fluence at 970 nm decreases gradually when SO_2 increases. Thus, when SO_2 is 1.00, the wavelength moves to 909 nm, which indicates that the gain in the optical fluence starts to outweigh the loss in spectral distinction. Similarly, as the depth of a vessel increases, n_{min} selects shorter wavelengths as the second wavelengths.

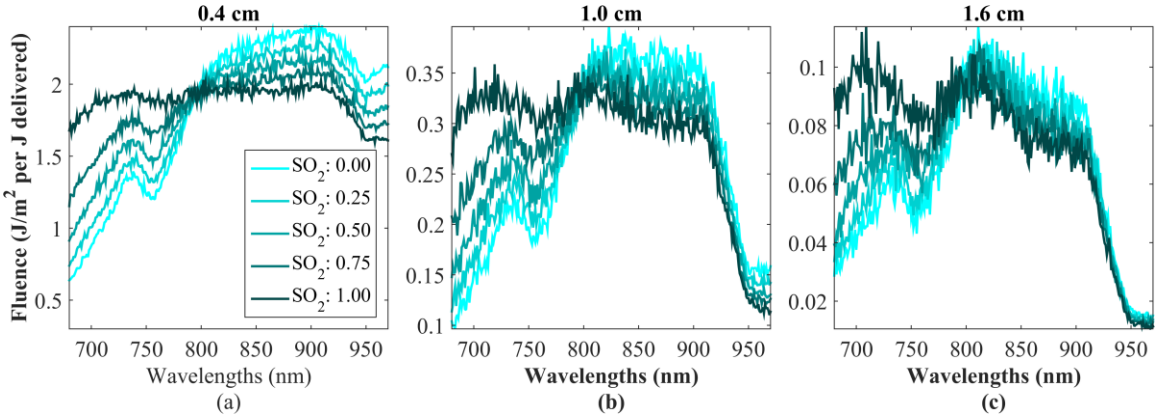

Figure 16 – One-dimensional averaged optical fluence signals in three vessel depths at (a) 0.4 cm, (b) 1.0 cm, and (c) 1.6 cm at 0 cm in the lateral direction as a function of wavelength.

Figure 18 and Figure 19 show the RMSE of estimated HbO_2 and Hb concentrations under various SO_2 levels and vessel depths. This study uses two wavelength selection methods (n_{min} and σ_{min}) with two constraints (with and without the non-negativity constraint) (i.e., four methods: n_{min}+LLS, n_{min}+CLLS, σ_{min}+LLS, and σ_{min}+CLLS). The RMSE is negligible in both HbO_2 and Hb at the 0.4-cm depth vessel, since as illustrated in

Figure 17, the overall SNR is sufficiently large at 0.4 cm over all wavelengths (> 40 dB). Furthermore, since the choices of wavelengths by two wavelength selection methods ($n_{\min}$ and $\sigma_{\min}$) are almost identical when the vessel is located at 0.4 cm, the RMSE differences between the two methods are minor, except when SO_2 is 1.00. However, the deeper the vessel is located, the more the overall SNR decreases, and thus, the RMSE becomes larger. In addition, from the 1.6-cm vessel, we can observe the largest gap between the RSME of the two wavelength selection methods, which suggests that the wavelength choice is critical in far-depth imaging. Commonly, the non-negativity constraint (CLLS) produces more precise estimates in terms of RMSE.

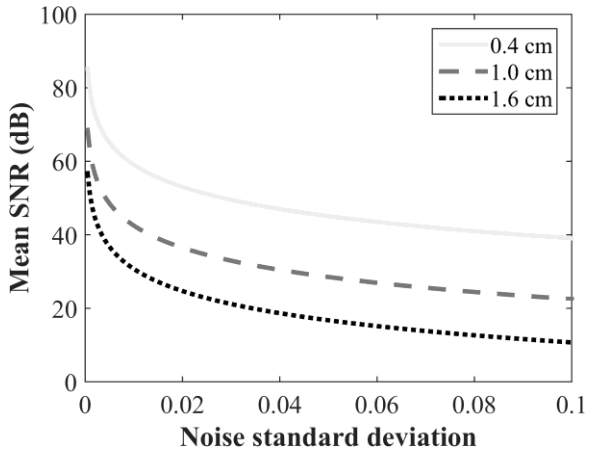

Figure 17 – Mean SNRs of PA spectrum in blood vessels at three depths (0.4 cm, 1.0 cm, and 1.6 cm) as a function of noise STD.

In Figure 20, we compute mean SO_2 levels from the concentration estimates of HbO_2 an Hb. Here, since any negative estimate in the concentration of HbO_2 or Hb causes amplified or negative SO_2 values, the non-negativity constraint is desirable in the estimation of SO_2. However, the non-negativity constraint results in a bias in SO_2 when SO_2 is 0.00 or 1.00. Overall, as the vessel depth increases, the accuracy in mean SO_2 levels degrades, shown in Figure 10. Particularly, when the noise STD is larger than 0.01 at the

1.6-cm vessel (that is, SNR < 30 dB), the σ_{min} method without the non-negativity constraint (i.e., σ_{min}+LLS) fails to reconstruct reliable SO_2 levels. The non-negativity constraint partially improves accuracy but still yields substantial errors. However, n_{min} stably measures SO_2 levels regardless of vessel depths, constraints, and concentrations.

Table 6 – Two (M=2) selected wavelengths (nm) used for estimating SO_2 by the proposed approach (n_{min}) at three Vessel depths under five SO_2 levels.

SO_2	Vessel depth		
	0.4 cm	1.0 cm	1.6 cm
0.00	692, 970	688, 895	681, 882
0.25	694, 969	683, 887	687, 887
0.50	683, 970	684, 909	693, 881
0.75	681, 970	680, 906	684, 878
1.00	681, 909	682, 887	680, 893

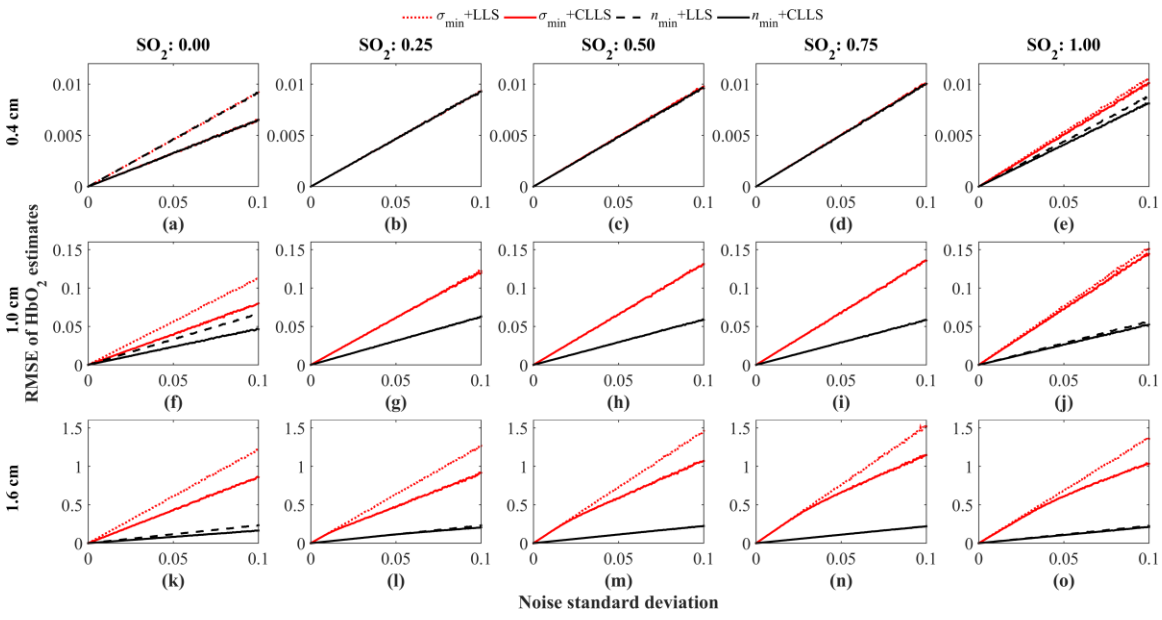

Figure 18 – RMSE of estimated HbO_2 concentrations from four methods: σ_{min}+LLS, σ_{min}+CLLS, n_{min}+LLS, and n_{min}+CLLS with respect to the noise STD. Rows represent three vessel depths (0.4 cm, 1.0 cm, and 1.6 cm). Columns represent five levels of SO_2 (0.00, 0.25, 0.50, 0.75, and 1.00).

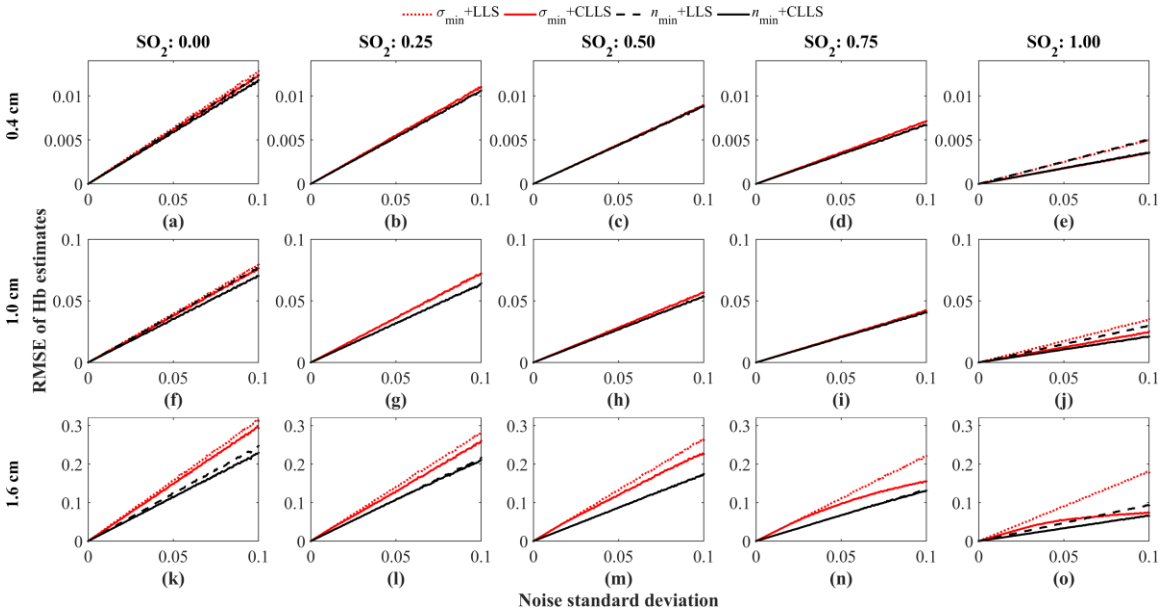

Figure 19 – RMSE of estimated Hb concentrations from four methods: σ_{min}+LLS, σ_{min}+CLLS, n_{min}+LLS, and n_{min}+CLLS with respect to the noise STD. Rows represent three vessel depths (0.4 cm, 1.0 cm, and 1.6 cm). Columns represent five levels of SO_2 (0.00, 0.25, 0.50, 0.75, and 1.00).

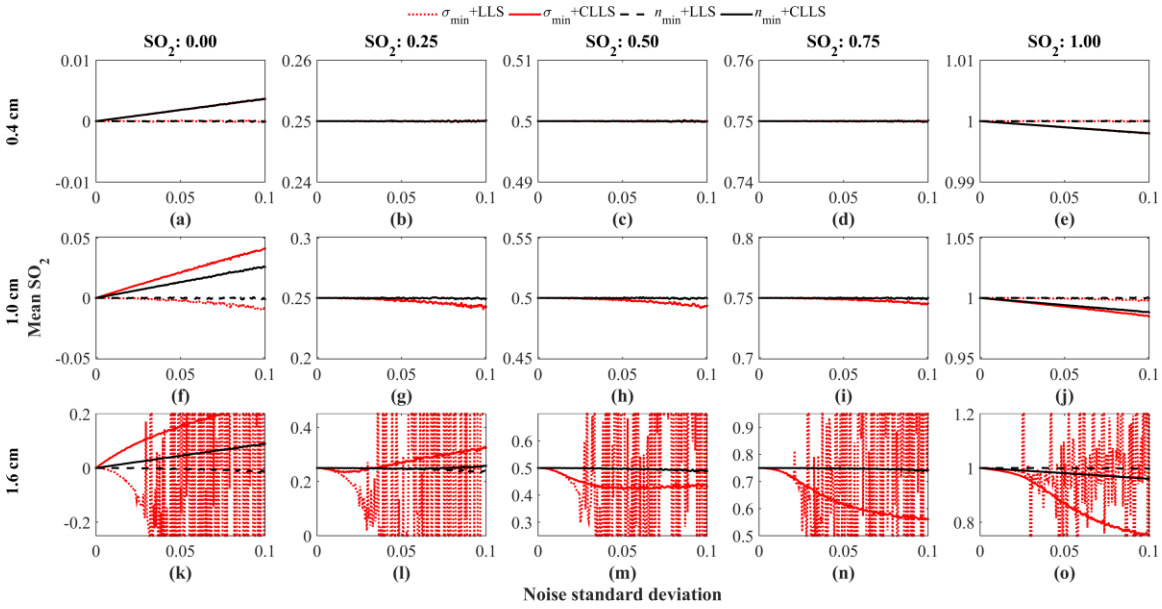

Figure 20 – Estimated mean SO_2 by four methods: σ_{min}+LLS, σ_{min}+CLLS, n_{min}+LLS, and n_{min}+CLLS with respect to the noise STD. Rows represent three vessel depths (0.4 cm, 1.0 cm, and 1.6 cm). Columns represent five levels of SO_2 (0.00, 0.25, 0.50, 0.75, and 1.00).

We investigated the effect of the choice of optical wavelengths in the estimation of SO_2 using sPA imaging in the presence of wavelength-dependent, spatially-variant fluence through the simulation. Different amount of additive white random noise was applied to demonstrate the changes in desired optical wavelengths, showing that the current method outperforms the previous method especially when the SNR is low (i.e., the noise STD is high). In addition, the wavelength choices in Table 6 indicate that for deeper vessel (i.e., the SNR becomes lower), the wavelengths selected with our method are increasingly different from those estimated using the previous method, resulting in improved accuracy in SO_2 estimation (note that the wavelength sets in Table 6 are only optimal in our simulation settings, not optimal in general). Thus, for sPA images with low signal and/or high noise, our method finds a more optimal set of optical wavelengths. However, the noise model used in our study does not reflect all noise components present in sPA imaging. Thus, a future study should include other noise sources, such as thermal acoustic noise from the medium and thermal noise from the transducer, to make the model more realistic [113].

The results clearly show that the imaging depth and tissue properties play a significant role in the optimal wavelength selection for sPA imaging. As researchers seek to reduce the cost and/or improve the temporal resolution of sPA imaging systems, using only small subset of the optical spectrum is an appealing option. In practice, the specific choice of imaging wavelengths is nontrivial and application-dependent. In this work, we assumed that the optical fluence distribution is known. In this case, our method selects wavelengths capable of achieving accurate sPA images of hemoglobin relatively deep in tissue. In practice, because spatially-varying optical properties of tissue are unknown, successful modeling of the optical fluence distribution is often challenging and requires several assumptions, such as the number and a type of absorbers and the scattering coefficients. Therefore, the selected wavelengths found by our method likely to be

suboptimal. These results indicate that extensive analysis of a variety of tissue properties must be performed prior to selecting a subset of the available wavelengths. One additional consideration is the maximum safe level of laser exposure [114]. In the wavelength range from 680 nm to 970 nm, longer wavelengths allow us to use higher laser energy and achieve higher SNR, which could result more accurate sPA images.

This study assumed that the acoustic inversion problem to reconstruct the local PA spectrum from the received PA spectrum can be solved. However, to reconstruct acoustic pressure generated in local absorbers accurately, we should consider heterogeneous tissue, bandlimited ultrasound detectors, and other physical limitations [108]. In reality, the heterogeneity of tissue may cause variations in the speed of sound, resulting in phase aberration [115]. This degrades the image quality as well as the accuracy in concentration estimation. Thus, the accurate modeling of non-homogenous tissue properties should be considered when reconstructing PA images. In addition, because the received PA signals are inherently wide band and noisy, the sensitivity of the ultrasound transducer is crucial. The limited bandwidth and SNR of the PA spectrum affect the resolution and the accuracy of SO_2 estimation [43]. Furthermore, because of frequency-dependent attenuation of acoustic waves, as the imaging depth increases, the center frequency of the acoustic wave downshifts and its bandwidth becomes narrow, degrading the resolution and the SNR. Moreover, using data acquired with a linear array transducer, the limited-view tomographic reconstruction leads to the artifacts in the local PA reconstruction. Finally, the reverberation artifact (or reflection artifact), mainly caused by strong PA signals generated from superficial optical absorbers, is another issue in sPA imaging because it significantly limits the image contrast and the imaging depth [116].

3.5 Conclusion

Through the simulation study, we have shown that the wavelength selection for the SO_2 estimation in sPA imaging is affected by the corresponding wavelength-dependent optical fluence distribution. To improve the SO_2 estimation capability, this chapter has introduced the depth-optimized wavelength selection method, which allows us to obtain the concentration estimates with higher accuracy. Assuming that the wavelength-dependent, spatially-variant optical fluence distribution can be reliably obtained, this approach finds a set of wavelengths, which minimizes the noise-related errors in the concentration estimates. Through the MC simulation of light propagation in tissue, we have investigated the effect of various imaging parameters, including the depth and the concentrations of chromophores. The quantitative assessment using RMSE showed that the proposed approach robustly and accurately estimated SO_2 over the previous method. This study indicates that the choice of wavelength in sPA imaging is critical, and our depth-optimized method could be effective, especially when quantifying deeper agents.

CHAPTER 4. CONTRAST-ENHANCED ULTRASOUND IMAGING IN VIVO WITH LASER-ACTIVATED NANODROPLETS

This chapter introduces a real-time contrast-enhanced ultrasound imaging method with recently developed laser-activated nanodroplets (LANDs), a new class of phase-change nanometer-scale contrast agents that provides perceptible, sustained high-contrast with ultrasound. In response to pulsed laser irradiation, the LANDs—, which contain liquid perfluorohexane and optical fuses—blink (vaporize and recondense). That is, they change their state from liquid nanodroplets to gas microbubbles, and then back to liquid nanodroplets. In their gaseous microbubble state, the LANDs provide high-contrast ultrasound, but the microbubbles formed *in situ* typically recondense in tens of milliseconds. As a result, LAND visualization by standard, real-time ultrasound is limited. However, the periodic optical triggering of LANDs allows us to observe corresponding transient, periodic changes in ultrasound contrast. This study formulates a probability function that measures how ultrasound temporal signals vary in periodicity. Then, the estimated probability is mapped onto a B-scan image to construct a LAND-localized, contrast-enhanced image. We verified our method through phantom and *in vivo*

experiments using an ultrasound system (Vevo 2100, FUJIFILM VisualSonics, Inc., Toronto, ON, Canada) operating with a 40-MHz linear array and interfaced with a 10 Hz Nd:YAG laser (Phocus Mobile, Opotek Inc., Carlsbad, CA, USA) operating at the fundamental 1064 nm wavelength. From the phantom study, the results showed improvements in the contrast-to-noise ratio of our approach over conventional ultrasound ranging from 129% to 267%, with corresponding execution times of 0.10 to 0.29 s, meaning that the developed method is computationally efficient while yielding high-contrast ultrasound. Furthermore, *in vivo* sentinel lymph node (SLN) imaging results demonstrated that our technique could accurately identify the SLN. The results indicate that our approach enables efficient and robust LAND localization in real time with substantially improved contrast, which is essential for the successful translation of this contrast agent platform to clinical settings.

4.1 Introduction

Cancer is the second leading cause of death in the United States, and most cancer-related deaths are highly associated with metastasis [117, 118]. Therefore, detecting and assessing the sentinel lymph node (SLN), which is the first lymph node to which cancer cells drain from a primary tumor, is crucial. To identify the SLN, researchers have explored numerous biomedical imaging techniques [41, 98, 119-124]. Classically, lymphoscintigraphy with radiocolloid injection has been widely used for preoperative lymph node imaging, but its imaging resolution is relatively low [121]. Magnetic resonance imaging (MRI) has shown promising results for nodal staging, but MRI is not cost effective and imaging lymph nodes during surgery and/or biopsies is challenging [122]. In addition, although positron emission tomography/computed tomography (PET/CT) has shown

potential in preoperative scanning of lymph nodes, its sensitivity and specificity in identifying SLN is lower than those of lymphoscintigraphy or MRI [125]. Ultrasound is a cost-effective and non-invasive imaging modality that is able to guide SLN biopsies in real-time. Although ultrasound can be used to identify lymph nodes, the contrast between lymph nodes and the surrounding background is limited, and ultrasound alone cannot visualize which node receives drainage from the tumor. Accordingly, microbubbles have been used to improve contrast, but their relatively large size (a few microns) impedes their influx into the lymph node [126, 127]. In addition, their circulation time is relatively short (a few minutes), limiting the duration of imaging sessions [45].

To address these limitations of microbubbles, phase-changing nanodroplets that can be activated either acoustically or optically have been intensively investigated [48, 49, 128-131]. Because they remain in a stable liquid state until they are triggered, nanodroplets can circulate relatively longer and remain small enough to extravasate from tumor neovasculature. Once vaporized in response to an acoustic or optical trigger, nanodroplets become gaseous microbubbles, providing high-contrast ultrasound similar to conventional microbubbles. However, because nanodroplets usually consist of low-boiling-point materials (e.g., perfluoropentane (29°C) or perfluorobutane (−1°C)), they do not recondense back to the original liquid state after activation. More recently, our group and others have developed laser-activated nanodroplets (LANDs) containing liquid perfluorohexane and optical dye. LANDs repeatedly vaporize and recondense because the boiling point of perfluorohexane (56°C) is higher than physiological temperature (37°C) [55, 132, 133]. This unique, repeatable phase-changing property of LANDs has enabled or improved many applications, including super-resolution imaging, background-free

imaging, and photoacoustic imaging [55, 132, 133]. Figure 21 shows the blinking dynamics of the LANDs. Before optical triggering, the LANDs remain liquid nanodroplets, producing very limited ultrasound echoes. However, once activated by pulsed laser irradiation, the LANDs rapidly vaporize into gaseous microbubbles *in situ*, generating hyperechoic ultrasound signals until the LANDs completely recondense [49, 55, 129, 133]. However, their gaseous period is relatively transient (several to hundreds of milliseconds), which limits human perception of LAND-based contrast [133].

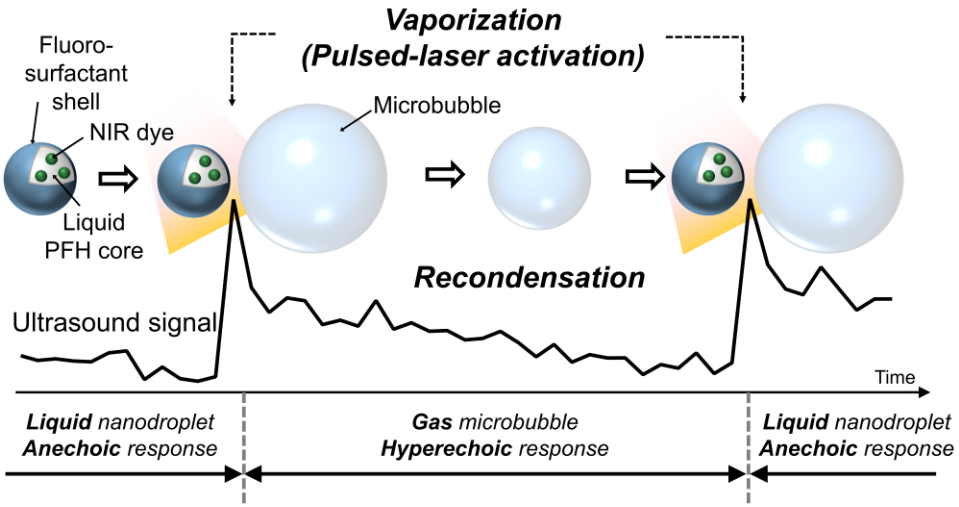

Figure 21 – Vaporization and recondensation of laser-activated nanodroplets (LANDs) in response to an optical trigger. When activated, LANDs immediately produce strong ultrasound signals, which decrease as the LANDs recondense to native, liquid droplets.

To overcome this limitation and to provide perceptible, sustainable LAND-based contrast in ultrasound, this work has developed an imaging method that effectively localizes the LANDs with high frame rate ultrasound imaging. In the method, we activate the LANDs periodically and capture the periodic blinking LANDs in ultrasound images, enabling the development of a fast, robust LAND-localization algorithm.

4.2 Materials and Methods

4.2.1 Localization of Perfluorohexane Nanodroplets (PFHnDs)

This study introduces a novel, contrast-enhanced imaging method that uses high frame rate ultrasound imaging to localize LANDs. This real-time imaging method is clinically applicable and provides superior contrast to conventional ultrasound. As illustrated in Figure 22, our approach is based on LAND injection and optical activation, both of which are essential to the creation of contrast-enhanced LAND frames. Before injecting LANDs and initiating the laser, no localized LANDs are observable in contrast-enhanced frames. Without an optical trigger, localized LAND frames produce nearly imperceptible contrast because the LANDs have not vaporized and thus remain liquid droplets. However, once the pulsed laser irradiates local tissue containing LANDs, the vaporized particles become hyperechoic, allowing for construction of contrast-enhanced LAND images (yellow frames in Figure 22). The recondensation process, however, is relatively fast; so to provide sustained contrast-enhanced imaging, this method uniquely exploits the periodic, repeated blinking in our LAND-localization algorithm. Overall, our imaging protocol reconstructs contrast-enhanced LAND image frames from the acquired ultrasound data at the rate of the pulse repetition frequency (PRF) of the laser. Fortunately, it does not require any sophisticated synchronization between the laser and the ultrasound systems, indicating that this approach is not limited in its utility. Until several laser pulses (usually, 3 to 5) activate the LANDs, it is only possible to build incomplete, transient LAND frames (blue). Yet after triggering several times, fully contrast-enhanced LAND frames (green) can be achieved.

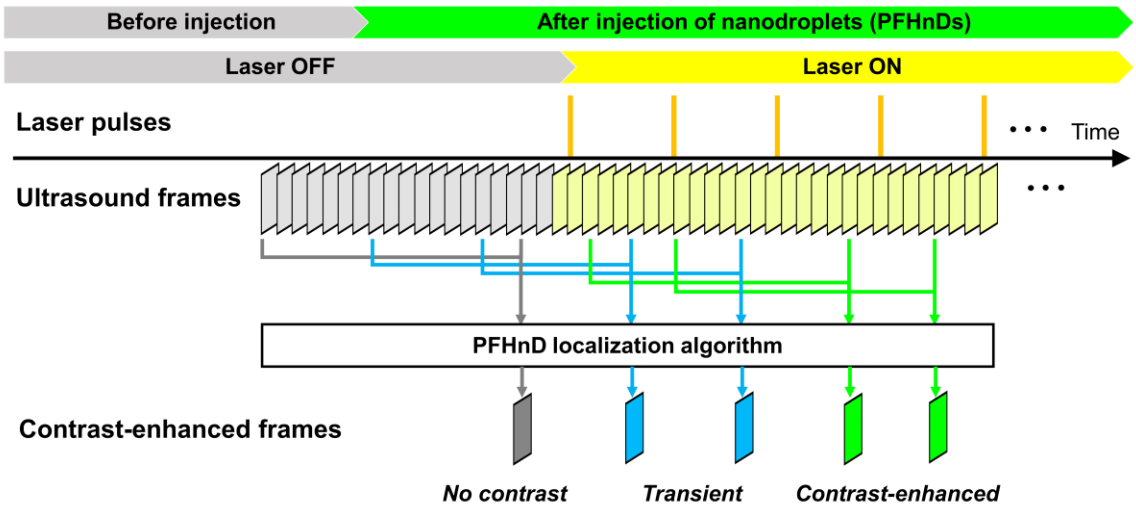

Figure 22 – An imaging configuration for the localization of LANDs. After both injecting and triggering LANDs, this algorithm can reconstruct contrast-enhanced LAND image frames at the pulse repetition frequency of a laser system.

The crux of the LAND localization method is that if a pixel in an image contains LANDs and the PRF of the laser pulses is constant, then we can induce repeated, periodic blinking of LANDs corresponding to this PRF. Thus, the temporal ultrasound signal for this pixel will contain regularly spaced peaks if the frame rate of ultrasound is also kept constant. The localization method assesses the consistency of the resultant peaks in ultrasound frames after tissue has been irradiated with multiple laser pulses. The PRF of the laser is defined as M and the frame rate of ultrasound is defined as R. Thus, every N frames (N=R/M) a single strong signal peak from the optically triggered LANDs is observed, as this corresponds to the ultrasound frame at which the LANDs are vaporized. Therefore, when irradiating with L laser pulses, L peaks occur. These L peaks here are recorded in L sets of N ultrasound frames (i.e., $L{\cdot}N$ ultrasound frames contain L peaks). The positions of these peaks can be any integer between 1 and N, as every set consists of

N frames and one of these *N* frames will include the corresponding peak. For every pixel of interest in the image, the set *S*, containing *L* positions of peaks, is defined by

$$S = \{s_1, s_2, \dots, s_L\}, \tag{23}$$

where s_1, s_2, … , s_L are positions of peaks created by *L* number of laser pulses. Each peak is detected using a simple gradient operation. Then, a cost function with absolute differences of all two-combinations from *S* is defined by

$$e(i) = |s_j - s_k|, \qquad i = 1,2, \dots, \binom{L}{2}, \tag{24}$$

where *j* and *k* are 1, 2, …, *L* and $j \neq k$. The cost function *e*(*i*) in Equation 24 contains differences between peak positions from all possible pairs of two. Only image pixels containing the LANDs can present periodically blinking periodic ultrasound, which results in small *e*(*i*)'s because these peaks are detected repeatedly and consistently. Therefore, this method counts the number of *e*(*i*)'s less than or equal to *d*, where *d* is a threshold that determines the sensitivity of the algorithm, as *c*(*i*) by

$$c(i) = \begin{cases} 1, & if\ e(i) \leq d \\ 0, & otherwise \end{cases}, \qquad i = 1,2, \dots, \binom{L}{2}, \tag{25}$$

Finally, this method formulates a probability function P_{LAND} presenting the positional regularity of these peaks by

$$P_{PFHnD} = \frac{\sum_{i=1}^{\binom{L}{2}} c(i)}{\binom{L}{2}}, \tag{26}$$

where the denominator is the number of all two-combinations of L and the numerator is the number of two-combinations whose absolute difference is less than or equal to d. Thus, the probability function defined in Equation 26 represents how regularly peaks occur in the pixel of interest. In summary, to localize the LANDs for each pixel, this method measures how mutually close the detected L peaks are to temporal ultrasound sequences. The estimated probability in Equation 26 is displayed on each pixel of a contrast-enhanced LAND frame, indicating the localizability of LANDs.

4.2.2 Experimental Set-Up

We synthesized the LANDs, consisting of an optical dye (Epolight 3072, Epolin, Inc., Newark, NJ, USA), liquid perfluorohexane (FluoroMed, L.P., Round Rock, TX, USA), an aqueous fluorosurfactant (Zonyl FSO, Sigma-Aldrich, St. Louis, MO, USA), and deionized water, following detailed procedures from our previous work [133]. Briefly, we first dissolved 1 mg of dye in 250 μL of perfluorohexane solution and sonicated the solution for 30 s. Then, we mixed this solution and a mixture of 2.5 mL deionized water and 0.5 mL 1% v/v aqueous fluorosurfactant. We vortexed the solution for 10 s and sonicated it again for 5 minutes in a water bath. Finally, we washed the synthesized LANDs by centrifuging for 5 minutes at 1,000 relative centrifugal force (rcf) and resuspending in fresh deionized water. The diameter of the synthesized LANDs was 300 nm, as measured by a dynamic light scattering instrument (Zetasizer Nano ZS, Malvern Instruments, Malvern, Worcestershire, UK).

For our phantom and *in vivo* SLN imaging studies, we used a preclinical ultrasound system (Vevo 2100, FUJIFILM VisualSonics Inc., Toronto, ON, Canada) with a 40-MHz linear array transducer. The frame rate of ultrasound imaging was 288 Hz. To activate the LANDs, we used a 10-Hz Nd:YAG (neodymium-doped yttrium aluminium garnet) laser (Phocus, Opotek Inc., Carlsbad, CA, USA) at its fundamental 1064-nm wavelength, without synchronization with the ultrasound system. We acquired ultrasound images for approximately 2 s, and thus, several tens of laser pulses could be delivered per ultrasound acquisition. The measured optical fluence was 50 mJ/cm^2, far below the ANSI limit (100 mJ/cm^2) for safety [114].

We fabricated a tissue-mimicking phantom containing a cylindrical LAND-labeled inclusion and a homogeneous background. The phantom consisted of 21 mL of 40% polyacrylamide (Thermo Fisher Scientific, Walthan, MA, USA), 850 μL of 10% aqueous ammonium persulfate (Sigma-Aldrich, St. Louis, MO, USA) solution, 106 μL of TEMED (Sigma-Aldrich, St. Louis, MO, USA), 0.2% w/w silica particles (U.S. Silica, Hurtsboro, AL, USA), 0.01% w/w graphite particles (Dixon Ticonderoga, Lake Mary, FL, USA), and 64 mL of deionized water. Detailed procedures can be found in [133]. Only the inclusion contained 0.1% v/v LANDs. Our *in vivo* study was performed under protocols approved by the Institutional Animal Care and Use Committee at The University of Texas at Austin. A BALB/c nu/nu mouse (Charles River Laboratories, Inc., Wilmington, MA, USA) was anesthetized and injected submucosally through the tongue with 40 μL of LANDs using a 30-gauge needle. Then, we allowed the LANDs to drain for 30 minutes and imaged the cervical lymph nodes in the mouse's neck. After imaging, we immediately euthanized the mouse.

We collected two-dimensional ultrasound IQ sequences and processed the data with custom-written codes using MATLAB (The MathWorks, Inc., Natick, MA, USA). When reconstructing LAND frames, we varied the value of L (i.e., the number of sets of

ultrasound sequences used) to investigate how the choice of L affects the results. For the quantitative evaluation, we computed the contrast-to-noise ratio (CNR) values from B-scans alone and LAND-localized frames with two region-of-interests (inclusion and background) in the phantom as a function of L. We estimated 95% confidence intervals (CIs), where the number of replicates were 13, 11, 9, 7, and 5 with L of 3, 5, 7, 9, and 11, respectively. In addition, to assess the practicality of the method, we evaluated the execution times in MATLAB by repeating processing with 100 trials to obtain average running times and their 95% CIs. The size of image was 1168 by 148 pixels.

4.3 Results and Discussion

The top plot in Figure 23 shows a temporal profile of the linear ultrasound intensity measured on a pixel of the image containing LANDs. A corresponding movie is available online. The laser began pulsing at 0.4 s, and the pulse repetition interval of the laser was 0.1 s (i.e., 10 Hz). Thus, the repeated blinking behavior of LANDs was observable in the profile every 0.1 s from 0.4 s onward. In the figure, the algorithm allocated LAND frames (with L = 3 and 5) and their corresponding ultrasound frames every 0.1s. When L = 3, the image processing method was able to produce LAND frames at 0.3 s since it used three sets of ultrasound sequences to localize the LANDs. Equally, when L = 5, this method could generate LAND frames as soon as five sets of ultrasound sequences were collected (i.e., the number of ultrasound frames containing five laser pulses). Then, it continued generating LAND frames every 0.1 s (i.e., every laser pulse). However, note that even if a LAND image was constructed at 0.3 s when L was three, it yielded no contrast since the laser pulsing had not commenced. In addition, before three laser pulses were fired, LAND frames were incomplete, and so the two LAND frames at 0.4 s and 0.5s were incomplete, transient images. Finally, from 0.6 s onward, the algorithm was able to create fully contrast-enhanced LAND images. As a result, this method clearly localized the LAND-containing inclusion with L's of both three and five.

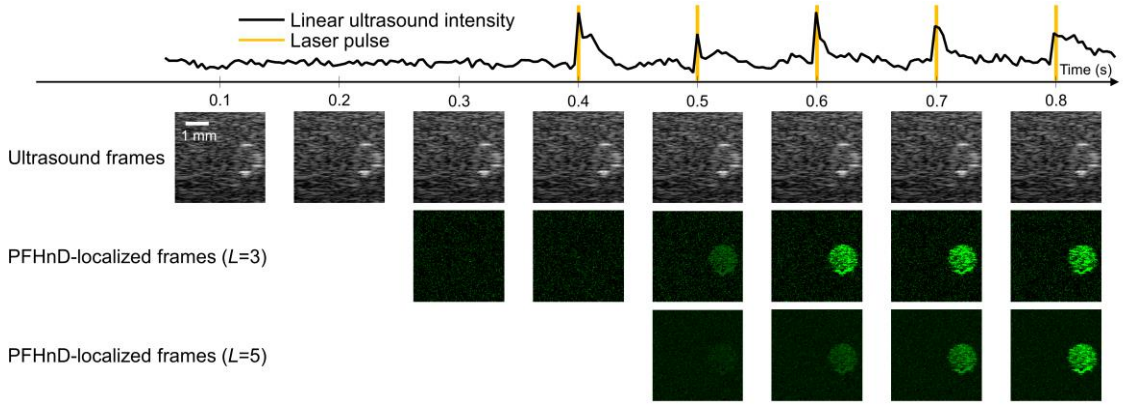

Figure 23 – Ultrasound and LAND-localized images acquired in the phantom, containing a LAND-labeled inclusion as a function time. Laser pulses start activating the LANDs at 0.4 s. Corresponding two sets of the LAND-localized frames are shown using L = 3 and L = 5.

Table 7 – Quantitative assessment of LAND-localization results in a phantom.

Number of laser pulses (L)	Contrast-to-noise ratio				Processing times	
	No. trials	B-scans	PFHnD frames	Mean improvement (%)	No. trials	Mean (95% CI) (ms)
3	13	0.49 (0.48, 0.51)	1.12 (1.09, 1.16)	128.8		104.6 (104.0, 105.2)
5	11	0.50 (0.49, 0.51)	1.45 (1.44, 1.47)	190.4		135.7 (134.8, 136.6)
7	9	0.51 (0.50, 0.51)	1.64 (1.62, 1.66)	223.2	100	174.4 (173.7, 175.0)
9	7	0.51 (0.51, 0.52)	1.77 (1.75, 1.78)	246.1		227.4 (226.6, 228.1)
11	5	0.51 (0.51, 0.52)	1.89 (1.88, 1.90)	267.3		291.6 (291.0, 292.3)

Table 7 summarizes the CNR values of both unprocessed B-scans and LAND frames and the averaged processing times of LAND localization with various *L* (3 to 11). As *L* increased, the CNR improvement increased, but increasing *L* may also cause motion-induced errors. Hence, maintaining as small an *L* as possible is desirable to avoid motion artifacts. The measured average processing times were all under 0.3 s per LAND frame without deliberate computational optimization. Depending on the choice of *L*, the frame rate of LAND-localized images ranged from 3 to 10 Hz, whereas the frame rate of B-scan was not compromised with this method (i.e., consistent at 288 Hz). These results indicate that our approach is practical and robust, and that it enables the real-time detection of LANDs necessary for future translational efforts.

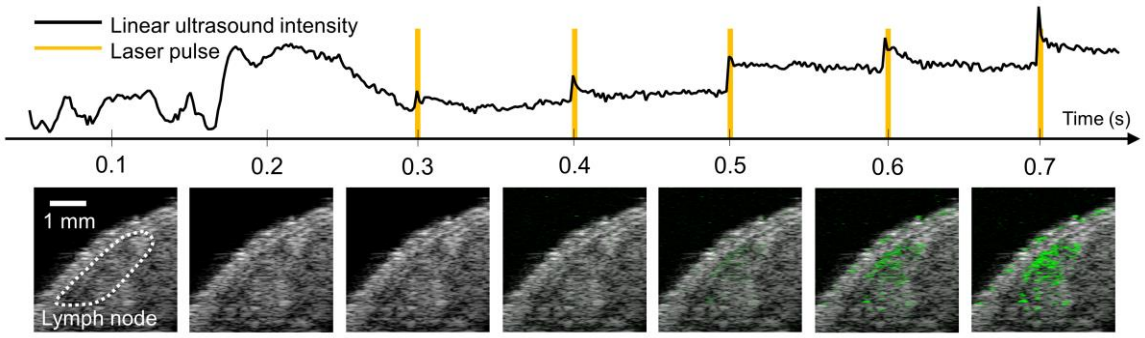

Figure 24 – Ultrasound and LAND-localized images of *in vivo* murine SLN as a function of time. Laser pulses start activating the LANDs at 0.3 s. The LAND-localized frames with *L* = 5 are presented.

In the *in vivo* study, we imaged the murine SLN with the same setup used in the *in vitro* study, and Figure 24 shows the results. Again, a corresponding movie is available online. In Figure 24, we overlaid B-scan ultrasound frames with LAND-localized frames ($L = 5$). A temporal profile on a selected pixel in the lymph node containing LANDs shows their blinking dynamics in response to laser activation. As expected, the more laser pulses used to trigger the LANDs, the better the method can localize the LANDs, which correspond to the location of the SLN. After irradiating the tissue with 5 laser pulses, the

SLN in Figure 24 was identified at 0.7 s with improved contrast over ultrasound alone (i.e., unprocessed B-scans obtained from 0.1 s to 0.4 s in Figure 24).

This study has demonstrated the potential of the developed LAND-localization method via phantom and *in vivo* results. However, the study has several limitations. First, we only showed the *in vivo* results obtained from a single mouse. Our continuing studies will include more animals to validate the method's robustness. In addition, for the clinical translation of this technique, not only should the ability to process the data in real time and provide high contrast be considered, but also the biocompatibility of LANDs should be examined. For example, the Epolight 3072 dye used in this study has not been FDA-approved, but our previous work has shown that the FDA-approved indocyanine green (ICG) dye was successfully loaded in perfluorocarbon nanodroplets, indicating that the LAND platform has high translational potential [133]. Lastly, we have not explicitly investigated the stability of LANDs (i.e., the number of cycles of vaporization and recondensation that LANDs can endure in response to pulsed laser irradiation). In these experiments, LANDs were imaged for at least five minutes, which equals to 3,000 cycles with our 10 Hz laser, suggesting their ability to reliably vaporize and recondense. In addition, our previous work has demonstrated that the vaporization of the LANDs depends on selected laser energy, indicating that the LANDs activated below their vaporization threshold do not vaporize and remain in the liquid state.[133] Thus, to utilize the blinking ability of LANDs, a proper choice of laser energy is required and a laser fluence of 50 mJ/cm^2 in this study allowed the LANDs to vaporize and recondense repeatedly.

4.4 Conclusion

We have introduced a contrast-enhanced imaging method that relies on LANDs undergoing sustained and repeatable phase changes. The LANDs vaporize and recondense in response to pulsed laser irradiation; and given a constant laser PRF, they exhibit periodic

peaks in the temporal ultrasound signal. Based on this unique blinking phenomenon, we have built an imaging method that determines how regularly the temporal ultrasound fluctuates to create a LAND-localized frame. Through our *in vitro* study, we quantified a substantial improvement in CNR over conventional ultrasound achieved with low computational complexity. Furthermore, we successfully identified a murine SLN, illustrating the viability of our technique in a small animal model. These results demonstrate that our approach effectively and efficiently localized LANDs in real time, which is necessary for future work to translate this contrast agent platform to the clinic.

CHAPTER 5. SUPER-RESOLUTION IMAGING WITH ULTRAFAST ULTRASOUND IMAGING OF OPTICALLY TRIGGERED PERFLUOROHEXANE NANODROPLETS

Super-resolution imaging with moving microbubbles has shown potential in identifying fine details of deep-lying vascular compartments. To image the extravascular targets, the current study has employed nanometer-sized, optically triggered perfluorohexane nanodroplets (PFHnDs). In response to pulsed laser irradiation, the PFHnDs repeatedly vaporize and stochastically recondense, resulting in random changes of ultrasound signals. Our previous study has shown that the stochastic recondensation of the PFHnDs can be used to isolate individual PFHnDs for super-resolution imaging. This study introduces an improved method for super-resolution imaging with ultrafast ultrasound imaging of PFHnDs. The previous method was based on subtraction of two consecutive ultrasound images to detect signals from recondensed, isolated droplets whereas our current method compounds respective multiple pre- and post-recondensation ultrafast ultrasound images prior to subtraction to improve the spatial resolution further. To evaluate the axial and lateral resolutions of our method, we repeatedly imaged a phantom containing PFHnDs using a programmable ultrasound system synchronized with

a pulsed laser system. As a result, our method improved the lateral and axial resolutions by 54% and 68%, respectively, over the previous super-resolution imaging approach, indicating that it can be used for localizing extravascular molecular targets with superior accuracy.

5.1 Introduction

Super-resolution ultrasound imaging techniques have shown unprecedented potential in mapping deep-lying microvasculature, which was virtually unattainable because of the fundamental tradeoff between spatial resolution and penetration depth in ultrasound imaging [134-136]. In ultrafast ultrasound localization microscopy (one of the most seminal super-resolution methods), the authors found that ultrafast imaging of gas microbubbles leads to the transient decorrelation of signals, enabling isolation of individual microbubble signals with the clinically relevant concentration of microbubbles [137]. Because the microbubble diameter is much smaller than the ultrasound wavelength, the signal reflected from each microbubble can be viewed as the point spread function (PSF) of the imaging system. Thus, the deconvolution of the individual microbubble signal allows for the detection of exact microbubble positions [138]. These super-resolved locations are accumulated over a few minutes with tens of thousands of images, resulting in the unsurpassed microvasculature map of the *in vivo* rat brain [135].

Since then, more researchers have investigated pre-clinical and technical studies using super-resolution imaging techniques [139-146]. Lin et al. imaged *in vivo* tumor-bearing rats to identify tumor angiogenesis and found that microvascular patterns of healthy and diseased rats are significantly different [139]. Foiret et al. reported that super-

resolution imaging could successfully map the microvasculature of *in vivo* rat kidney in the presence of physiological motion [140]. Moving tissue, however, is a concern in super-resolution imaging because it takes several minutes to collect a stack of images to create super-resolution maps. Thus, Hingot et al. introduced a phase correlation-based motion correction method and assessed the improvement in the quality of super-resolution images [141]. More recently, the nonlocal means (NLM) filter and a graph-based particle tracking method were utilized for robust tracking of microbubbles [142]. Optimization of super-resolution imaging has been investigated in several studies, showing the effect of various sizes and concentrations of microbubbles on the sensitivity of super-resolution imaging [143, 144]. Christensen-Jeffries et al. introduced a method that reduces axial localization errors of microbubbles by comparing various localization methods [145]. In addition, 3-D super-resolution imaging has been investigated using a pair of ultrasound transducers [146].

The microbubble-based super-resolution imaging techniques can map microvasculature with a spatial resolution beyond the wave diffraction limit. However, because of their relatively large size (a few micrometers), microbubbles rarely extravasate from the vasculature, limiting the utility of super-resolution imaging [50]. As an alternative approach, super-resolution imaging with submicrometer-sized, optically triggered droplets was recently introduced [55]. Perfluorohexane nanodroplets were used in these studies because of their ability to vaporize and recondense in response to pulsed laser irradiation. The optically triggered PFHnD is one of many perfluorocarbon nanodroplet species [49, 52, 53, 132, 133], and not only can they be used for super-resolution imaging, but also for contrast-enhanced imaging, by relying on the PFHnD's unique ability to repeatedly

activate [56]. These PFHnDs can be synthesized at sub-micrometer sizes and are thus capable of reaching extravascular targets. The PFHnDs consist of a perfluorohexane core, an optical dye, and a fluorosurfactant shell [133]. In response to pulsed laser irradiation, the PFHnDs can be vaporized and become gaseous microbubbles that can be used for contrast-enhanced ultrasound images. Furthermore, because the boiling point of perfluorohexane (56°C) is higher than physiological body temperature, the PFHnDs can recondense to the native liquid state and can repeatedly undergo phase-transitions [133]. Luke et al. found that the recondensation process of PFHnDs is stochastic and thus at a given time during recondensation, a sparse subset of PFHnDs can be obtained, allowing for isolation and localization of individual PFHnDs [55]. In their method, a stack of images was collected using conventional ultrasound imaging while PFHnDs were recondensing post-laser irradiation. Then, a signal from each PFHnD was isolated by taking a difference between consecutive images to detect randomly recondensed PFHnDs.

In this chapter, we propose a method for improving super-resolution imaging of PFHnDs using ultrafast ultrasound imaging and a temporal compounding approach. Specifically, before taking a difference of ultrasound sequences to detect a stochastic recondensation event, we combine multiple frames before and after droplet recondensation to suppress random background noise thus to improve the accuracy of super-resolution imaging. To demonstrate our approach, a tissue-mimicking phantom containing PFHnDs was used.

5.2 Materials and Methods

5.2.1 Super-Resolution Process with Optically-Triggered Perfluorohexane Nanodroplets

Super-resolution imaging with PFHnDs relies on the random recondensation of PFHnDs. The vaporization and recondensation of PFHnDs are likely to be stochastic because they are a combined function of droplet size, local laser fluence, amount of dye captured, local temperature, local pressure, and local viscoelasticity [55, 79, 147]. To capture their random recondensation, high-frame-rate ultrasound imaging is required because PFHnDs typically recondense within several milliseconds [55, 147].

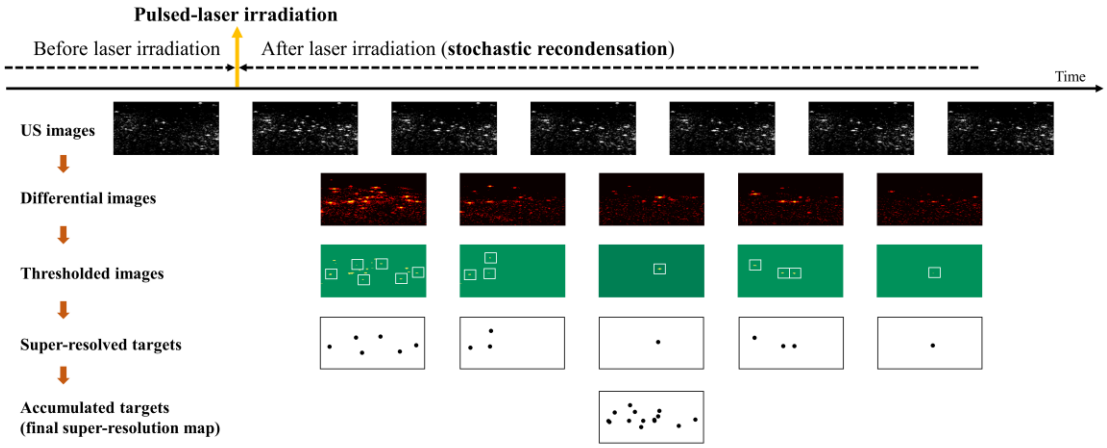

Figure 25 – An overall protocol for super-resolution ultrasound imaging with optically triggered perfluorohexane nanodroplets (PFHnDs). Thresholded images in the third row are binary images (green for zero and yellow for one) and the sparse isolated droplets, which do not have any other droplets located closely, are shown with white squares.

The overall protocol of super-resolution imaging with PFHnDs is illustrated in Figure 25. When the laser pulse irradiates the volume, the PFHnDs are immediately vaporized, producing high contrast ultrasound signals. Then, they begin stochastically condensing back to the original liquid state. As illustrated in Figure 25, the signals from vaporized PFHnDs appear in the second ultrasound image right after laser activation, and then these signals gradually disappear as a function of time because of the random

recondensation of PFHnDs. To detect a sparse subset of randomly recondensing droplets in each frame, differential ultrasound images are taken by subtracting adjacent ultrasound images (note that two terms differentiation and subtraction are used interchangeably in this chapter). In other words, post-laser ultrasound images are subtracted continuously, as shown in the second-row images, to produce a series of differential images. Then, thresholding is applied to reject high-frequency noise amplified by the differentiation process and to detect only the signals from recondensed PFHnDs. The thresholded images are binarized to find the location of droplet signals. From these binary images (images in the third row in Figure 25), the sparse isolated droplets, which do not have any other droplets located closely, are selected as shown with white-colored boxes in Figure 25. Subsequently, these PFHnD patches are fitted to a Gaussian approximation of the PSF of the imaging system, allowing for precise localization of PFHnD positions. Thus, each differential ultrasound image can produce a partial super-resolution map of a sparse subset of PFHnDs recondensed at that time. Finally, all super-resolved targets are combined to create a final super-resolution map. This entire process can be repeated in response to each pulsed-laser irradiation.

5.2.2 Temporal Compounding Approach

To improve the reliability of super-resolution imaging and thus to further enhance the spatial resolution, this study uses ultrafast ultrasound imaging and introduces a temporal compounding approach that respectively averages multiple pre- and post-recondensation images before taking a difference between consecutive ultrasound images. In an example illustrated in Figure 26, all PFHnDs in a particular region of interest vaporize immediately in response to laser illumination, but recondense at different times. Given that

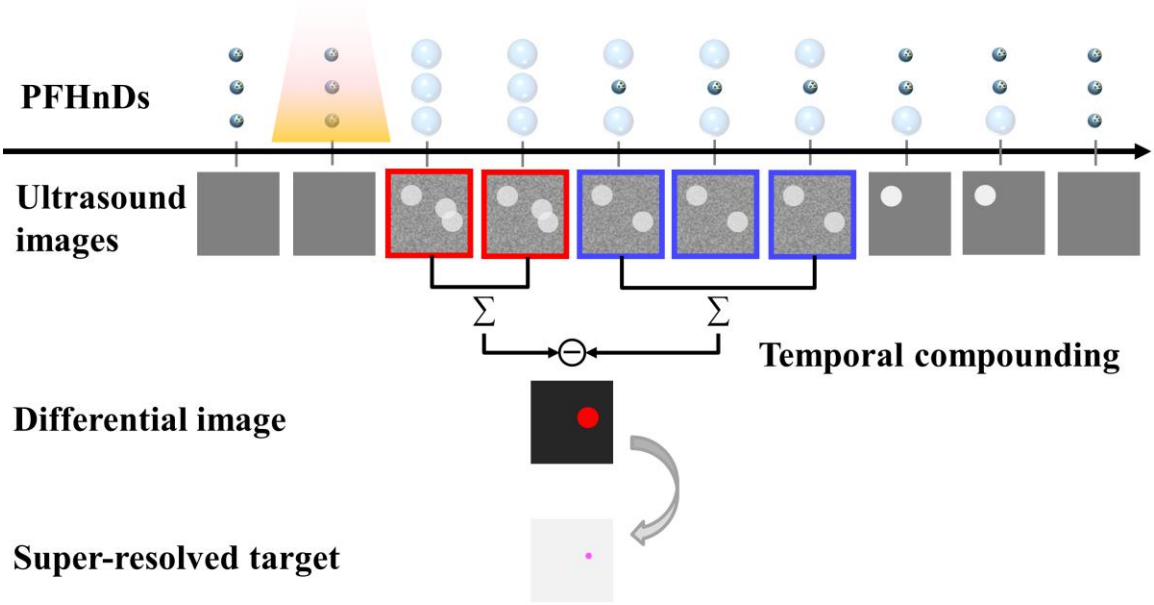

Figure 26 – A diagram describing the temporal compounding approach. Here, the small dark blue circles present nanodroplets before activation and the large light blue circles vaporized microbubbles after activation. Yellow shaded region indicates the nanodroplets under laser illumination.

the frame rate of ultrafast imaging is much higher than that of conventional beam-by-beam ultrasound imaging, in principle, several ultrafast frames can remain the same before recondensation (frames denoted by red outline in Figure 26). Similarly, several ultrafast frames can also remain the same after a specific recondensation event (frames denoted by blue outline). However, ultrasound images contain noise, which is amplified during the frame differentiation process, and therefore, the Gaussian approximation of the PSF of the system may not be reliable [148]. Thus, using temporal information obtained from ultrafast ultrasound imaging, pre- and post-recondensation frames are respectively compounded, and then the corresponding compounded frames with higher signal-to-noise ratio (SNR) are subtracted from each other to create a differential image. Here, the number of ultrafast frames used for compounding is an important parameter that determines the degree of

improvement. The rest of the super-resolution process follows the same protocol described previously [55]. Briefly, the differential images were thresholded to detect recondensed droplets, and Gaussian approximation was used determine the location of the detected droplets.

Similar to the previous approach, our method first detects recondensation events by differentiation and thresholding methods. In general, all detected, isolated droplets could recondense at different, random times and, therefore, would be captured in different frames. From every detected frame for each droplet, pre-recondensation and post-recondensation images are compounded, respectively, according to our choice of the number of compounded frames. Two compounded images (i.e., one containing vaporized PFHnD signals and another containing recondensed background signals) are subtracted to obtain noise-reduced differential images as shown in Figure 26. In some cases, due to the random nature of droplet recondensation, the number of frames compounded pre-and post-recondensation could be different. A droplet recondensing "early" (when the number of desired compounded images is k and the recondensation event occurs prior to the k^{th} frame) would limit the pre-recondensation frame compounding while the "late" recondensing droplet (when the recondensation event occurs within last $k-1$ frames) would limit post-recondensation compounding. For example, if one droplet is deactivated in the third frame, then it would have at most only two pre-recondensation images to be compounded. This would not affect the post-recondensation compounding as the originally selected number of compounded frames (1-10) for analysis in post-recondensation would be used. As a result, a droplet that recondenses midway through acquisition best demonstrates the effect of temporal compounding to improve spatial resolution as it allows for the originally

selected number of compounded frames to be used pre- and post-recondensation. In addition, the number of frames for compounding would be further limited when pre- or post-recondensation patches for each droplet contain recondensation events from other closely located droplets, which are rejected by tracking the number of peaks in the patches. Thus, local peaks in each candidate patch are detected and when more than one occurs, that patch was not used. The size of the patch was determined by the ultrasound wavelength λ. In this study, the dimension of the patch was 3λ x 3λ (i.e., 0.96 mm x 0.96 mm).

5.2.3 Experimental Set-Up

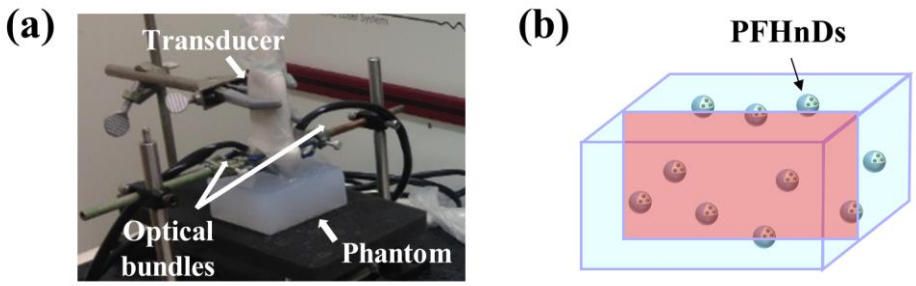

Figure 27 – (a) An experimental set-up consisting of a linear array transducer with bifurcated optical fiber bundles and a fabricated polyacrylamide gel, and (b) a diagram representing the phantom containing PFHnDs. The red rectangle in the cubic phantom indicates an example cross-section as an imaging plane.

To verify the temporal compounding approach, we fabricated a tissue-mimicking phantom containing PFHnDs mixed in a polyacrylamide gel (Figure 27 (a)). It has been demonstrated that a polyacrylamide phantom has tissue-like acoustic properties such as density, sound speed, acoustic impedance, and attenuation; from the parameter published elsewhere [149], the acoustic attenuation coefficient was calculated to be 2.0 dB/cm at 9.6 MHz (a center frequency used in this study). In addition, a polyacrylamide phantom has

desired optical properties as it is transparent in the near-infrared region [150]. Although not performed in our study, the optical absorption and scattering properties of gel can be tuned using additives.

PFHnDs were prepared using 3 mL of deionized water, 0.3 mL of perfluorohexane (FluoroMed, L.P., Round Rock, TX, USA), 1 mL of Zonyl fluorosurfactant (1% v/v, Sigma-Aldrich, St. Louis, MO, USA), and 2 mg of near infrared absorbing dye (Epolight 3072, Epolin, Inc., Newark, NJ, USA) with an optical absorption near 1064 nm wavelength. Droplets were formed by adding materials to a 7 mL scintillation vial, placing the vial in a water bath, and sonicating the mixture using a probe sonicator (Q500, QSonica LLC, Newtown, CT, USA) for 60 seconds at an amplitude of one. The resulting emulsion was washed in a mini-centrifuge (Mini-Spin, Eppendorf, Hamburg, Germany) at 400 rcf for 2 min. The supernatant was kept and the pellet discarded. Droplets were sized at 464 nm ± 129 nm (Zetasizer Nano ZS, Malvern Instruments Ltd., Malvern, UK). From stock, the droplet concentration was ~10^8 nanodroplets/mL.

The volume of the phantom was 170 mL and consisted of 42.5 mL of 40% polyacrylamide solution (Thermo Fisher Scientific, Walthan, MA, USA), 1.7 mL of 10% ammonium persulfate solution (Sigma-Aldrich, St. Louis, MO, USA), 212.5 µL of TEMED (Sigma-Aldrich, St. Louis, MO, USA), and 127 mL of deionized water. The water, polyacrylamide solution, and ammonium persulfate were added to a Büchner flask and mixed using stir plate for about 10 minutes. Using a vacuum chamber, the volume was degassed. After degassing and prior to adding TEMED to solidify the polyacrylamide gel, 17 µL of PFHnDs (1:10,000 dilution, ~10^4 nanodroplets/mL) from the stock were added to the solution.

The approximate concentration of the droplets in the unit volume resulted in 10 nanodroplets/mm^3 (i.e., one nanodroplet per 100 μm^3). Our study requires repeated tracking of individual droplets over multiple blinking events for resolution assessment. However, considering the ultrasound wavelength of 160 μm (9.6 MHz center frequency used in the study), the average spacing between nanodroplets would be not far greater than the resolution, which may not be appropriate in observing individual PFHnDs over the course of repeated vaporization and recondensation events. However, because the density of perfluorohexane (1.68 g/ml) is greater than water, many of them could settle down toward the bottom of the phantom while being solidified. Thus, we have fabricated the phantom with various concentrations and heuristically determined the concentration (i.e., 10^4 nanodroplets/mL) to not only have the reasonable number of PFHnD signals, but to also have the appropriate PFHnDs sparsity for signal localization.

The fabricated phantom was imaged using a multi-wavelength photoacoustic and plane-wave ultrasound imaging system that combines a wavelength-tunable nanosecond pulsed laser (Phocus Mobile, Opotek Inc., Carlsbad, CA, USA) and a programmable ultrasound imaging system (Vantage 256^{TM}, Verasonics Inc., Kirkland, WA, USA) equipped with a linear array transducer (L11-4v, Verasonics Inc., Kirkland, WA, USA) operating at 9.6 MHz center frequency [151]. In this study, a single optical wavelength of 1064 nm was used; this wavelength is near the peak optical absorption of the dye-loaded PFHnD. Using nanosecond laser pulses delivered through the bifurcated optical fiber bundles placed on both sides of the ultrasound imaging transducer (Figure 27 (a)), the area of phantom underneath of the transducer was irradiated. The laser fluence measured from the output of the optical bundles was 47.5 mJ/cm^2, satisfying the ANSI safety limit [114].

Before and after the laser pulses, the irradiated area was imaged using ultrafast ultrasound to capture the temporal dynamics of the PFHnDs (Figure 27 (b)). A pulse-repetition-frequency (PRF) of ultrafast ultrasound imaging was 9 kHz but, due to angular compounding of three plane-wave angles (−2°, 0°, +2°), the effective frame rate of ultrasound imaging was 3 kHz. For each laser pulse, 90 compounded ultrasound frames were collected. The Verasonics system beamformed all raw-format data and stored the resultant IQ data, which were processed off-line for super-resolution imaging. The PRF of laser pulses was 10 Hz thus the pulsed-laser irradiation and the ultrasound data acquisition were repeated every 100 ms.

5.2.4 Lateral and Axial Resolution Assessment

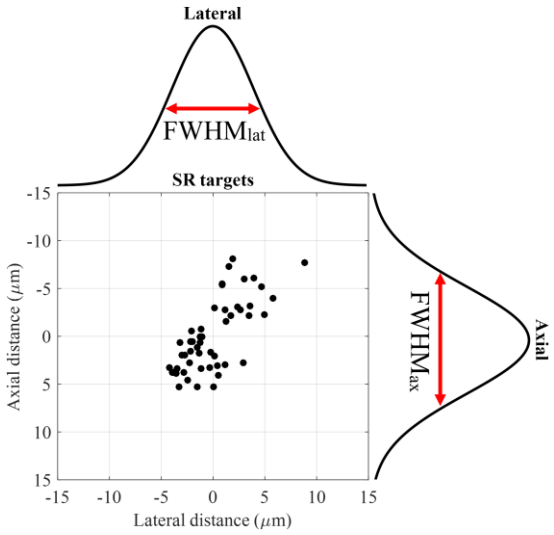

Figure 28 – Assessment of lateral and axial resolutions of super-resolution imaging.

To assess the effect of the temporal compounding in super-resolution imaging, lateral and axial resolutions as a function of the number of compounded frames were quantified using the method described elsewhere [55]. Specifically, we irradiated the

phantom with 50 laser pulses repeatedly and found the isolated droplets that blinked more than or equal to 30 times. Then, the distribution of at least 30 super-resolved positions from each droplet was fit to the Gaussian function both laterally and axially to obtain corresponding full width at half maximum (FWHM) in both directions as shown in Figure 28. The FWHM in lateral and axial directions are referred to as $FWHM_{lat}$ and $FWHM_{ax}$, respectively. For the better statistical analysis, we repeated this process by imaging 7 different cross-sections of the phantom. Using the droplets that blinked more than or equal to 30 times, found in these 7 imaging planes, we evaluated $FWHM_{lat}$ and $FWHM_{ax}$ as a function of the number of temporally compounded frames.

5.3 Results

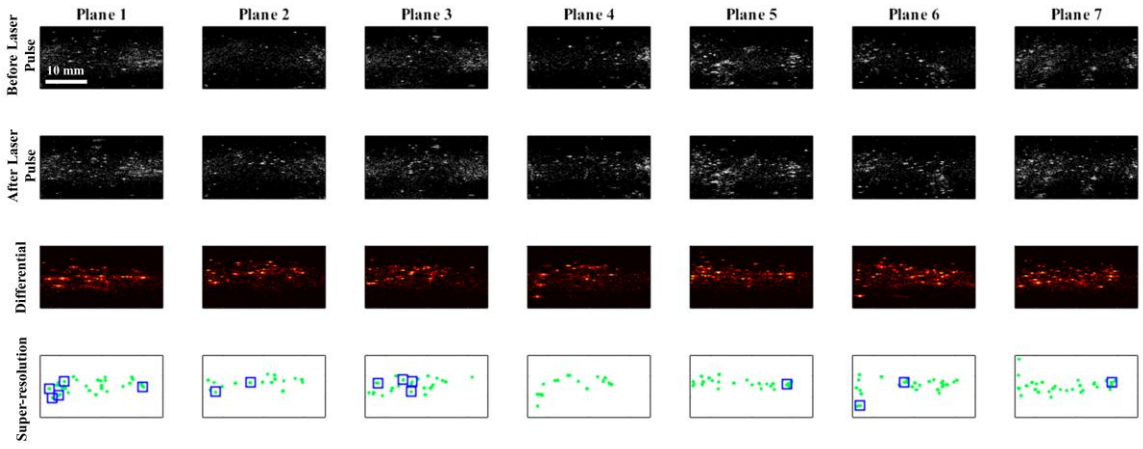

Figure 29 – Super-resolution imaging results with 7 imaging planes selected in the phantom. Columns represent different imaging planes from plane 1 to plane 7. The first and second row images represent pre- and post-laser activation ultrasound images, respectively. To employ the signals solely generated from the vaporized PFHnDs, differential images between pre- and post-laser ultrasound images were taken and presented in the third row. Super-resolution imaging was performed with 50 laser pulses and the resulting super-resolved targets, accumulated over all laser pulses, are shown in the fourth row images.

We imaged 7 cross-sections of the phantom where each cross-section (referred as Plane 1, Plane 2, … , Plane 7 in Figure 29) was exposed to 50 laser pulses accompanied with ultrafast ultrasound imaging. The results presented in Figure 29 show typical greyscale ultrasound images before and after laser pulses that led to optical activation of PFHnDs. In addition, differential ultrasound images for each cross-section are also shown in Figure 29. Finally, the resultant super-resolved targets were accumulated and displayed in the super-resolution maps shown in the last row in Figure 29. Here, 15 locations highlighted by the blue squares contain at least 30 and up to 50 super-resolved positions of the droplet while other super-resolved targets had less than 30 blinking events and were not used in further analysis.

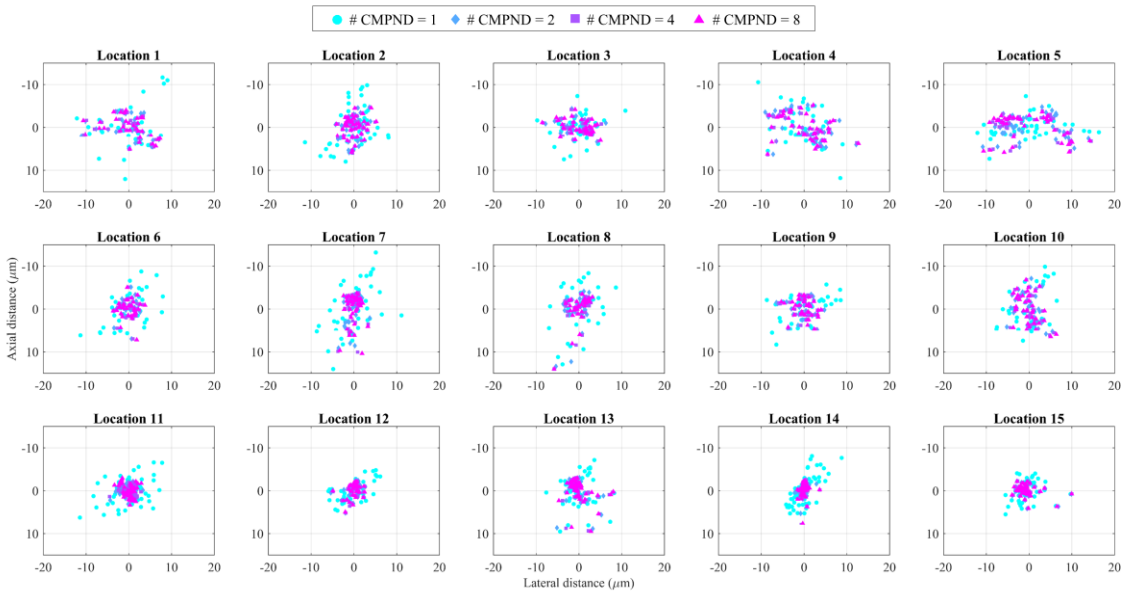

Figure 30 – Super-resolved positions of droplets (15 locations with droplets exhibiting at least 30 blinking events) as a function of the number of compounded frames (1, 2, 4, and 8).

Using 15 locations of super-resolved droplets presented in Figure 29, we evaluated the effect of the temporal compounding approach and the corresponding resolution

Table 8 – Mean recondensation frames.

Location	Recondensation frame (mean ± STD)
1	2.3 ± 0.8
2	2.9 ± 0.9
3	2.3 ± 0.5
4	2.1 ± 0.2
5	5.8 ± 3.9
6	2.8 ± 0.7
7	8.2 ± 4.1
8	5.0 ± 2.3
9	2.3 ± 0.4
10	2.2 ± 0.4
11	12.5 ± 4.6
12	2.6 ± 0.5
13	2.1 ± 0.5
14	9.9 ± 2.0
15	2.2 ± 0.4

enhancement. Specifically, temporal compounding using one frame (i.e., no compounding) to 10 frames was applied, and the variations in the distribution of the super-resolved positions of each target were estimated. The results shown in Figure 30 indicate that the super-resolved positions tend to converge toward the center as the number of compounded frames increases. Indeed, temporal compounding reduces the variations in super-resolved targets and thus improves the reliability and the localization accuracy in super-resolution imaging. Table 8 lists the mean frame numbers and their standard deviations (STD), where the recondensation events occurred for all corresponding 15 droplets. As previously explained, the droplets are recondensed at random, and at different times. Therefore, even if our parameter of the number of compounded frames varies from 1 to 10, the number of pre- and post-recondensation frames to be compounded cannot be necessarily 1 to 10. For,

example, for the droplet termed location 8, the mean recondensation frame was 5, meaning that its pre-recondensation images can be up to 4 frames on average.

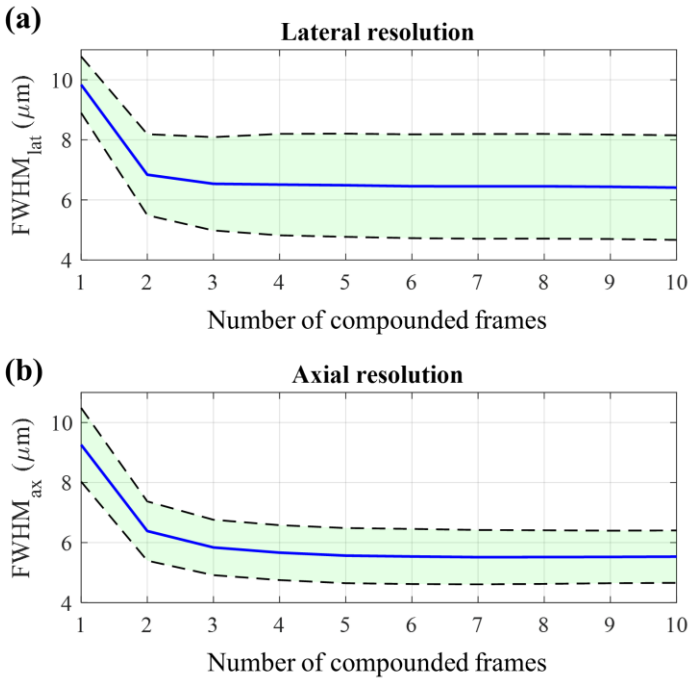

Figure 31 – FWHM$_{lat}$ and FWHM$_{ax}$ assessment results as a function of the number of compounding frames. Blue lines represent the means of FWHM$_{lat}$ and FWHM$_{ax}$ and black dotted lines represent corresponding 95% confidence intervals.

Furthermore, we quantified FWHM$_{lat}$ and FWHM$_{ax}$ of the location of these 15 droplets and evaluated their means and 95% confidence intervals. The results are presented in **Figure 31** where blue lines represent the means of FWHM$_{lat}$ and FWHM$_{ax}$ and black dotted lines represent their 95% confidence intervals. Here, the number of compounded frames equal to one corresponds to the previously introduced approach [55]. As can be seen in **Figure 31**, both FWHM$_{lat}$ and FWHM$_{ax}$ decease as the number of compounded frames used increases. Compared to the previous approach where no compounding was

used, the temporal compounding improves the lateral and axial resolutions by up to 54% and 68%, respectively.

5.4 Discussion

Our study revisited super-resolution ultrasound imaging of optically triggered PFHnDs introduced earlier [55]. Using ultrafast ultrasound imaging and temporal compounding, the localization of the targets was improved. Ultrafast ultrasound imaging captures an order of one to two times more temporal information on the transient, stochastic recondensation of the PFHnDs. Hence, before differentiating adjacent images to identify the recondensation event, the temporal compounding approach, which averages multiple pre- and post-recondensation images, could be applied to further improve the ability to localize the PFHnDs. Using the tissue-mimicking phantom containing PFHnDs, we have shown that our approach improves both lateral and axial resolutions by about a factor of two. Because frame averaging reduces electrical background noise, the Gaussian approximation of the PSF of the imaging system was more reliable, leading to improved spatial resolution.

To understand the theoretical limit of spatial resolution improvements in our approach, we have investigated how the random noise in the ultrasound image affects the Gaussian fitting process through the simulation. In super-resolution fluorescent imaging, it has been proven that the uncertainty of the Gaussian fitting (i.e., the position error of each measurement) is related to the standard deviation (STD) of the imaging system PSF, the number of photons, pixelation noise, and background electrical noise [148]. Because the STD of the PSF and the pixilation noise would be fixed in the given system and the number

of photons is not applicable to ultrasound imaging, here we observed the changes in FWHM of the super-resolution imaging as a function of the background noise and as a function of the number of compounded frames. We modeled signals from pre-recondensation PFHnDs as the PSF of the system and signals from post-recondensation PFHnDs as background. Then, we have added zero mean white Gaussian noise with STDs ranging from 0 to 0.25 with a step size of 0.05 to both pre- and post-recondensation images, resulting in the signal-to-noise ratios (SNRs) ranging from ∞ dB to 11.2 dB. The FWHM was measured as a function of the number of compounded frames on the subtracted images after temporal compounding. Figure 32 shows an exemplary comparison between 1 and 10 compounded frames with the noise STD of 0.1. When the compounded frames were 10, the subtracted PFHnD signal was less noisy, leading to far reduced localization errors.

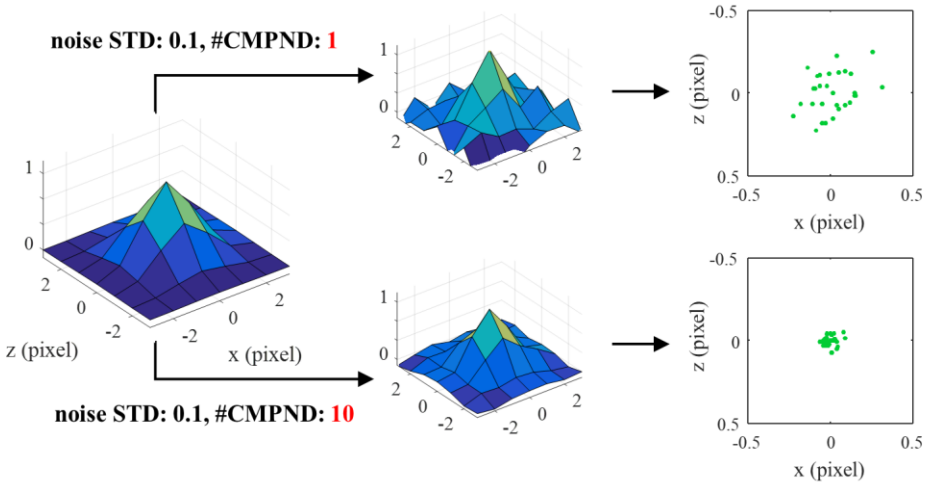

Figure 32 – Simulation steps to evaluate the proposed approach with various electrical noise and the number of compounded frames. Here, the modeled PSF is added with noise with a STD of 0.1 to create noise-corrupted images. 1 and 10 compounded frames are compared to present how they affect the distribution of localization positions.

The results of the simulation are shown in Figure 33. Overall, as the number of compounded frames increases, FWHM decreases (i.e., spatial resolution improves) because the electrical background noise added reduces as the number of compounded frames increases. If SNR is ∞ dB (i.e., the noise STD is 0 or there was no noise), no localization error occurred, resulting in the FWHM of 0. However, as the SNR decreases, the FWHM becomes large up to about one pixel. As the number of compounded frames reaches 10, the improvement in the FWHM was almost five fold for the SNR of 11.2 dB. Overall results show that depending on the SNR of ultrasound images, the temporal compounding leads to gradual resolution improvement.

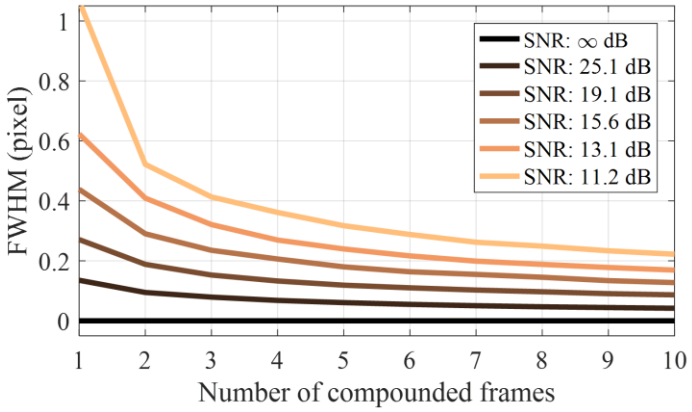

Figure 33 – The estimated FWHM in terms of pixel as a function of the number of compounded frames with various SNRs.

In theory, the noise reduction by averaging signals is proportional to the square root of the number of the compounded frames. Thus, if we have the very large number of compounded frames, the effect of the noise should be negligible. However, our approach relies on the subtraction process between pre- and post-recondensation images, which amplifies the noise influence after averaging, limiting the decrease in FWHM.

Furthermore, as presented in Table 8, many droplets recondensed at relatively earlier frames (2 to 3). Therefore, our experimental results in **Figure 31** show more limited improvements in resolution, compared to the simulation results in Figure 33. The droplet locations for 7, 11, and 14 had relatively larger mean recondensed frames, and thus, they resulted in the narrower distributions with respect to the number of compounded frames in Figure 30 compared to other droplets. As a result, the fundamental limit of the resolution improvement is dependent on noise of the system and the random recondensation timing of each droplet.

Although the frame compounding approach is simple and effective in resolution enhancement, combining multiple frames can cause physiological motion artifacts, which are critical in super-resolution [141]. However, even if 10 images (i.e., ideally 20 images for both pre- and post-recondensation images) are used for temporal compounding, it only requires imaging target to be stationary for 6.6 ms (the frame rate of 3 kHz in this study was used to compute the imaging time, i.e., 0.33 ms x 20 images). Fortunately, as can be seen in **Figure 31**, the enhancements in both lateral and axial resolutions is most noticeable for small number of frames. In other words, our approach only needs up to five frames to reach its almost full potential, which takes less than 3.3 ms (0.33 ms x 5 x 2 images). Furthermore, although we used the PRF of 9 kHz with three angles of plane waves, the PRF could be higher if the imaging depth permits (theoretically, for imaging of a 20-mm depth, the PRF can reach up to 38.5 kHz), which can further alleviate potential concerns in motion artifacts.

This study has not investigated the effect of the frame rate in super-resolution imaging. However, not only could the frame rate affect motion artifacts, but also it can

determine the overall imaging time or the number of isolatable nanodroplets per laser pulse. As discussed, the recondensation of the PFHnDs is a stochastic process. Therefore, if two closely-spaced droplets are recondensed at a slightly different time, then slower frame-rate imaging will identify them as recondensed at the same time thus not allowing for localization of each droplet. However, imaging with a faster frame rate should resolve them as two separable droplets. Thus, as the frame rate increases, an increased number of isolated droplets could be detected. Consequently, a higher concentration of PFHnDs can be used with higher frame rate imaging, which also will reduce the overall imaging time. Our future study will include the investigation of the effect of the frame rate in super-resolution imaging.

The laser-activated PFHnDs recondense randomly and thus at different times, which is the crucial finding that enables the super-resolution with nanodroplets. However, in our experiments, many droplets were recondensed in the first few ultrasound frames thus limiting the applicability of the temporal compounding approach. Thus, a method to make the recondensation of the droplets more stochastic and less transient should be studied in the future. If the stochastic behavior of the droplets could be manipulated, more super-resolved targets could be imaged while the imaging session is shortened. For example, because the boiling point of a gas core affects recondensation dynamics, instead of pure perfluorohexane (boiling point: 56°C), a mixture of perfluorohexane and perfluoropentane (boiling point: 29°C) could be used to extend the recondensation time [147]. In addition, to make droplet recondensation more random, a polydisperse distribution of droplets can be used because the size of droplets also affects the recondensation time.

The penetration depth of light is typically more limited than that of an acoustic wave. Therefore, to reach full potential of the optically triggered PFHnD-based super-resolution imaging, a thorough investigation of the activated depth of the PFHnDs is necessary. Our previous work using perfluoropentane nanodroplets has shown that these droplets can be vaporized at further than a 3-cm depth in turbid media [53]. The PFHnDs may have a slightly shallower imaging depth because they could require higher optical fluence to be activated due to the higher boiling point. Therefore, clinical applications using the PFHnDs could be restricted. However, it has been shown that negative pressure of externally applied acoustic field could be used together with laser pulses to increase the activation efficiency of droplets [152].

Unlike super-resolution imaging based on micrometer-sized contrast agents, we have used submicrometer-sized nanodroplets capable of extravasating from the vascular compartment, which may expand the utility of super-resolution imaging. Currently available imaging methods struggle to characterize *in vivo* tumors at the molecular and cellular level. Understanding the molecular composition of a tumor is crucial in treatment planning and outcome because tumor cells are genetically heterogeneous [4, 5]. Super-resolution imaging with molecularly targeted PFHnDs could be a solution in identifying the tumor microenvironment, enabling the effective personalized treatment.

5.5 Conclusion

We have introduced a method for improving super-resolution imaging with ultrafast ultrasound imaging of optically triggered PFHnDs. The frame compounding approach was suggested and verified with the phantom containing PFHnDs. Quantitative

assessment of the method has shown that lateral and axial resolutions can be reduced by 54% and 68%, respectively, over the previous approach, indicating that it can be used for localizing extravascular molecular targets with improved accuracy.

CHAPTER 6. COMBINED MULTI-WAVELENGTH PHOTOACOUSTIC AND PLANE-WAVE ULTRASOUND IMAGING FOR PROBING DYNAMIC PHASE-CHANGE CONTRAST AGENTS

The purpose of this study was to introduce combined multi-wavelength photoacoustic (PA) and plane-wave ultrasound (US) imaging referred to as mwPA/pwUS imaging capable of probing the rapid dynamic behavior of optically activated phase-change contrast agents. A dedicated mwPA/pwUS imaging sequence was developed based on a programmable US system synchronized with a tunable laser to irradiate tissue with laser pulses at desired optical wavelengths and to acquire post-laser-pulse PA images followed by ultrafast plane-wave US images. To evaluate the mwPA/pwUS imaging, a capillary filled with optically responsive perfluorohexane nanodroplets (PFHnDs) containing a dye with the peak absorption at 760 nm was imaged with optical wavelengths ranging from 700 nm to 940 nm. The differences between post-laser ultrafast US images (i.e., differential US (ΔUS)) were taken to visualize the recondensation dynamics of PFHnDs at each wavelength. The PA images of PFHnDs showed higher contrast near 760 nm, corresponding to the peak absorption of the dye encapsulated in the PFHnDs. Moreover, the ΔUS signals immediately after 760 nm pulsed-laser irradiation were also high due to

the increased US contrast associated with vaporized PFHnDs. The mwPA/pwUS imaging allowed for the US-based optical spectroscopic characterization of PFHnDs and their dynamics. The introduced mwPA/pwUS imaging sequence can be used in various clinical applications where both spectroscopic PA imaging of endogenous and/or exogenous chromophores and ultrafast US imaging of phase-change nanodroplets are desired.

6.1 Introduction

Phase-change ultrasound contrast agents such as perfluorocarbon nanodroplets have demonstrated promising potential in various diagnostic ultrasound and therapeutic applications [48, 51]. Unlike traditional microbubbles (usually 1−5 μm diameter), phase-change contrast agents can be synthesized at sub-micrometer sizes, which allows them to extravasate from the intra-vascular space [47, 154]. In addition, because of their relative stability, these phase-change contrast agents can circulate longer than microbubbles [45]. Once administered, they can be vaporized by an acoustic trigger to undergo a liquid-to-gas phase transition, providing on-demand high contrast ultrasound [131, 155].

Optically triggered nanodroplets (nDs) are a new class of phase-change contrast agents [49]. These nanodroplets contain optical absorbers (e.g., dyes or nanoparticles) that can be used to vaporize perfluorocarbon nDs in response to pulsed-laser irradiation [49, 52, 129, 130]. Perfluorohexane nanodroplets (PFHnDs) with the boiling point (56°C), higher than the physiological body temperature (37°C), recondense after vaporization. Importantly, this vaporization-condensation process is repeatable, which offers repeated high-contrast photoacoustic (PA) and ultrasound (US) signals. Here, PA signals are generated from both the vaporization of PFHnDs and the thermal expansion of dye within

PFHnDs. US signals are increased due to an acoustic backscattering from the transient microbubbles formed right after vaporization of PFHnDs.

The recondensation of PFHnDs is a function of many factors including core type, droplet size, photoabsorber type, local optical fluence, local temperature, local acoustic pressure, and local viscoelasticity [55, 79, 147]. The droplet recondensation is, therefore, transient and stochastic in general. Previously, the gas-to-liquid transition of PFHnDs captured via ultrasound imaging was demonstrated in several applications including super-resolution imaging of the vasculature and contrast-enhanced imaging of the mouse lymph node [55, 56, 133]. However, it has been experimentally shown that the recondensation of the PFHnDs typically takes just a few milliseconds although it could vary from a few microseconds to tens of milliseconds [55, 147]. Therefore, high-frame-rate ultrasound imaging is required to capture the gaseous state of vaporized PFHnDs prior to recondensation.

Previously, PFHnDs were imaged using a preclinical US and PA imaging system (Vevo 2100, FUJIFILM VisualSonics, Inc., Toronto, ON, Canada), where laser illumination was not synchronized with US imaging; this was done to achieve high-frame-rate US imaging during laser activation of the PFHnDs [55, 56, 133]. Consequently, no corresponding PA images were obtained due to technical limitations of the US/PA system, operating at 20 Hz or slower. Thus, high frame rate US imaging synchronized with PA imaging is desired to fully exploit the benefits of optically triggered contrast agents such as PFHnDs.

Introducing a tunable laser to trigger nDs containing photoabsorbers with distinct optical absorption peaks allows for selective activation of nDs, enabling multiplexed imaging of molecularly targeted nDs. A previous study has shown that a subset of perfluoropentane nanodroplets (PFPnDs) can be selectively activated at the wavelength corresponding to the particular optical dye inside the PFPnDs, whereas the other PFPnDs containing the dye with different peak absorption were not activated [156]. Due to the low boiling point of perfluoropentane (29°C), the PFPnDs vaporize but do not recondense. Therefore, low-frame-rate US and spectroscopic PA (sPA) imaging were used. However, to extend this method to image PFHnDs, high-frame-rate US with sPA imaging is needed. In addition, sPA imaging not only enables the selective activation and imaging of nDs, but also allows for the quantification of chromophores' concentrations.

The goal of this study was to design, implement, and test an imaging sequence capable of acquiring spectroscopic PA (sPA) images followed by ultrafast ultrasound images. This imaging sequence, referred to as multi-wavelength PA and plane-wave US (mwPA/pwUS) imaging, can capture the dynamic behavior of PFHnDs and can be used in various applications including super-resolution imaging, contrast-enhanced imaging, and molecular multiplex imaging.

6.2 Multi-Wavelength PA and Plane-Wave US imaging

6.2.1 System Configuration

To implement mwPA/pwUS imaging, a programmable ultrasound system (Vantage 256^{TM}, Verasonics Inc., Kirkland, WA, USA) and a tunable pulsed laser (Phocus Mobile, Opotek Inc., Carlsbad, CA, USA) were interfaced and synchronized with a host controller

(Figure 34). Bifurcated optical fiber bundles placed at two sides of a linear array transducer were connected to the laser system to irradiate the imaging volume with laser pulses at 1,064 nm (Nd:YAG primary wavelength) or 690 nm – 950 nm (Nd:YAG laser pumped OPO system). To tune the laser wavelength, the laser was controlled by the host controller using dedicated dynamic-link libraries. Using the MATLAB (MathWorks, Natick, MA, USA), customized imaging routines were developed to sweep the optical wavelength and to acquire post-laser-pulse PA and ultrafast US images.

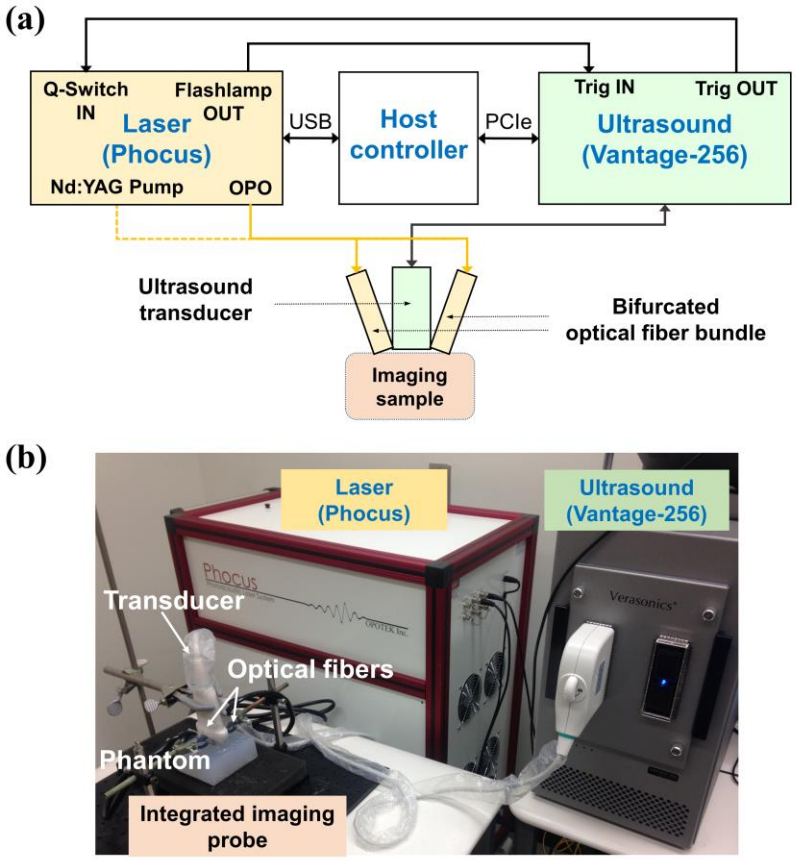

Figure 34 – (a) Block diagram and (b) photograph of the mwPA/pwUS system containing an ultrasound imager, a laser system, a host controller, and an integrated imaging probe consisting of an ultrasound transducer and optical fiber bundles.

6.2.2 Imaging Sequence

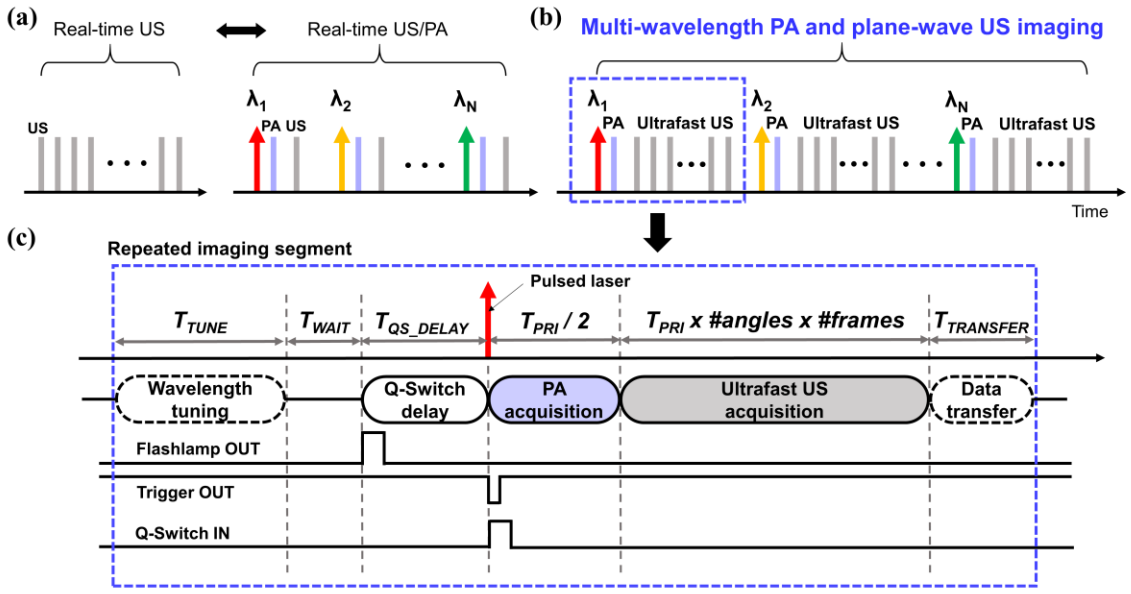

Figure 35 – (a) Real-time US and real-time US/PA imaging mode. (b) mwPA/pwUS imaging mode, where gray lines present ultrafast ultrasound frames acquired as a function of time, and red, yellow, and green lines present multi-wavelength laser pulses. Light blue lines indicate photoacoustic frames. (c) A detailed view of an imaging segment of the overall mwPA/pwUS imaging.

The overall imaging sequence consisted of real-time US/PA imaging as a default mode (Figure 35 (a)) and mwPA/pwUS imaging as an acquisition mode (Figure 35 (b)). The default real-time imaging was used to identify imaging targets before switching to the acquisition mode. In the mwPA/pwUS imaging, laser pulses with pre-selected wavelengths (i.e., λ_1, λ_2, … , λ_N) were used for two purposes: to activate PFHnDs, and/or to obtain sPA images. After irradiating the tissue with a laser pulse at a desired wavelength and obtaining a corresponding PA image, ultrafast US imaging captured the temporal dynamics of PFHnDs.

The imaging sequence started with irradiation of a laser pulse tuned to a particular wavelength, followed by PA and US imaging. Each segment of an imaging sequence, outlined using a blue dotted rectangular box (Figure 35 (b) and (c)), consisted of several

modules including wavelength tuning, Q-Switch delay, PA image acquisition, ultrafast US image acquisition, and data transfer (Figure 35 (c)). For T_{TUNE}, the laser system was tuned to produce a desired optical wavelength. Then, the ultrasound system waited for T_{WAIT} for a "flashlamp OUT" trigger signal from the laser system. The flashlamp signal is generally periodic, and in the case of our laser system, it was repeated every 0.1 sec (10 Hz). Once triggered, the ultrasound system sent out a "trigger OUT" signal after a pre-determined Q-Switch delay (T_{QS_DELAY}) to irradiate a laser light. After the "Q-Switch IN" signal from the Verasonics system activated laser pulse generation, PA acquisition began immediately and continued for half of a pre-defined US pulse-repetition interval (PRI) (i.e., $T_{PRI}/2$). Thus, the Verasonics system controlled the Q-Switch delay signal, determining the laser fluence. Then, ultrafast US images were acquired based on the user-defined number of plane-wave angles and frames. Each imaging segment per laser pulse concluded with transfer of captured data ($T_{TRANSFER}$).

For mwPA/pwUS imaging, the single-wavelength PA and ultrafast imaging was repeated for each optical wavelength, i.e., until the last optical wavelength (λ_N) was reached (Figure 35 (b)).

6.2.3 PFHnD Synthesis and Phantom Experiments

The PFHnDs were synthesized by sonication-based methods, described in detail elsewhere [133]. The resulting PFHnDs consisted of a fluorosurfactant (Zonyl FSO, Sigma-Aldrich, St. Louis, MO, USA) shell with a liquid perfluorohexane (FluoroMed, L.P., Round Rock, TX, USA) and an optical dye (Epolight 9151, Epolin Inc., Newark, NJ, USA). The optical absorption peak of the dye was around 760 nm.

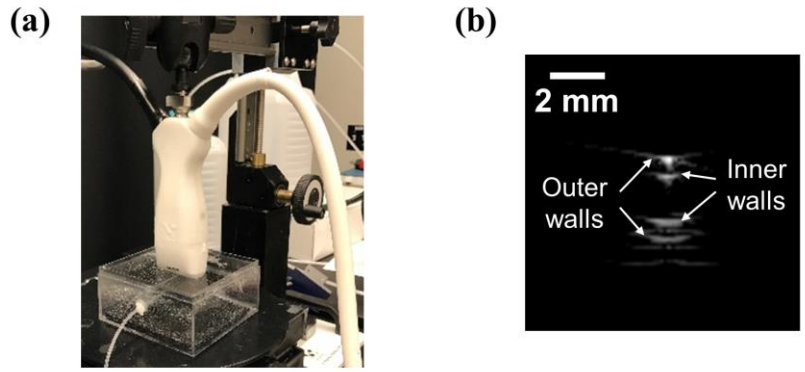

Figure 36 – (a) Experimental setup for imaging PFHnDs and (b) an example B-scan ultrasound image of the cross-section of the tube.

To test the developed system, a phantom containing a small capillary (inner and outer diameters are 1.6 mm and 2.9 mm, respectively), filled with PFHnDs and positioned horizontally in a plastic cuvette, was prepared (Figure 36 (a)). The integrated imaging probe was positioned above the tube phantom, and the phantom was imaged such that the capillary tube was orthogonal to the imaging plane (Figure 36 (b)).

A linear array transducer (LZ201, FUJIFILM VisualSonics Inc., Toronto, ON, Canada) integrated with optical fibers was used. This transducer was connected to the ultrasound system via an adapter (UTA 360, Verasonics Inc., Kirkland, WA, USA). A single angle (0°) of a plane wave with a center frequency of 15.6 MHz (i.e., the wavelength was 98.6 μm) at a pulse repetition frequency (PRF) of 3 kHz was used for ultrafast US imaging. For an imaging depth of 20 mm, the PRF can be up to 38.5 kHz. However, to avoid reverberation artifacts, a PRF of 3 kHz was used in our study. Because angular compounding was not used, the effective frame rate was the same as the PRF. An optical wavelength range from 700 nm to 940 nm with a 30-nm step was used. At each wavelength, a single PA image and 30 US images were collected and displayed using a logarithmic

scale with a dynamic range of 40 dB. To allow for better visualization of the recondensation of PFHnDs, the static signals were rejected by taking a difference between adjacent US frames.

6.3 Results and Discussion

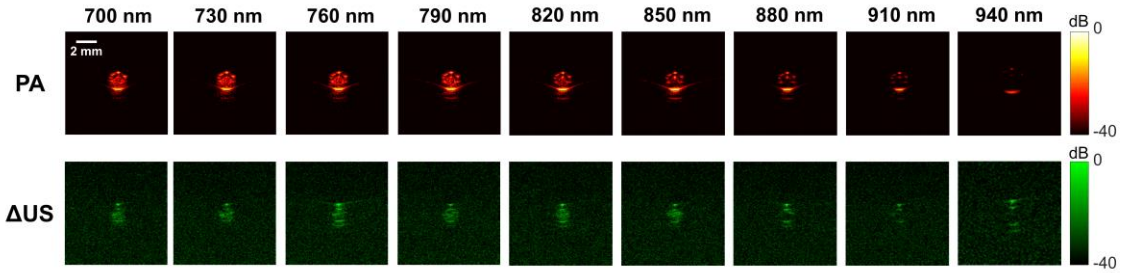

Figure 37 – Photoacoustic and differential US (ΔUS) images of a capillary tube containing PFHnDs. The images were obtained at different optical wavelengths ranging from 700 nm to 940 nm. Each ΔUS image was generated by taking a difference between first two post-laser ultrasound frames.

PA and differential US (ΔUS) images obtained from the tube containing PFHnDs are shown in Figure 37. Because PFHnDs had the dye with a peak optical absorption at 760 nm, the PA signals are stronger near 760 nm than those at other wavelengths. Starting from 790 nm, the magnitude of PA signals decreases as wavelength increases. The corresponding ΔUS images obtained from the first and second US images are presented as a function of wavelength (Figure 37). Given that the ΔUS images represent differences between consecutive images right after the laser activation of PFHnDs, the higher signals in ΔUS images indicate that PFHnDs were successfully vaporized and recondensed. Similar to the PA images, ΔUS signals were high at around 760 nm. The ΔUS signals at optical wavelengths of 880 nm, 910 nm, and 940 nm were very weak, indicating that at

these wavelengths the PFHnDs were not vaporized and recondensed, thus producing no change in ΔUS images.

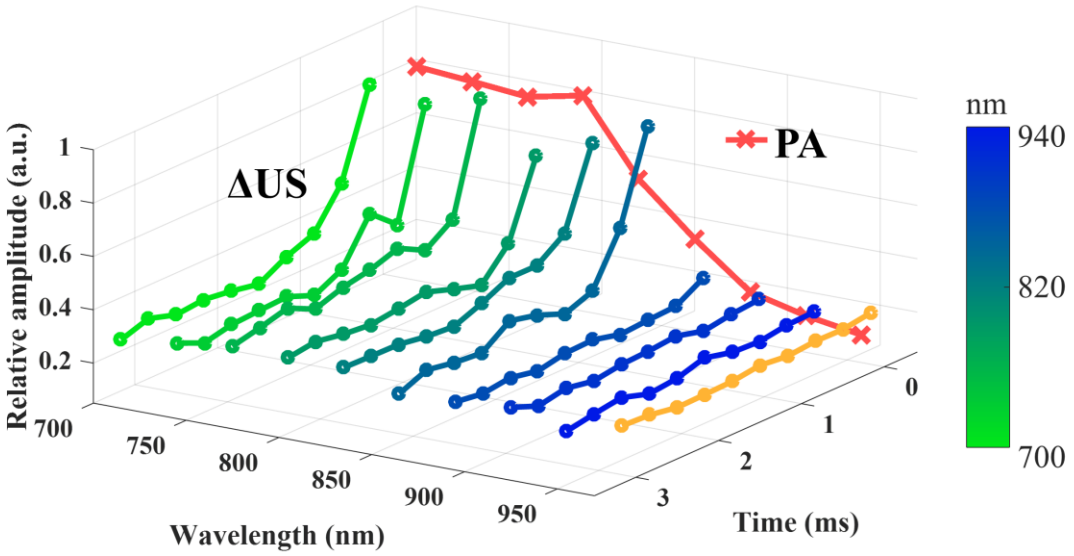

Figure 38 – Mean intensity of PA and ΔUS images inside the tube as a function of optical wavelength and time after each laser pulse. Orange ΔUS line was obtained with US images under no laser irradiation.

Mean intensity of PA (red lines) and ΔUS (green to blue lines) signals inside the tube as a function of both optical wavelength and time is plotted in Figure 38. Both PA and ΔUS signals are clearly wavelength dependent. Although the peak absorption of the dye was at 760 nm, the PA signals were strong within a range from 700 nm to 820 nm due to spectral shift and/or broadening of the absorption of the dye encapsulated in the droplet shell. The PA signals started to decay as wavelength increases beyond 850 nm. The ΔUS signals at higher wavelengths (> 880 nm) do not change significantly over time, which indicates that if the laser wavelength is far from the peak absorption, no vaporization of PFHnDs occurs, and, therefore, ΔUS signals remain low and almost the same as the ΔUS

signals under no laser irradiation (orange line in Figure 38). However, for the ΔUS signals at lower wavelengths (< 850 nm), the large amplitude of ΔUS right after laser pulses demonstrates the occurrence of the PFHnD vaporization. As the PFHnDs recondensed over time, the ΔUS signals accordingly reduced.

In the current study, we observed the vaporization and the recondensation of the PFHnDs repeatedly at the same location. In our previous study, we have shown that the PFHnDs, can repeatedly vaporize and recondense for more than a few thousand times [56]. In the future studies, we will employ the developed imaging sequence to characterize the dynamics of PFHnDs quantitatively.

We have demonstrated the feasibility of mwPA/pwUS imaging using PFHnDs. Although an exogenous agent was used in our study, use of mwPA/pwUS imaging is not limited to contrast-enhanced ultrasound imaging and could be used in various clinical applications. For example, our mwPA/pwUS imaging should be able to simultaneously assess the oxygen saturation level for tumor characterization based on the sPA imaging mode and visualize the dynamics of PFHnDs for tumor detection based on the ultrafast imaging mode [56, 157]. Thus, our approach can be potentially used for both detection and characterization of cancer.

6.4 Conclusion

We have introduced combined mwPA/pwUS imaging as a tool to probe dynamic phase-change contrast agents. The ability of mwPA/pwUS imaging was demonstrated in the phantom study where a capillary tube containing PFHnDs was visualized and analyzed. We have shown that both acoustic and optical features of the PFHnD dynamic behavior

were captured as a function of time and optical wavelength. A poteintial future study will include testing and optimization of the developed imaging method in *in vivo* studies.

CHAPTER 7. DESIGN AND DEMONSTRATION OF A CONFIGURABLE IMAGING PLATFORM FOR COMBINED LASER, ULTRASOUND, AND ELASTICITY IMAGING

This chapter introduces a configurable combined laser, ultrasound, and elasticity (CLUE) imaging platform. The CLUE platform enables imaging sequences capable of uniquely providing quantitative acoustic, optical, and mechanical contrast for comprehensive diagnosis and monitoring of complex diseases, such as cancer. The CLUE imaging platform was developed on a Verasonics ultrasound scanner integrated with a pulsed laser, and it was designed to be scalable and modular to allow researchers to create their own specific imaging sequences efficiently. The CLUE imaging platform and sequence were demonstrated in a tissue-mimicking phantom containing a stiff inclusion labeled with optically-activated nanodroplets and in an *ex vivo* mouse spleen. We have shown that CLUE imaging can simultaneously capture multi-functional imaging signals providing quantitative information on tissue.

7.1 Introduction

In the previous chapter, we have introduced combined multi-wavelength photoacoustic and plane-wave ultrasound (mwPA/pwUS) imaging that can trigger laser pulses with multiple optical wavelengths to support sPA imaging and activate the PFHnD; it allows for observation of transient PFHnD dynamics activated at various optical wavelengths by ultrafast US imaging [158]. The mwPA/pwUS imaging has shown its promising ability to capture acoustic and optical contrast of PFHnDs as a function of both

time and optical wavelength, but it cannot measure the mechanical properties of tissue. To address this issue, there were a few attempts combining ultrasound, photoacoustic, and elasticity imaging. Emelianov *et al.* combined strain imaging-based elasticity imaging and single-wavelength photoacoustic imaging [159]. However, strain imaging could not offer quantitative mechanical properties and single-wavelength PA imaging does not quantify the concentration of chromophores. More recently, Nguyen *et al.* replaced strain imaging by quantitative SWEI and added thermal strain imaging, quantifying lipid-based tissue composition [160]. However, their PA imaging remains qualitative, and their system does not support mwPA/pwUS imaging.

This chapter introduces a configurable, module-based imaging platform, referred to as the combined laser, ultrasound, and elasticity (CLUE) imaging platform. The CLUE imaging platform is capable of supporting various imaging sequences for general researchers in this field to explore a wide array of clinical applications. In the design of the imaging platform, we define each imaging function as a "module," and we allow users to allocate these imaging modules arbitrarily to design their own custom imaging sequences according to their specific needs. Currently, we introduce 14 imaging modules including pulsed-laser excitation, ultrafast US acquisition, and ARF application. These imaging modules can be freely placed as a series of imaging functions when designing an imaging sequence. We have developed the CLUE imaging platform using a specific ultrasound research scanner and laser system, but our design philosophy can be adapted to other hardware. Our CLUE imaging platform and relevant graphical user interface (GUI) scripts are shared in a script repository in the Verasonics Community (http://verasonicscommunity.com). Furthermore, this chapter introduces a combined

imaging sequence referred to as a CLUE imaging sequence that acquires all ultrasound-based quantitative mechanical and functional information on tissue using SWEI and PA and ultrafast US imaging with laser-activated PFHnDs. Because the CLUE imaging sequence can assess multiple quantitative aspects of tissue simultaneously, it potentially can be used to comprehensively characterize the prognosis and treatment response of diseases, such as cancer.

In this chapter, we first introduce a system configuration consisting of an ultrasound system and a laser, and then we explain design details of the developed CLUE imaging platform. Next, we present a representative CLUE imaging sequence, designed on the CLUE imaging platform. To demonstrate this imaging sequence on the CLUE imaging platform, experimental methods for phantom and *ex vivo* mouse spleen imaging studies are described. Subsequent imaging results and discussion follow.

7.2 Design of Configurable Imaging Platform

7.2.1 A Set-Up for Laser and Ultrasound Systems

Our configurable CLUE imaging platform was developed on a programmable ultrasound research scanner (Vantage 256^{TM}; Verasonics, Inc., Kirkland, WA, USA) integrated with a tunable pulsed laser (Phocus Mobile; Opotek Inc., Carlsbad, CA, USA) as illustrated in Figure 39. Note that although the Phocus Mobile laser was used, other laser systems are not excluded, as typical laser systems have a similar communication protocol. In addition, the CLUE imaging platform was designed on the Verasonics scanner, but the same design approach could be applied to other ultrasound imaging systems.

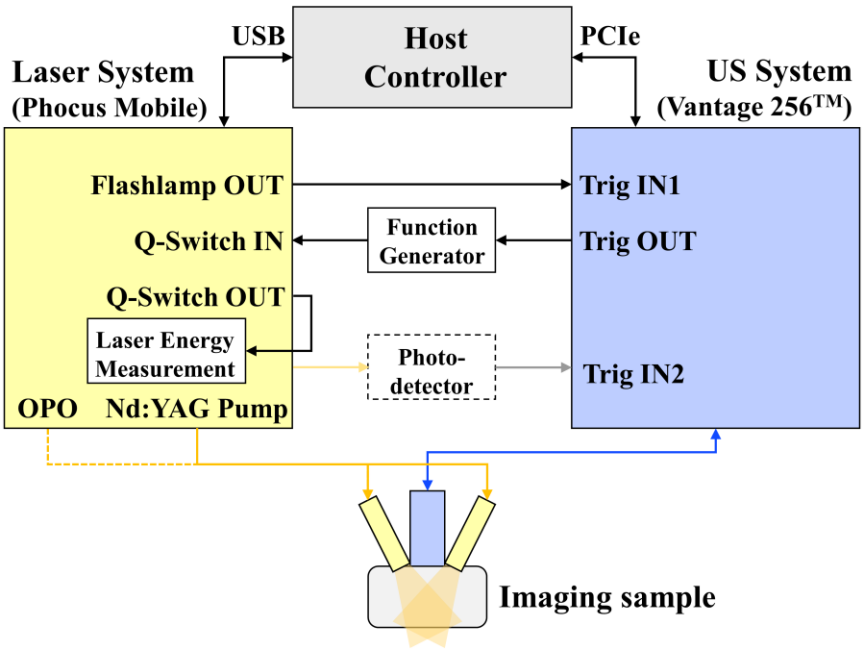

Figure 39 – Block diagram of an overall imaging set-up with integrated ultrasound and laser systems.

In our setup, the laser and the Verasonics system communicate in the following order: (1) A periodic Flashlamp OUT signal from the laser triggers the Verasonics system through Trig IN1, and (2) when triggered, the Verasonics system sends a Trig OUT signal to the laser through a function generator to fire an actual laser pulse after a pre-determined Q-Switch delay. Here, a Q-Switch delay is a delay time between the Flashlamp OUT signal and the Q-Switch IN signal, and it determines the energy of a laser pulse. In general, a longer Q-Switch delay makes the output energy of the laser weaker. When delivering the Trig OUT signal from the Verasonics system to the Q-Switch IN of the laser, the function generator is used to invert the phase and to extend the duration of the Trig OUT signal in order to satisfy the input requirements of the Phocus laser. The same approach can also be found from our previous study [158]. Additionally, a laser energy meter (Pulsar-2; Ophir Optronics Solutions, Inc., Jerusalem, Israel) placed inside the laser was used to measure

and collect the energy of irradiated laser pulses. Lastly, in the case that the time delay between the Trig OUT signal and the actual laser pulse is not negligible, which may delay the generation of PA signals, a photo-detector can be incorporated to synchronize PA imaging. The photo-detector can output a trigger once it senses pulsed-laser irradiation. The trigger can also potentially be used with the second trigger input (Trig IN2) of the Verasonics system.

7.2.2 Module-based Configurable Imaging Platform

The overall process of imaging sequence design and execution using our imaging platform, referred to as the "CLUE imaging platform," is illustrated in Figure 40. The 14 imaging modules listed in Table 9 are shown on top of Figure 40. The crux of the CLUE imaging platform is that it allows users to design any customized imaging sequence by flexible, serial allocation of "imaging modules" and selection of relevant imaging parameters according to their specific need, as shown in Figure 40. Based on the designed imaging sequence, the CLUE imaging platform scalably generates all relevant Verasonics objects that are required to run the system.

Table 9 – Imaging modules used in the CLUE imaging platform.

Module name	Description
UF	Ultrafast imaging
UF-PI	Ultrafast pulse inversion imaging
UF-INTL	Ultrafast interleaved imaging
UF-PI-INTL	Ultrafast pulse inversion interleaved imaging
LL	Line-by-line imaging
LL-PI	Line-by-line pulse inversion imaging

LL-INTL	Line-by-line interleaved imaging
LL-PI-INTL	Line-by-line pulse inversion interleaved imaging
PA	Photoacoustic imaging
ExtLaser	Pulsed-laser excitation
IntARF	ARF excitation with an imaging transducer
ExtARF	ARF excitation with an external transducer
Doppler	Color/power Doppler imaging
Idle	Idle time delay (no operation)

The imaging modules consist of 14 fundamental building blocks of the imaging sequence, as defined in Table 9. UF represents ultrafast ultrasound imaging, which acquires a full two-dimensional image with plane-wave compounding, and LL line-by-line ultrasound imaging that sequentially acquires each scanline per transmit-receive event with a focused beam [73]. The UF and LL modules can be extended with either PI or INTL or both. PI supports pulse-inversion-based harmonic imaging and INTL enables multiple acquisition with different transmit offset times to increase the effective sampling rate for high-frequency ultrasound imaging. For example, since the maximum sampling rate of the Verasonics system is 62.5 MHz, two interleaved acquisitions can make the effective sample rate 125 MHz, supporting an effectively doubled center frequency. The PA module only receives the signals, and thus, it usually necessitates a preceding ExtLaser module, which irradiates a laser pulse to generate the photoacoustic signals. Nevertheless, the PA and ExtLaser modules are designed to be independent like other modules. Hence, either one of them can be used independently according to the study purpose. The IntARF and ExtARF modules are to apply an ARF to create shear waves for SWEI. Here, for ARF excitation, the IntARF module uses an imaging transducer connected to the Verasonics system, but the ExtARF module triggers an external transducer. The Doppler module acquires both color and power Doppler images for flow quantification. The Idle module

creates an idle wait step for a user-specified time duration to control the acquisition timings between other modules. These fundamental modules can be used to create various imaging sequences. For example, a simple US/PA imaging sequence can be designed with a series of the UF (or LL), ExtLaser, and PA modules.

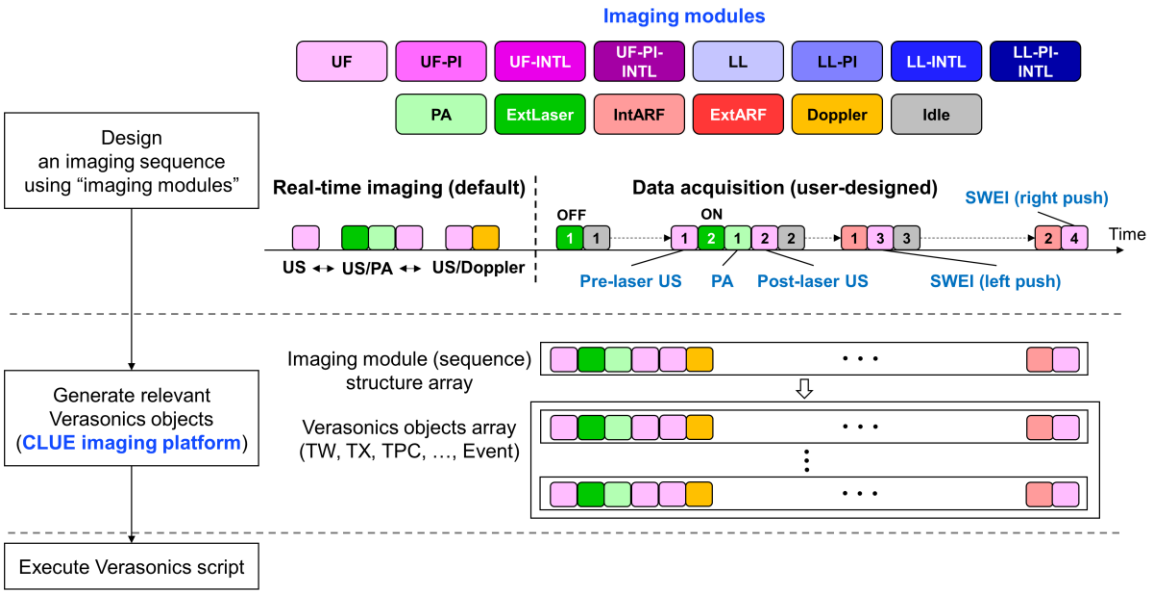

Figure 40 – Design and execution process of an imaging sequence using the CLUE imaging platform. All imaging modules here are uniquely color-coded for better visualization of them for the rest of this chapter.

The CLUE imaging platform offers three default real-time imaging methods: US, US/PA, and US/Doppler imaging modes. A user can switch to any of these three modes in a Verasonics GUI. A button was created on the GUI to execute the user-designed custom imaging sequence. Real-time imaging will be paused when the data acquisition is in process. Once data is acquired and saved for offline processing, real-time imaging will resume. In Figure 40, a representative imaging sequence is shown. First, a sham laser pulse is placed at the beginning for synchronization of the US system and the laser. Because the

timing of pulsed-laser irradiation is determined by periodic Flashlamp OUT triggers of the laser, the sham laser pulse allows the sequence to expect an irradiated timing of the next actual laser pulse, enabling acquisition of US images exactly prior to the actual laser excitation. Specifically, the pulse-repetition frequency (PRF) of the Flashlamp OUT signal is constant at 10 Hz in the Phocus laser (i.e., pulse-repetition interval (PRI) of 100 ms). Thus, the Idle module with an appropriate duration can be inserted right after the irradiation of the sham laser pulse specified by the ExtLaser module. For example, if pre-laser US imaging is to acquire 50 frames at 10 kHz, it will take 5 ms for data acquisition. Thus, 95 ms (= 100 ms (laser PRI) – 5 ms (pre-laser US acquisition)) of the Idle module duration is needed to enable the pre-laser US acquisition right before the actual laser pulse. Following the laser irradiation, corresponding PA and post-laser US images are captured in the imaging sequence. Then, two SWEI processes are executed, where each process consists of two modules: an IntARF module for ARF application and a subsequent UF module for shear wave observation. Here, two IntARF modules in two SWEI processes apply the ARF beams at different lateral positions to cover a complete view of SWEI mapping. The Idle module between two SWEI acquisitions is to ensure the safety limits on acoustic intensities outlined by the Food and Drug Administration [80].

7.2.3 Interface of CLUE Imaging Platform

Verasonics systems are one of the most widely used research ultrasound scanners in a diverse array of applications: from nondestructive evaluation (NDE) to clinical diagnosis (http://verasonics.com/scientific-references/). A user can design and use their imaging sequence by defining Verasonics objects in the MATLAB (MathWorks, Natick, MA) environment. The Verasonics objects are classified in two groups: global system

objects and sequence objects. The global system objects (Resource, Trans, and PData) define system specifications, medium properties, and transducer characteristics. The sequence objects (TW, TX, TPC, Receive, Recon, ReconInfo, Process, Event, and SeqControl) determine a sequence of imaging, image reconstruction, and image display. Thus, as shown in the left part of Figure 41, a user is required to define all Verasonics objects to run their script on the system (various example scripts and a detailed user manual are provided with the system).

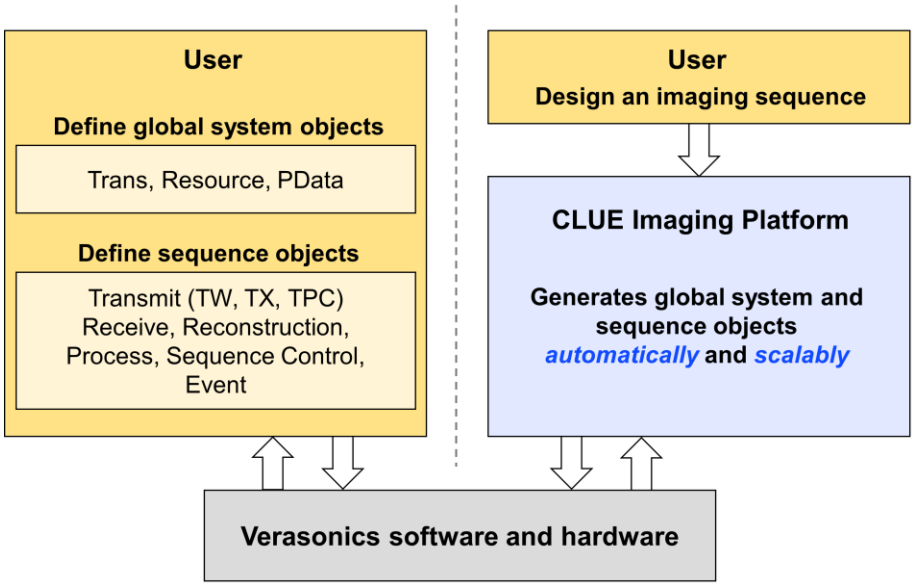

Figure 41 – A diagram showing the role of the CLUE imaging platform in interfacing users and Verasonics software and hardware.

The CLUE imaging platform is a module-based configurable imaging platform, providing non-advanced users a shortcut to sophisticated imaging sequences. As shown in the right part of Figure 41, the CLUE imaging platform interfaces Verasonics software and hardware on behalf of a user, and thus, one only needs to define their imaging sequence by allocating the imaging modules listed in Table 9. All objects required in the Verasonics

programming script are generated by our platform automatically. Once the imaging sequence is defined, relevant parameters per imaging module can be set in the script or through a custom-made GUI. In Figure 42, all imaging modules used in the imaging sequence appear as color-coded buttons. Each module or button can be chosen to adjust relevant parameters listed in the table on the right panel. Then, the CLUE imaging platform creates the corresponding Verasonics objects scalably according to the designed imaging modules with the determined parameters.

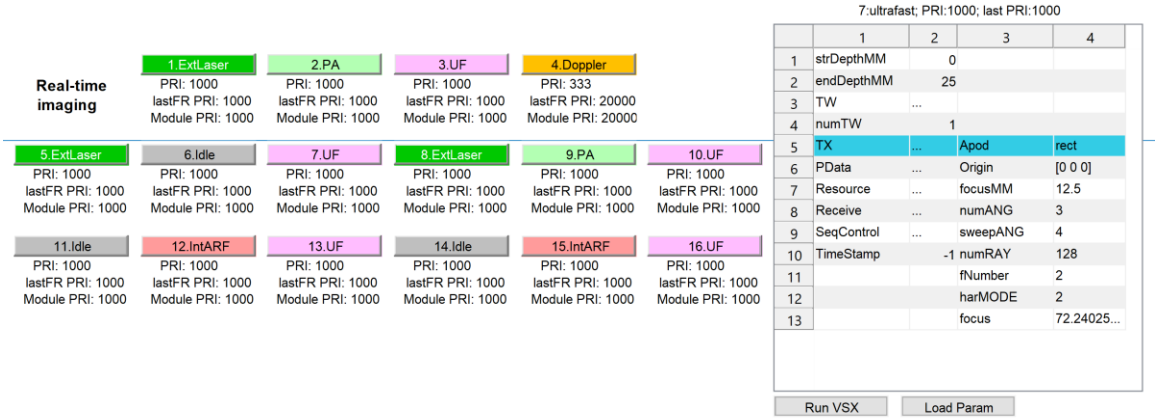

Figure 42 – A graphical user interface for setting imaging parameters of all imaging module.

7.3 Experimental Methods and Materials

7.3.1 Combined Laser, Ultrasound, and Elasticity (CLUE) Imaging

To demonstrate the integrated implementation of various ultrasound-based imaging modules, our CLUE imaging sequence includes ultrafast US imaging, PA imaging, and SWEI. The combination of the first two are to detect the PFHnDs, which can be used for contrast-enhanced or super-resolution imaging [55-57]. The PFHnDs vaporize and recondense in response to pulsed-laser irradiation and their transient response requires

high-frame-rate US imaging [57]. In addition, the vaporization event also provides strong PA signals. Thus, in the CLUE imaging sequence shown in Figure 43, we used two respective UF imaging modules before and after laser pulses to capture the dynamic response of the PFHnDs (blue rectangle). The differential US (ΔUS) image, which is obtained by subtracting pre- and post-laser US images, is used to visualize the vaporized PFHnDs. In addition, three SWEI sequences with three ARFs applied at different lateral positions (left/right/middle) follow (red rectangle). The propagation of shear waves was visualized through a two-dimensional auto-correlation approach [161] and these shear waves were used to reconstruct the corresponding SWV maps using a two-dimensional cross-correlation approach [76]. Overall, IQ data generated from all imaging modules were saved immediately after acquisition, and the result images were processed offline.

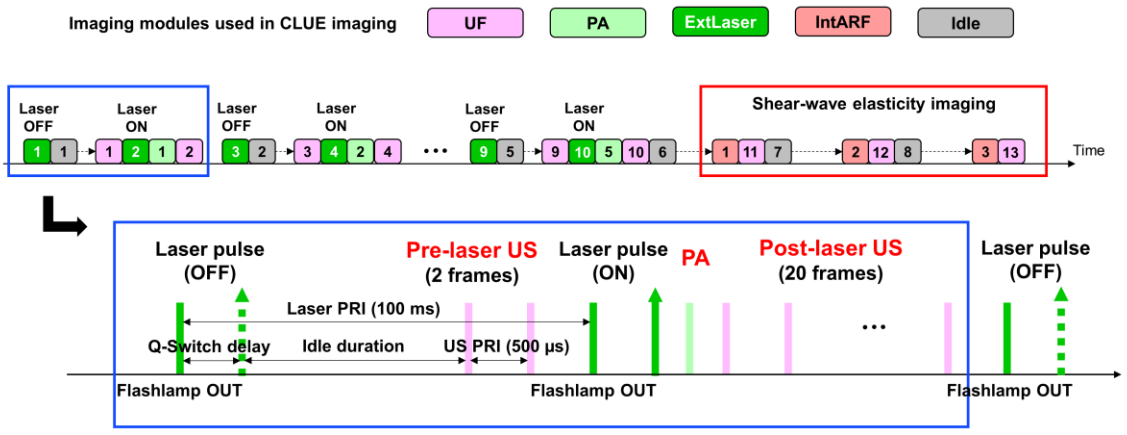

Figure 43 – A proposed CLUE imaging sequence including 5 sets of pre-laser US, PA, and post-laser US imaging as a function of optical fluence and three sets of SWEI sequences.

This study used a linear array ultrasound transducer (CL15-7; Philips Healthcare, Andover, MA, USA). Table 10 lists all parameters used in the CLUE imaging sequence.

Laser pulsing was repeatedly disabled and enabled to obtain pre-laser US images immediately prior to the actual laser pulse (for example, UF 1 is placed before ExtLaser 2 in Figure 43). Thus, the Idle module was used to control the acquisition time. The desired duration of the Idle module was computed by subtracting a Q-Switch delay and a pre-laser US acquisition duration from the laser PRI (100 ms). Immediately after irradiating a laser pulse, PA imaging and subsequent post-laser US imaging followed. This study applied 5 actual laser pulses as a function of Q-Switch delay to demonstrate its ability to adjust the optical fluence with respect to laser pulse, which allows for evaluation of the optical vaporization threshold of the PFHnDs. The Q-Switch delay decreased with each successive laser pulse (400, 350, 300, 270, 250 μs), increasing the irradiated optical fluence accordingly. The average measured fluence values were 33, 54, 77, 90, and 94 mJ/cm^2.

SWEI in the CLUE imaging sequence consisted of three ARF applications and three ultrafast ultrasound acquisitions to obtain the mechanical properties of tissue. As listed in Table 10, the ARFs were applied at three lateral locations and the propagation of the shear waves were respectively tracked at a PRF of 10 kHz. Three angles of plane waves were used for angular compounding [73]. For the ARF beams, f-number of 2.5, a focal depth of 17.5 mm, a pulse duration of 200 μs, and a center frequency of 6.5 MHz were used. Between pushing and tracking events, an interval of 500 ms was placed using the Idle module.

Table 10 – Imaging parameters used in the CLUE imaging sequence.

	Ultrafast US and PA imaging of PFHnDs							SWEI	
	Laser pulsing (fake)	No operation	Pre-laser US	Laser pulsing (actual)	PA	Post-laser US	ARF	US tracking	No operation
Imaging module	ExtLaser	Idle	UF	ExtLaser	PA	UF	IntARF	UF	Idle
Module number	1,3,5,7,9	1,2,3,4,5	1,3,5,7,9	2,4,6,8,10	1,2,3,4,5	2,4,6,8,10	1,2,3	11,12,13	7,8
Wavelength	1064 nm			1064 nm					
Enable	False			True					
Q-Switch delay (µs)	400, 350, 300, 270, 250			400, 350, 300, 270, 250					
Idle duration		~97.7							500 ms
No. frames			2		1	20		120	
No. plane waves			1			1		3	
Sweeping angles			0°			0°		−2°, 0°, 2°	
PRI (1/PRF)	100 ms		500 µs	100 ms	250 µs	500 µs		100 µs	
Center frequency			8.9 MHz			8.9 MHz	6.5 MHz	8.9 MHz	
ARF lateral location (mm)							−7, 0, 7		
Focal depth							17.5 mm		
ARF duration							200 µs		
f-number							2.5		

7.3.2 Synthesis of Perfluorohexane Nanodroplets (PFHnDs)

Perfluorohexane nanodroplets were synthesized using a sonication-based protocol. Briefly, 1 µmol of DSPC and DSPE-mPEG2000 in a 1:9 molar ratio were isolated along with 0.5 mg of near-infrared-absorbing dye (IR-1048; Sigma-Aldrich) from a chloroform solution using a rotary evaporator. After rotary evaporation produced an even cake of lipid and dye, the solid isolate was further dried under nitrogen flow in order to evaporator all residual chloroform.

Next, the solid reagents were hydrated with 1 mL of 7.40 pH PBS and agitated using a water bath sonicator to produce a solution of dye-loaded nanomicelles. This solution was centrifuged at 300 rcf for 1 minute in order to pellet excess near-infrared dye. Then, 900 µL of the nanomicelle-containing supernatant was combined with 100 µL of PBS and 50 µL of perfluorohexane. This solution was then probe sonicated (1s on, 15 s off, 5 times) on ice in order to produce a stock solution of PFHnDs.

Prior to their use for imaging, 100 µL of PFHnDs were diluted in 2 mL of PBS and bath sonicated for 5 minutes. This solution would then be centrifuged at 3000 rcf for 5 minutes in order to pellet PFHnDs. The supernatant would then be removed and the PFHnDs would be reconstituted in 100 µL of sterile saline for imaging. This protocol produces PFHnDs with an average hydrodynamic diameter of 222 nm measured via dynamic light scattering (Zetasizer Nano ZS; Malvern Instruments Ltd.) and at a concentration of approximately 10^{10} PFHnDs/mL as assessed by nanoparticle tracking analysis (NanoSight NS300; Malvern Panalytical).

7.3.3 Tissue-Mimicking Phantom Synthesis and Imaging

A tissue-mimicking gelatin phantom containing a cylindrical stiff inclusion labeled with the synthesized PFHnDs was fabricated to demonstrate the CLUE imaging sequence. The diameter of the inclusion was 7 mm. The concentrations of the gelatin powders in the inclusion and background were 12% w/v and 6% w/v, respectively. Thus, a SWV ratio of the inclusion to the background was expected to be two, as the stiffness of a gelatin phantom is proportional to its gelatin concentration. The v/v ratio of the as-prepared PFHnDs solution to the inclusion was 1:1000. For acoustic scattering, 0.5% w/v silica particles were included both in the inclusion and in the background. The imaging depth of the center of the inclusion was approximately 17.5 mm. The CLUE imaging sequence was repeated three times to evaluate means and standard deviations (SDs) of the pre-laser US, PA, post-laser US, ΔUS, and SWV images over independent measurement.

7.3.4 Mouse Spleen Preparation for Ex Vivo Imaging

All animal procedures were performed under the oversight of the Institutional Animal Care and Use Committee at the Georgia Institute of Technology. For *ex vivo* spleen imaging, an 18-week-old female athymic nude mouse (NU/J; The Jackson Laboratory) was placed under general anesthesia with isoflurane (5% induction, 2.5% maintenance; 0.5 L/min O_2) and injected via the jugular vein with 140 µL of 10^{10} PFHnD/mL particles, prepared as described in section "B." After injection, the mouse was returned to consciousness and kept in the Animal Resources Facility at Georgia Tech for 24 hours. This time allows for injected particles to be filtered within splenic sinusoids and endocytosed by resident reticuloendothelial cells. After 24 hours, the mouse was humanely euthanized by an intraperitoneal lethal injection of Euthasol (Sodium pentobarbital 390 mg/ml, 150 mg/kg; Henry Schein Medical). Following cessation of the heartbeat,

euthanasia was confirmed by secondary cervical dislocation. Immediately after secondary euthanasia, the spleen was dissected and kept submerged in 6.80 pH-buffered PBS solution prior to phantom inclusion.

Within two hours post-resection, the mouse spleen was immediately embedded in a gelatin phantom to fix its movement and improve the acoustic coupling. Then, the mouse spleen was imaged using the same CLUE imaging sequence as described previously.

7.4 Results and Discussion

7.4.1 CLUE Imaging of a Phantom Containing a Stiff Inclusion

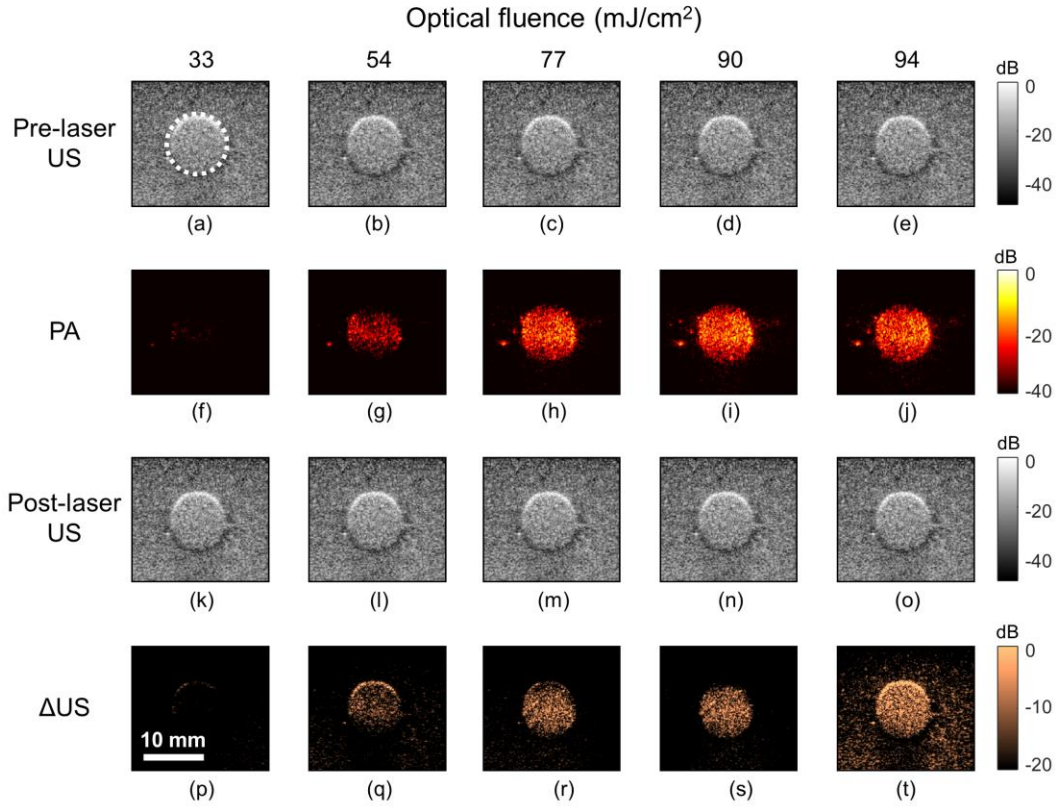

Figure 44 – Processed pre-laser US, PA, post-laser US, and ΔUS images as a function of optical fluence obtained from the tissue-mimicking gelatin phantom.

The CLUE imaging sequence introduced in Figure 43 was applied to the gelatin phantom containing a stiff cylindrical inclusion. Figure 44 shows the corresponding pre-laser US, PA, post-laser US, and ΔUS images as a function of laser pulse. At the lowest fluence (i.e., 33 mJ/cm^2) in Figure 44 (a) and (p), almost no PA and ΔUS signals were detectable, and thus, we conclude that the laser pulse at this fluence level did not activate the PFHnDs. As optical fluence increased from 33 mJ/cm^2 to 94 mJ/cm^2, the number of triggered PFHnDs increased, resulting in the growing PA and ΔUS signals. However, in pre- and post-laser B-scan US images (the first and third row images), no obvious differences were observable. This is because the signals coming from the vaporized PFHnDs were relatively subtle compared to those from other acoustic scatters in the phantom. Thus, taking a difference between pre- and post-laser US images (i.e., ΔUS images) shown in the fourth row (Figure 44 (p), (q), (r), (s), and (t)) could be useful in identifying the optical activation of the PFHnDs for high-contrast imaging.

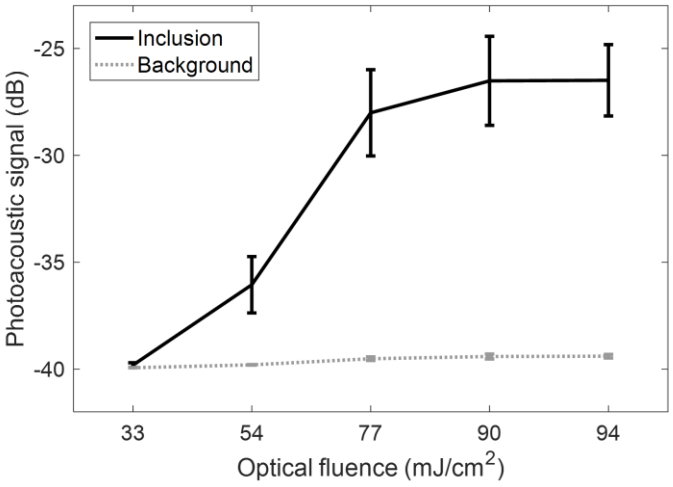

Figure 45 – Means and SDs of PA signals obtained inside and outside of the inclusion as a function of optical fluence.

Means and SDs of the PA signals in the stiff inclusion (region-of-interest for the inclusion is circled with a white dotted line in Figure 44 (a)) and in the background region were computed with three measurements as shown in Figure 45. The background mean PA signals did not change significantly with respect to optical fluence and were consistently negligible (gray dotted line), but the PFHnDs contained in the inclusion resulted in increasing mean PA signals (black solid line). As the vaporization process is a combined, complex function of various factors including droplet size, local fluence, amount of dye encapsulated, and local temperature [57], the PFHnDs vaporize stochastically. Thus, the vaporization threshold is unique to each formulation. Therefore, the increase in the mean PA signal resulting from the expansion of the PFHnDs is not completely discrete as shown in Figure 45.

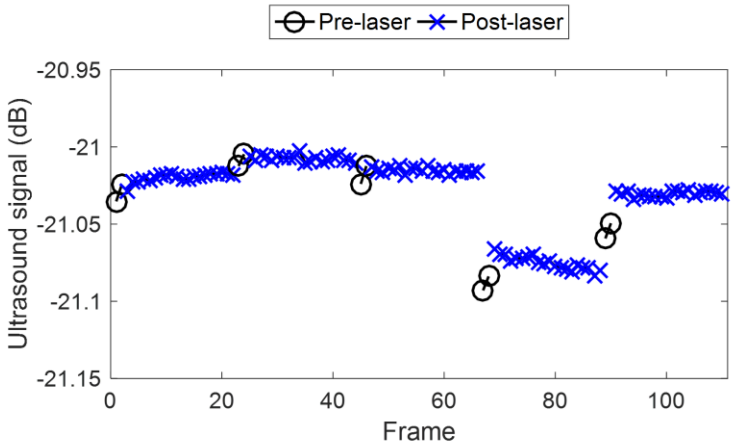

Figure 46 – Combined 5 sets of means of pre- and post-laser US signals in the inclusion as a function of US frame.

Mean ultrasound signals of all 5 sets from both pre- and post-laser US images are shown together as a time series in Figure 46 as a function of frame. Since we acquired two pre-laser US frames and 20 post-laser US frames per laser pulse, the application of five

laser pulses produced a total of 110 (5 x 22) US frames. Every first two frames in 22 frames are pre-laser US frames indicated with black circles and the other 20 frames are post-laser US images indicated with blue x marks. The first three sets did not obviously show clear changes between pre- and post-laser US signals. The fourth and fifth transitions from pre- to post-laser US signals are clearer, although their differences are still not substantial. These results indicate that when the PFHnD signals are mixed with the endogenous US signals from acoustic scatters, the PFHnD vaporization may not be easily detectable with typical grayscale US images. Pre- and post-laser US images (first and third row images in Figure 44) are also almost visually identical.

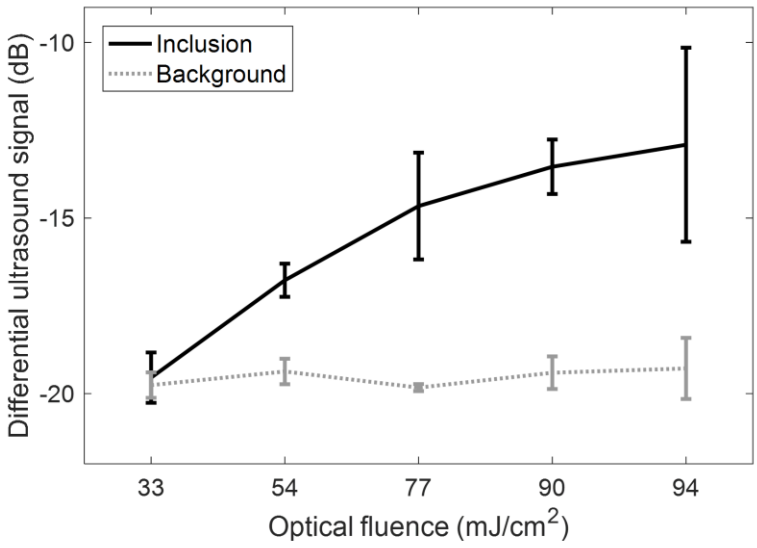

Figure 47 – Means and SDs of ΔUS signals obtained inside and outside of the inclusion as a function of optical fluence.

ΔUS images removing background signals showed the vaporized PFHnDs with high contrast (fourth row images in Figure 44). Means and SDs of ΔUS signals inside and outside of the inclusion were computed and plotted in Figure 47. Like the results observed

in Figure 45, the mean ΔUS signals in the background (gray dotted line) do not change as a function of fluence, but those in the inclusion (black solid line) increased as optical fluence increased, which vaporized more PFHnDs.

On the same target, and at the same time, the CLUE imaging sequence obtained the SWEI results as shown in Figure 48. We applied three ARF beams at different lateral locations (−7 mm, +7 mm, and 0 mm) and observed the corresponding generation and propagation of the shear waves. Three rows in Figure 48 represent three lateral locations of ARF application. As the shear waves propagate through the stiff region, they became faster, as observed in the axial velocity sequences at multiple downstream time points (the second to fifth column images in Figure 48). The respective SWV maps reconstructed from each axial velocity sequence are shown in Figure 48 (f), (l), and (r). On the regions where the push beams were applied, the propagation of the shear waves is not observable. Therefore, the SWVs on the pushing regions are unreliable. This limitation typically requires multiple applications of ARF beams at different lateral locations to span the full field-of-view while still omitting unwanted regions in the SWV map prior to combining multiple SWV maps.

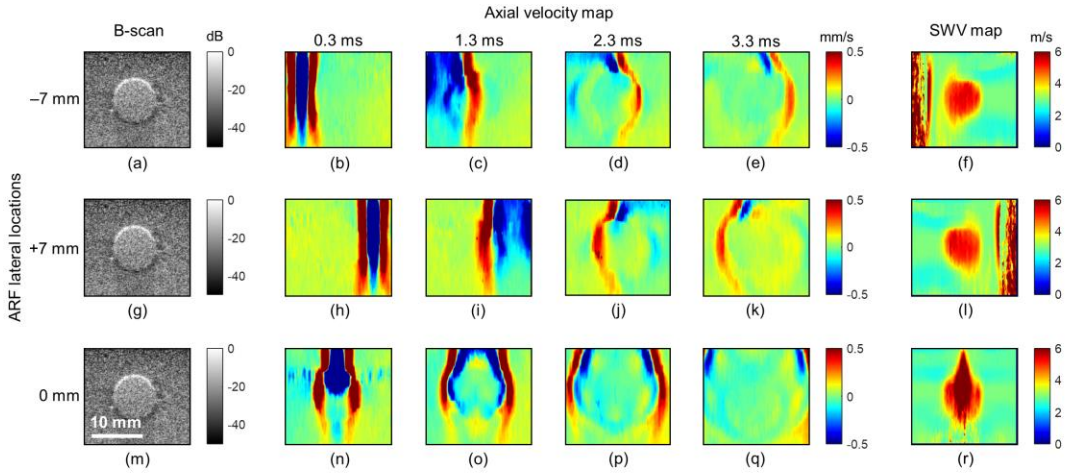

Figure 48 – Estimated axial velocity sequences visualizing the propagation of the shear waves generated at three lateral locations in the gelatin phantom and three corresponding SWV maps.

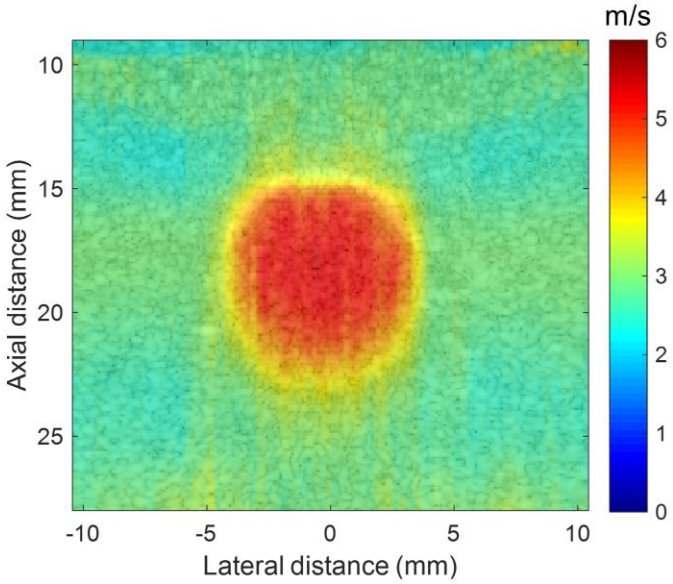

Figure 49 – A combined SWV map overlaid on a B-scan US image of the gelatin phantom.

The combined SWV map from the three acquired SWV maps is given in Figure 49. The inclusion center was placed at 17.5 mm in depth. We found that mean SWVs inside

and outside of the inclusion were 4.22 m/s, and 2.81 m/s, respectively. The ratio of square of them was 2.27, which is close to the ratio of the gelatin concentration of the inclusion to that of the background (i.e., 12% / 6% = 2).

Overall, we have demonstrated that the CLUE imaging sequence is able to sense multiple properties of the imaging target simultaneously through our gelatin phantom study. The stiff PFHnD-labeled inclusion offered both the laser-induced contrast by PA and ΔUS imaging and mechanical contrast by SWEI. A further imaging study on a phantom containing multiple contrast sources distributed amongst multiple targets is necessary.

7.4.2 CLUE imaging of Ex Vivo Spleen

To further demonstrate the feasibility of CLUE imaging, we imaged a cross-section of an *ex vivo* mouse spleen embedded in a homogeneous gelatin background as shown in Figure 50.

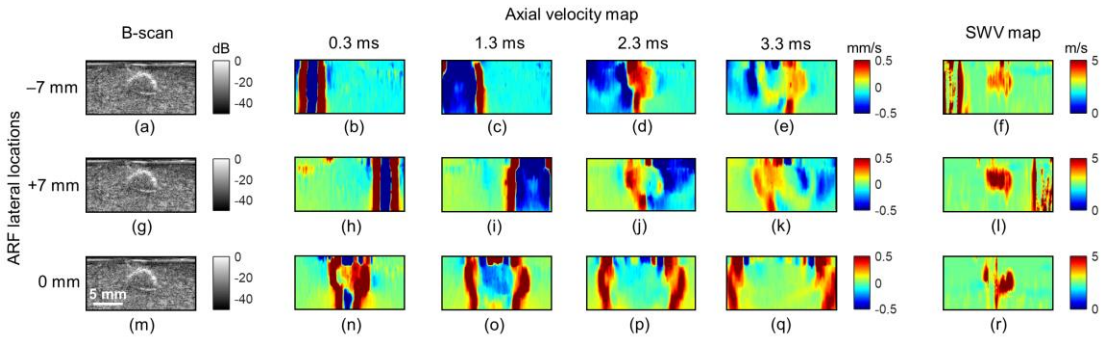

Figure 50 – Estimated axial velocity sequences visualizing the propagation of the shear waves generated at three lateral locations in the phantom embedding the *ex vivo* mouse spleen and three corresponding SWV maps.

Similar to the gelatin inclusion study introduced in the previous section, no overt differences between pre- and post-laser US images can be observed over increasing optical fluences. However, we could confirm that the intravenously injected PFHnDs successfully accumulated in the spleen before extraction. Therefore, similar to the phantom case, the PA and ΔUS signals inside the spleen increased due to the increased vaporization of PFHnDs as a function of optical fluence.

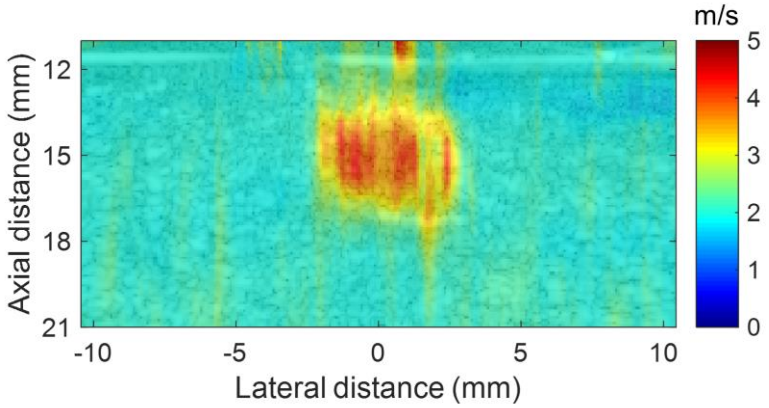

Figure 51 – A combined SWV map overlaid on a B-scan US image of the *ex vivo* mouse spleen.

From the estimated axial velocity sequences in Figure 50, it is observed that shear waves were successfully created and propagated through the spleen. As shown in Figure 50, the spleen seemed to be stiffer than the gelatin background, which resulted in faster SWVs propagating through the spleen. Three SWV maps acquired at three lateral positions were again reconstructed from the corresponding axial velocity sequences, but there is a noticeable difference in the SWVs in the spleen between Figure 50 (f) and (l). This is possibly due to the unexpected broadening of shear waves [162], as the shear wave front in Figure 50 (e) seems to be wider (i.e., more blurred) and unclear than that in Fig. 13 (k).

A final SWV map of the mouse spleen combined from three SWV maps is presented in Figure 51.

7.4.3 Potential Limitations and Utilities of CLUE Imaging

CLUE imaging may not be able to always capture all mechanical, optical, acoustic information in soft tissue. One of the most critical concerns would be a limitation in light penetration. Because of optical absorption and scattering, pulsed-laser light becomes diffuse in biological tissue. Although near-infrared light can reach depths at several centimeters, PA imaging of deep tissue is still challenging [163]. Furthermore, sPA imaging of chromophore concentrations gets significantly inaccurate as the imaging target goes deeper or the PA signal-to-noise ratio gets lower [164]. On the other hand, SWEI relies on the ARF application to generate and thus to monitor shear waves. However, because of the attenuation of shear waves, adequate generation of shear waves is desired [24, 27, 28]. In addition, the generation of shear waves is highly dependent on the regional characteristics of tissue, such as, coupling stress resulting from internal organs, boundary conditions, and viscoelasticity [165]. Thus, given these physical challenges in PA imaging and SWEI, CLUE imaging could be partially functional in a region of interest dependent upon depth and local tissue properties. In other words, a region of interest, where PA imaging is insensitive, can rely on SWEI and vice versa.

CLUE imaging has promising potential in various clinical applications. Not only does CLUE imaging help to understand progress, status, and prognosis of disease, but also it can be a valuable tool for therapeutic guidance. Currently, assessment of a treatment response of cancer is likely delayed, as monitoring the reduction of the tumor size is used

as a standard method [29]. Thus, it may be beneficial to apply CLUE imaging to monitor the changes in both mechanical and functional properties of cancer in response to specific therapy, as it can provide immediate and collective information on treatment progress. For example, sPA imaging and SWEI have shown their respective capabilities in evaluating various therapeutic approaches, which may be further improved with CLUE imaging [29, 30, 40, 157]. Monitoring oxygenation of a tumor for effective therapeutic radiation sensitization and promptly evaluating its response to radiation would be feasible using sPA imaging and SWEI, respectively, which would be simultaneously possible through CLUE imaging.

7.5 Conclusion

This chapter has introduced and designed the CLUE imaging platform and sequence as a research tool for comprehensive cancer diagnosis. Furthermore, the development of the CLUE imaging platform will also support imaging studies for ultrasound researchers in a wide array of disease applications. In our module-configurable, scalable CLUE platform, an arbitrary imaging sequence can be created by allocating pre-defined imaging modules. To demonstrate the developed CLUE imaging platform in the tissue-mimicking gelatin phantom and the *ex vivo* mouse spleen, we have applied a representative CLUE imaging sequence, which can acquire pre-laser US, PA, post-laser US, and SWV images. The imaging results collectively showed multiple desired imaging contrast—acoustic, optical, and mechanical—from both the PFHnD-labeled stiff inclusion and the PFHnD-laden spleen, suggesting that the introduced CLUE imaging platform and sequence can be potentially used to provide comprehensive soft tissue assessment.

7.6 Acknowledgements

The authors would like to thank Donald VanderLaan and Andrei B. Karpiouk of the Georgia Institute of Technology for their help with the laser system hardware and Vadakkancheril S. Jisha of the Georgia Institute of Technology for her help with the preliminary imaging studies.

CHAPTER 8. CONCLUSIONS AND FUTURE WORK

8.1 Conclusions

Medical ultrasound imaging is one of most widely used modalities in clinic as it is highly portable, real-time, noninvasive, and cost-effective. However, traditional gray scale ultrasound imaging lacks functional, molecular, and mechanical information on tissue, limiting its utility as a first-line screening tool. In other words, because comprehensive diagnostic information on cancer and other diseases is unattainable with ultrasound imaging, accurate and early diagnosis is challenging in ultrasound imaging.

To alleviate this limitation and improve the utility of ultrasound imaging, various ultrasound-based imaging techniques including SWEI, sPA imaging, and imaging of PFHnDs have been investigated. The primary goals of this research are to engineer and improve these imaging methods to enhance their diagnostic abilities, and ultimately, to combine these imaging techniques in a configurable CLUE imaging platform to enable comprehensive diagnosis of cancer with single imaging modality.

Due to the previous studies from researchers in this field and fruitful collaboration with lab members, this research could advance these imaging techniques. For SWEI, the effective use of multi-angular shear waves utilizing grating lobes was proposed and verified that it can improve the quality of shear-wave velocity images. For sPA imaging, a depth-optimized wavelength selection method was introduced and demonstrated numerically. It was shown that the proposed method can quantify concentrations of chromophores accurately for improved blood oxygen saturation estimation. A method

localizing PFHnDs in real-time was introduced to provide sustained contrast-enhanced images to identify lymph node better. In addition, a temporal averaging approach that improves spatial resolution of super-resolution imaging with the PFHnDs was suggested and demonstrated. Furthermore, to utilize the full potential of the PFHnDs, multi-wavelength PA and plane-wave US imaging was introduced and showed that it enables acoustic observation of the PFHnDs as a function of both optical wavelength and time. Lastly, an imaging platform that is able to combine all these imaging methods referred to as CLUE imaging platform was introduced and designed. The proposed CLUE imaging platform not only supports the CLUE imaging sequence itself, but also enables various user-specific arbitrary imaging sequences because the CLUE imaging platform is designed to be module-configurable and scalable.

These technical contributions and improvements in noninvasive ultrasound imaging in this research will help improving comprehensive understanding of cancer and other diseases at an earlier stage with higher accuracy. I hope that the CLUE imaging platform and sequence will be used to solve various health problems, and thus, will contribute advances in healthcare and make our society well-being.

8.2 Future Directions

8.2.1 In vivo Human Thyroid Study using Multiangular Compound Shear-Wave Elasticity Imaging (MAC-SWEI)

About 95% of thyroid nodules are benign, but most patients undergo additional imaging studies or biopsy because their benignity cannot be accurately characterized by standard ultrasound scanning [166, 167]. Thus, as one of on-going studies in our laboratory,

MAC-SWEI has been applied to human patients with thyroid nodules to assess its ability in differentiating malignant from benign thyroid nodules. When using the MAC-SWEI, three pushing configurations created with $\Delta\phi$'s of 0°, 140°, and 180° have been applied in the middle of the transducer and two pushing configurations with $\Delta\phi$ of 0° have been applied sequentially in the left and the right sides of the transducer [28]. Thus, five pushing and tracking sequences have been applied to each patient and resulted in four shear wave velocity (SWV) images—one from the first three pushing and the other from the last two pushing—through off-line post-processing. The specificity and the sensitivity of each SWV image with the corresponding pathology results will be evaluated. The Emory institutional review board (IRB) had approved our system and imaging protocol, and patient scanning has been started from November 2017. The total number of patients scanned is to be more than 20 patients.

8.2.2 Combined Laser, Ultrasound, and Elasticity (CLUE) Imaging for In Vivo Mouse Breast Cancer Characterization

The developed and demonstrated CLUE imaging platform and sequence will be further evaluated with preclinical mouse model of breast cancer. Not only diagnosis of cancer, but also monitoring therapeutic response of cancer will be investigated. To evaluate malignancy of a tumor and detect the cancer early, rigorous studies on SWEI, sPA imaging, and contrast-enhanced US imaging have been investigated in this research field. However, these studies have been studied independently, and none of combined comprehensive imaging studies was approached. Primary and metastatic cancer shows different mechanical and functional properties as it progresses. Depending on its stage, changes in mechanical and functional properties of cancer can differ, which can be used to stage and

characterize the cancer. As the CLUE imaging platform and sequence uniquely provide quantitative mechanical, functional, and compositional information on cancer, it can be used for advanced cancer imaging.

8.2.3 Three-Dimensional CLUE Imaging using a Two-Dimensional Matrix Array

The CLUE imaging platform and sequence were developed on the Verasonics system using one-dimensional array transducers providing two-dimensional (2-D) images. The capability of the CLUE will be greatly improved if it adopts 2-D array transducers for three-dimensional (3-D) volume imaging as imaging a 2-D cross-section of cancer only shows part of cancer, limiting potential of the comprehensive CLUE imaging sequence. To expand the CLUE imaging sequence with a 2-D matrix array transducer, an effective data acquisition strategy is desired as 2-D matrix array transducers has typically at least four times more elements than 1-D array transducers. Our on-going research project uses a 1024-element matrix array driven by the 256-channel Verasonics system using PCIe-based RF data transfer. Data transfer rate and channel memory in the Verasonics system are limited, and thus considered carefully. In addition, different clinical applications require different volume rates. Therefore, data acquisition strategy should be deliberately studied to acquire volume RF data efficiently and stably, which will be used for 3-D CLUE imaging eventually.

REFERENCES

[1] R. L. Siegel, K. D. Miller, and A. Jemal, "Cancer statistics, 2017," *CA Cancer J. Clin.,* vol. 67, pp. 7-30, 2017.

[2] L. Fass, "Imaging and cancer: A review," *Mol. Oncol,,* vol. 2, pp. 115-152, 2008.

[3] D. Hanahan and Robert A. Weinberg, "Hallmarks of Cancer: The Next Generation," *Cell,* vol. 144, pp. 646-674, 2011.

[4] A. A. Alizadeh, V. Aranda, A. Bardelli, C. Blanpain, C. Bock, C. Borowski, *et al.*, "Toward understanding and exploiting tumor heterogeneity," *Nat. Med.,* vol. 21, pp. 846-853, 2015.

[5] D. L. Longo, "Tumor Heterogeneity and Personalized Medicine," *N. Engl. J. Med.,* vol. 366, pp. 956-957, 2012.

[6] J. V. Frangioni, "New Technologies for Human Cancer Imaging," *J. Clin. Oncol.,* vol. 26, pp. 4012-4021, 2008.

[7] C. Tempany, J. Jayender, T. Kapur, R. Bueno, A. Golby, N. Agar, *et al.*, "Multimodal Imaging for Improved Diagnosis and Treatment of Cancers," *Cancer,* vol. 121, pp. 817-827, 2015.

[8] L. Martí-Bonmatí, R. Sopena, P. Bartumeus, and P. Sopena, "Multimodality imaging techniques," *Contrast Media Mol. Imaging,* vol. 5, pp. 180-189, 2010.

[9] R. Guo, G. Lu, B. Qin, and B. Fei, "Ultrasound Imaging Technologies for Breast Cancer Detection and Management: A Review," *Ultrasound Med. Biol.,* vol. 44, pp. 37-70, 2018.

[10] Z. Li, M. Ren, J. Tian, S. Jiang, Y. Liu, L. Zhang, *et al.*, "The Differences in Ultrasound and Clinicopathological Features between Basal-Like and Normal-Like Subtypes of Triple Negative Breast Cancer," *PLoS ONE,* vol. 10, p. e0114820, 2015.

[11] S. Sarkar and S. Das, "A Review of Imaging Methods for Prostate Cancer Detection: Supplementary Issue: Image and Video Acquisition and Processing for Clinical Applications," *Biomed. Eng. Comput. Biol.,* vol. 7s1, p. BECB.S34255, 2016.

[12] B. Ariff, C. R. Lloyd, S. Khan, M. Shariff, A. V. Thillainayagam, D. S. Bansi, *et al.*, "Imaging of liver cancer," *World J. Gastroenterol.,* vol. 15, pp. 1289-1300, 2009.

[13] C. Xie, P. Cox, N. Taylor, and S. LaPorte, "Ultrasonography of thyroid nodules: a pictorial review," *Insights Imaging,* vol. 7, pp. 77-86, 2016.

[14] R. J. Hooley, L. M. Scoutt, and L. E. Philpotts, "Breast Ultrasonography: State of the Art," *Radiology,* vol. 268, pp. 642-659, 2013.

[15] J. Bamber, D. Cosgrove, C. F. Dietrich, J. Fromageau, J. Bojunga, F. Calliada, *et al.*, "EFSUMB guidelines and recommendations on the clinical use of ultrasound elastography. Part 1: basic principles and technology," *Ultraschall Med.,* vol. 34, pp. 169-184, 2013.

[16] T. Shiina, K. R. Nightingale, M. L. Palmeri, T. J. Hall, J. C. Bamber, R. G. Barr, *et al.*, "WFUMB Guidelines and Recommendations for Clinical Use of Ultrasound Elastography: Part 1: Basic Principles and Terminology," *Ultrasound Med. Biol.,* vol. 41, pp. 1126-1147, 2015.

[17] S. Mallidi, G. P. Luke, and S. Emelianov, "Photoacoustic imaging in cancer detection, diagnosis, and treatment guidance," *Trends Biotechnol.,* vol. 29, pp. 213-221, 2011.

[18] K. S. Valluru and J. K. Willmann, "Clinical photoacoustic imaging of cancer," *Ultrasonography,* vol. 35, pp. 267-280, 2016.

[19] O. F. Kaneko and J. K. Willmann, "Ultrasound for molecular imaging and therapy in cancer," *Quant. Imaging Med. Surg.,* vol. 2, pp. 87-97, 2012.

[20] D. Cosgrove, F. Piscaglia, J. Bamber, J. Bojunga, J. M. Correas, O. H. Gilja, *et al.*, "EFSUMB Guidelines and Recommendations on the Clinical Use of Ultrasound Elastography.Part 2: Clinical Applications," *Ultraschall in Med,* vol. 34, pp. 238-253, 2013.

[21] M. Tanter, J. Bercoff, A. Athanasiou, T. Deffieux, J.-L. Gennisson, G. Montaldo, *et al.*, "Quantitative Assessment of Breast Lesion Viscoelasticity: Initial Clinical Results Using Supersonic Shear Imaging," *Ultrasound Med. Biol.,* vol. 34, pp. 1373-1386, 2008.

[22] A. P. Sarvazyan, M. W. Urban, and J. F. Greenleaf, "Acoustic Waves in Medical Imaging and Diagnostics," *Ultrasound Med. Biol.,* vol. 39, pp. 1133-1146, 2013.

[23] A. P. Sarvazyan, O. V. Rudenko, S. D. Swanson, J. B. Fowlkes, and S. Y. Emelianov, "Shear wave elasticity imaging: a new ultrasonic technology of medical diagnostics," *Ultrasound Med. Biol.,* vol. 24, pp. 1419-1435, 1998.

[24] J. Bercoff, M. Tanter, and M. Fink, "Supersonic shear imaging: a new technique for soft tissue elasticity mapping," *IEEE Trans. Ultrason. Ferroelectr. Freq. Control,* vol. 51, pp. 396-409, 2004.

[25] K. Nightingale, M. S. Soo, R. Nightingale, and G. Trahey, "Acoustic radiation force impulse imaging: in vivo demonstration of clinical feasibility," *Ultrasound Med. Biol.,* vol. 28, pp. 227-235, 2002.

[26] S. Chen, M. W. Urban, C. Pislaru, R. Kinnick, Y. Zheng, A. Yao, *et al.*, "Shearwave dispersion ultrasound vibrometry (SDUV) for measuring tissue elasticity and viscosity," *IEEE Trans. Ultrason., Ferroelect., Freq. Control,* vol. 56, pp. 55-62, 2009.

[27] P. Song, H. Zhao, A. Manduca, M. W. Urban, J. F. Greenleaf, and S. Chen, "Comb-push ultrasound shear elastography (CUSE): a novel method for two-dimensional shear elasticity imaging of soft tissues," *IEEE Trans. Med. Imaging,* vol. 31, pp. 1821-1832, 2012.

[28] H. Yoon, S. R. Aglyamov, and S. Y. Emelianov, "Dual-Phase Transmit Focusing for Multiangle Compound Shear-Wave Elasticity Imaging," *IEEE Trans. Ultrason., Ferroelect., Freq. Control,* vol. 64, pp. 1439-1449, 2017.

[29] F. Chamming's, M.-A. Le-Frère-Belda, H. Latorre-Ossa, V. Fitoussi, A. Redheuil, F. Assayag, *et al.*, "Supersonic Shear Wave Elastography of Response to Anti-cancer Therapy in a Xenograft Tumor Model," *Ultrasound Med. Biol.,* vol. 42, pp. 924-930, 2016.

[30] J.-W. Wang, Z.-X. Guo, Q.-G. Lin, W. Zheng, S.-L. Zhuang, S.-Y. Lin, *et al.*, "Ultrasound elastography as an imaging biomarker for detection of early tumor response to chemotherapy in a murine breast cancer model: a feasibility study," *Br. J. Radiol.,* vol. 91, p. 20170698, 2018.

[31] T. Liu, O. A. Babaniyi, T. J. Hall, P. E. Barbone, and A. A. Oberai, "Noninvasive In-Vivo Quantification of Mechanical Heterogeneity of Invasive Breast Carcinomas," *PLoS ONE,* vol. 10, p. e0130258, 2015.

[32] M. Xu and L. V. Wang, "Photoacoustic imaging in biomedicine," *Rev. Sci. Instrum.,* vol. 77, p. 041101, 2006.

[33] P. Beard, "Biomedical photoacoustic imaging," *Interface Focus,* 2011.

[34] S. Zackrisson, S. van de Ven, and S. S. Gambhir, "Light In and Sound Out: Emerging Translational Strategies for Photoacoustic Imaging," *Cancer Res.,* vol. 74, pp. 979-1004, 2014.

[35] M. Toi, Y. Asao, Y. Matsumoto, H. Sekiguchi, A. Yoshikawa, M. Takada, *et al.*, "Visualization of tumor-related blood vessels in human breast by photoacoustic imaging system with a hemispherical detector array," *Sci. Rep.,* vol. 7, p. 41970, 2017.

[36] P. Vaupel and A. Mayer, "Hypoxia in cancer: significance and impact on clinical outcome," *Cancer Metastasis Rev.,* vol. 26, pp. 225-239, 2007.

[37] M. Höckel and P. Vaupel, "Tumor Hypoxia: Definitions and Current Clinical, Biologic, and Molecular Aspects," *Journal of the National Cancer Institute,* vol. 93, pp. 266-276, 2001.

[38] H. F. Zhang, K. Maslov, M. Sivaramakrishnan, G. Stoica, and L. V. Wang, "Imaging of hemoglobin oxygen saturation variations in single vessels in vivo using photoacoustic microscopy," *Appl. Phys. Lett.,* vol. 90, p. 053901, 2007.

[39] Y. Wang, S. Hu, K. Maslov, Y. Zhang, Y. Xia, and L. V. Wang, "In vivo integrated photoacoustic and confocal microscopy of hemoglobin oxygen saturation and oxygen partial pressure," *Opt. Lett.,* vol. 36, pp. 1029-1031, 2011.

[40] S. Mallidi, K. Watanabe, D. Timerman, D. Schoenfeld, and T. Hasan, "Prediction of Tumor Recurrence and Therapy Monitoring Using Ultrasound-Guided Photoacoustic Imaging," *Theranostics,* vol. 5, pp. 289-301, 2015.

[41] G. P. Luke and S. Y. Emelianov, "Label-free Detection of Lymph Node Metastases with US-guided Functional Photoacoustic Imaging," *Radiology,* vol. 277, pp. 435-442, 2015.

[42] L. Meng-Lin, O. Jung-Taek, X. Xie, G. Ku, W. Wei, L. Chun, *et al.,* "Simultaneous Molecular and Hypoxia Imaging of Brain Tumors In Vivo Using Spectroscopic Photoacoustic Tomography," *Proc. IEEE,* vol. 96, pp. 481-489, 2008.

[43] L. Jan, E. Clare, D. Dave, and B. Paul, "In vitro measurements of absolute blood oxygen saturation using pulsed near-infrared photoacoustic spectroscopy: accuracy and resolution," *Phys. Med. Biol,* vol. 50, p. 4409, 2005.

[44] M. J. K. Blomley, J. C. Cooke, E. C. Unger, M. J. Monaghan, and D. O. Cosgrove, "Microbubble contrast agents: a new era in ultrasound," *BMJ : British Medical Journal,* vol. 322, pp. 1222-1225, 2001.

[45] K. Ferrara, R. Pollard, and M. Borden, "Ultrasound Microbubble Contrast Agents: Fundamentals and Application to Gene and Drug Delivery," *Annu. Rev. Biomed. Eng.,* vol. 9, pp. 415-447, 2007.

[46] F. Kiessling, S. Fokong, P. Koczera, W. Lederle, and T. Lammers, "Ultrasound Microbubbles for Molecular Diagnosis, Therapy, and Theranostics," *J. Nucl. Med.,* vol. 53, pp. 345-348, 2012.

[47] K. H. Martin and P. A. Dayton, "Current status and prospects for microbubbles in ultrasound theranostics," *Wiley Interdiscipl. Rev. Nanomed. Nanobiotechnol.,* vol. 5, pp. 329-345, 2013.

[48] P. S. Sheeran and P. A. Dayton, "Phase-Change Contrast Agents for Imaging and Therapy," *Curr. Pharm. Des.,* vol. 18, pp. 2152-2165, 2012.

[49] K. Wilson, K. Homan, and S. Emelianov, "Biomedical photoacoustics beyond thermal expansion using triggered nanodroplet vaporization for contrast-enhanced imaging," *Nat. Commun.,* vol. 3, p. 618, 2012.

[50] N. Rapoport, "Phase-shift, stimuli-responsive perfluorocarbon nanodroplets for drug delivery to cancer," *Wiley Interdiscipl. Rev. Nanomed. Nanobiotechnol.,* vol. 4, pp. 492-510, 2012.

[51] C.-Y. Lin and W. G. Pitt, "Acoustic Droplet Vaporization in Biology and Medicine," *BioMed Res. Int,,* vol. 2013, pp. 1-13, 2013.

[52] S. Lin, A. Shah, J. Hernández-Gil, A. Stanziola, B. I. Harriss, T. O. Matsunaga, *et al.*, "Optically and acoustically triggerable sub-micron phase-change contrast agents for enhanced photoacoustic and ultrasound imaging," *Photoacoustics,* vol. 6, pp. 26-36, 2017.

[53] D. Y. Santiesteban, D. S. Dumani, D. Profili, and S. Y. Emelianov, "Copper Sulfide Perfluorocarbon Nanodroplets as Clinically Relevant Photoacoustic/Ultrasound Imaging Agents," *Nano Lett.,* vol. 17, pp. 5984-5989, 2017.

[54] D. Psychoudakis, J. B. Fowlkes, J. L. Volakis, and P. L. Carson, "Potential of microbubbles for use as point targets in phase aberration correction," *IEEE Trans. Ultrason., Ferroelect., Freq. Control,* vol. 51, pp. 1639-1648, 2004.

[55] G. P. Luke, A. S. Hannah, and S. Y. Emelianov, "Super-resolution ultrasound imaging in vivo with transient laser-activated nanodroplets," *Nano Lett.,* 2016.

[56] H. Yoon, S. K. Yarmoska, A. S. Hannah, C. Yoon, K. A. Hallam, and S. Y. Emelianov, "Contrast-enhanced ultrasound imaging in vivo with laser-activated nanodroplets," *Med. Phys.,* vol. 44, pp. 3444-3449, 2017.

[57] H. Yoon, K. A. Hallam, C. Yoon, and S. Y. Emelianov, "Super-resolution imaging with ultrafast ultrasound imaging of optically triggered perfluorohexane nanodroplets," *IEEE Trans. Ultrason., Ferroelect., Freq. Control,* pp. 1-1, 2018.

[58] A. Carovac, F. Smajlovic, and D. Junuzovic, "Application of Ultrasound in Medicine," *Acta Inform. Med.,* vol. 19, pp. 168-171, 2011.

[59] M. L. Palmeri, D. Yufeng, N. C. Rouze, and K. R. Nightingale, "Dependence of shear wave spectral content on acoustic radiation force excitation duration and spatial beamwidth," in *2014 IEEE Int. Ultrasonics Symp. (IUS)*, 2014, pp. 1105-1108.

[60] M. Denis, M. Mehrmohammadi, P. Song, D. D. Meixner, R. T. Fazzio, S. Pruthi, *et al.*, "Comb-push ultrasound shear elastography of breast masses: initial results show promise," *PLoS ONE,* vol. 10, p. e0119398, 2015.

[61] M. L. Palmeri and K. R. Nightingale, "Acoustic radiation force-based elasticity imaging methods," *Interface Focus,* vol. 1, pp. 553-564, 2011.

[62] J. J. Dahl, G. F. Pinton, L. Mark, V. Agrawal, K. R. Nightingale, and G. E. Trahey, "A parallel tracking method for acoustic radiation force impulse imaging," *IEEE Trans. Ultrason. Ferroelectr. Freq. Control,* vol. 54, pp. 301-312, 2007.

[63] A. Manduca, D. S. Lake, S. A. Kruse, and R. L. Ehman, "Spatio-temporal directional filtering for improved inversion of MR elastography images," *Med. Image Anal.,* vol. 7, pp. 465-473, 2003.

[64] S. L. Lipman, N. C. Rouze, M. L. Palmeri, and K. R. Nightingale, "Evaluating the Improvement in Shear Wave Speed Image Quality Using Multidimensional Directional Filters in the Presence of Reflection Artifacts," *IEEE Trans. Ultrason., Ferroelect., Freq. Control,* vol. 63, pp. 1049-1063, 2016.

[65] T. Deffieux, J. L. Gennisson, J. Bercoff, and M. Tanter, "On the effects of reflected waves in transient shear wave elastography," *IEEE Trans. Ultrason. Ferroelectr. Freq. Control,* vol. 58, pp. 2032-2035, 2011.

[66] P. Song, M. W. Urban, A. Manduca, H. Zhao, J. F. Greenleaf, and S. Chen, "Comb-push ultrasound shear elastography (CUSE) with various ultrasound push beams," *IEEE Trans. Med. Imaging,* vol. 32, pp. 1435-1447, 2013.

[67] A. Nabavizadeh, S. Pengfei, C. Shigao, J. F. Greenleaf, and M. W. Urban, "Multi-source and multi-directional shear wave generation with intersecting steered ultrasound push beams," *IEEE Trans. Ultrason. Ferroelectr. Freq. Control,* vol. 62, pp. 647-662, 2015.

[68] P. Y. Barthez, R. Léveillé, and P. V. Scrivani, "Side lobes and grating lobes artifacts in ultrasound imaging," *Vet. Radiol. Ultrasound,* vol. 38, pp. 387-393, 1997.

[69] A. Austeng and S. Holm, "Sparse 2-D arrays for 3-D phased array imaging - design methods," *IEEE Trans. Ultrason., Ferroelect., Freq. Control,* vol. 49, pp. 1073-1086, 2002.

[70] C. Yoon, B. J. Kang, C. Lee, H. H. Kim, and K. K. Shung, "Multi-particle trapping and manipulation by a high-frequency array transducer," *Appl. Phys. Lett.,* vol. 105, p. 214103, 2014.

[71] J. A. Jensen and N. B. Svendsen, "Calculation of pressure fields from arbitrarily shaped, apodized, and excited ultrasound transducers," *IEEE Trans. Ultrason. Ferroelectr. Freq. Control,* vol. 39, pp. 262-267, 1992.

[72] J. A. Jensen, "Field: a program for simulating ultrasound systems," *Med. Biol. Eng. Comput.,* vol. 34, pp. 351-353, 1996.

[73] G. Montaldo, M. Tanter, J. Bercoff, N. Benech, and M. Fink, "Coherent plane-wave compounding for very high frame rate ultrasonography and transient elastography," *IEEE Trans. Ultrason. Ferroelectr. Freq. Control,* vol. 56, pp. 489-506, 2009.

[74] G. F. Pinton, J. J. Dahl, and G. E. Trahey, "Rapid tracking of small displacements with ultrasound," *IEEE Trans. Ultrason. Ferroelectr. Freq. Control,* vol. 53, pp. 1103-1117, 2006.

[75] T. Loupas, R. B. Peterson, and R. W. Gill, "Experimental evaluation of velocity and power estimation for ultrasound blood flow imaging, by means of a two-dimensional autocorrelation approach," *IEEE Trans. Ultrason. Ferroelectr. Freq. Control,* vol. 42, pp. 689-699, 1995.

[76] P. Song, A. Manduca, H. Zhao, M. W. Urban, J. F. Greenleaf, and S. Chen, "Fast shear compounding using robust 2-D shear wave speed calculation and multi-directional filtering," *Ultrasound Med. Biol.*, vol. 40, pp. 1343-1355, 2014.

[77] S. Bae, T.-K. Song, and J. H. Chang, "New shear wave velocity estimation using arrival time differences in orthogonal directions," in *2014 IEEE Int. Ultrasonics Symp. (IUS)*, 2014, pp. 1113-1116.

[78] M. Rao, Q. Chen, H. Shi, and T. Varghese, "Spatial-angular compounding for elastography using beam steering on linear array transducers," *Med. Phys.*, vol. 33, pp. 618-626, 2006.

[79] A. S. Hannah, "Optically-triggered nanodroplets for enhanced ultrasound and photoacoustic imaging," Ph.D. thesis, Biomedical Engineering, The University of Texas at Austin, Austin, TX, USA, 2015.

[80] FDA. (2008). *Guidance for Industry and FDA Staff Information for Manufacturers Seeking Marketing Clearance of Diagnostic Ultrasound Systems and Transducers*. Available: http://www.fda.gov/RegulatoryInformation/Guidances/ucm070856.htm

[81] N. C. Rouze, M. H. Wang, M. L. Palmeri, and K. R. Nightingale, "Parameters affecting the resolution and accuracy of 2-D quantitative shear wave images," *IEEE Trans. Ultrason. Ferroelectr. Freq. Control,* vol. 59, pp. 1729-1740, 2012.

[82] C. Yoon, B. J. Kang, C. Lee, H. H. Kim, and K. K. Shung, "Multi-particle trapping and manipulation by a high-frequency array transducer," *Appl. Phys. Lett.*, vol. 105, p. 214103, 2014.

[83] H. Yoon, G. P. Luke, and S. Y. Emelianov, "Impact of depth-dependent optical attenuation on wavelength selection for spectroscopic photoacoustic imaging," *Photoacoustics,* 2018.

[84] J. M. Brown and W. R. Wilson, "Exploiting tumour hypoxia in cancer treatment," *Nat. Rev. Cancer,* vol. 4, pp. 437-447, 2004.

[85] I. N. Fleming, R. Manavaki, P. J. Blower, C. West, K. J. Williams, A. L. Harris, *et al.*, "Imaging tumour hypoxia with positron emission tomography," *Br. J. Cancer*, vol. 112, pp. 238-250, 2015.

[86] X. Sun, G. Niu, N. Chan, B. Shen, and X. Chen, "Tumor Hypoxia Imaging," *Mol Imaging Biol*, vol. 13, pp. 399-410, 2011.

[87] A. Taruttis and V. Ntziachristos, "Advances in real-time multispectral optoacoustic imaging and its applications," *Nat. Photon.*, vol. 9, pp. 219-227, 2015.

[88] S. Y. Emelianov, P.-C. Li, and M. O'Donnell, "Photoacoustics for molecular imaging and therapy," *Physics today*, vol. 62, pp. 34-39, 2009.

[89] G. Luke, D. Yeager, and S. Emelianov, "Biomedical Applications of Photoacoustic Imaging with Exogenous Contrast Agents," *Ann. Biomed. Eng.*, vol. 40, pp. 422-437, 2012.

[90] S. Mallidi, T. Larson, J. Tam, P. P. Joshi, A. Karpiouk, K. Sokolov, *et al.*, "Multiwavelength Photoacoustic Imaging and Plasmon Resonance Coupling of Gold Nanoparticles for Selective Detection of Cancer," *Nano Lett.*, vol. 9, pp. 2825-2831, 2009.

[91] J. Yao, L. Wang, J.-M. Yang, K. I. Maslov, T. T. W. Wong, L. Li, *et al.*, "High-speed label-free functional photoacoustic microscopy of mouse brain in action," *Nat. Meth.*, vol. 12, p. 407, 2015.

[92] B. T. Cox, S. R. Arridge, and P. C. Beard, "Estimating chromophore distributions from multiwavelength photoacoustic images," *J. Opt. Soc. Am. A*, vol. 26, pp. 443-455, 2009.

[93] S. Tzoumas, N. C. Deliolanis, S. Morscher, and V. Ntziachristos, "Unmixing Molecular Agents From Absorbing Tissue in Multispectral Optoacoustic Tomography," *IEEE Trans. Med. Imag.*, vol. 33, pp. 48-60, 2014.

[94] C. Lutzweiler and D. Razansky, "Optoacoustic Imaging and Tomography: Reconstruction Approaches and Outstanding Challenges in Image Performance and Quantification," *Sensors*, vol. 13, 2013.

[95] B. Cox, J. G. Laufer, S. R. Arridge, and P. C. Beard, "Quantitative spectroscopic photoacoustic imaging: a review," *J. Biomed. Opt.*, vol. 17, pp. 0612021-06120222, 2012.

[96] S. Kim, Y.-S. Chen, G. P. Luke, and S. Y. Emelianov, "In vivo three-dimensional spectroscopic photoacoustic imaging for monitoring nanoparticle delivery," *Biomed. Opt. Express*, vol. 2, pp. 2540-2550, 2011.

[97] H. F. Zhang, K. Maslov, G. Stoica, and L. V. Wang, "Functional photoacoustic microscopy for high-resolution and noninvasive in vivo imaging," *Nat. Biotech.*, vol. 24, pp. 848-851, 2006.

[98] G. P. Luke and S. Y. Emelianov, "Optimization of in vivo spectroscopic photoacoustic imaging by smart optical wavelength selection," *Opt. Lett.*, vol. 39, pp. 2214-2217, 2014.

[99] G. P. Luke, S. Y. Nam, and S. Y. Emelianov, "Optical wavelength selection for improved spectroscopic photoacoustic imaging," *Photoacoustics*, vol. 1, pp. 36-42, 2013.

[100] A. Q. Bauer, R. E. Nothdurft, T. N. Erpelding, L. V. Wang, and J. P. Culver, "Quantitative photoacoustic imaging: correcting for heterogeneous light fluence distributions using diffuse optical tomography," *J. Biomed. Opt.*, vol. 16, p. 096016, 2011.

[101] J. C. Ranasinghesagara and R. J. Zemp, "Combined photoacoustic and oblique-incidence diffuse reflectance system for quantitative photoacoustic imaging in turbid media," 2010, p. 5.

[102] B. T. Cox, S. R. Arridge, K. P. Köstli, and P. C. Beard, "Two-dimensional quantitative photoacoustic image reconstruction of absorption distributions in scattering media by use of a simple iterative method," *Appl. Opt.*, vol. 45, pp. 1866-1875, 2006.

[103] J. Laufer, B. Cox, E. Zhang, and P. Beard, "Quantitative determination of chromophore concentrations from 2D photoacoustic images using a nonlinear model-based inversion scheme," *Appl. Opt.*, vol. 49, pp. 1219-1233, 2010.

[104] F. M. Brochu, J. Brunker, J. Joseph, M. R. Tomaszewski, S. Morscher, and S. E. Bohndiek, "Towards Quantitative Evaluation of Tissue Absorption Coefficients Using Light Fluence Correction in Optoacoustic Tomography," *IEEE Trans. Med. Imag.*, vol. 36, pp. 322-331, 2017.

[105] C. Zhu and Q. Liu, "Review of Monte Carlo modeling of light transport in tissues," *J. Biomed. Opt.*, vol. 18, pp. 050902-050902, 2013.

[106] S. Tzoumas, A. Nunes, I. Olefir, S. Stangl, P. Symvoulidis, S. Glasl, *et al.*, "Eigenspectra optoacoustic tomography achieves quantitative blood oxygenation imaging deep in tissues," *Nat. Commun.*, vol. 7, p. 12121, 2016.

[107] K. Thomas, G. Janek, and M.-H. Lena, "Context encoding enables machine learning-based quantitative photoacoustics," *J. Biomed. Opt.*, vol. 23, pp. 1-9, 2018.

[108] B. T. Cox, J. G. Laufer, and P. C. Beard, "The challenges for quantitative photoacoustic imaging," in *Proc. SPIE, Photons Plus Ultrasound: Imaging and Sensing*, 2009, pp. 717713-717713-9.

[109] S. L. Jacques, "Coupling 3D Monte Carlo light transport in optically heterogeneous tissues to photoacoustic signal generation," *Photoacoustics,* vol. 2, pp. 137-142, 2014.

[110] N. Keshava and J. F. Mustard, "Spectral unmixing," *IEEE Signal Process. Mag.,* vol. 19, pp. 44-57, 2002.

[111] T. Tarvainen, A. Pulkkinen, B. T. Cox, J. P. Kaipio, and S. R. Arridge, "Bayesian Image Reconstruction in Quantitative Photoacoustic Tomography," *IEEE Trans. Med. Imag.,* vol. 32, pp. 2287-2298, 2013.

[112] S. Tzoumas, A. Rosenthal, C. Lutzweiler, D. Razansky, and V. Ntziachristos, "Spatiospectral denoising framework for multispectral optoacoustic imaging based on sparse signal representation," *Med. Phys.,* vol. 41, p. 113301, 2016.

[113] J. Yao and L. V. Wang, "Sensitivity of photoacoustic microscopy," *Photoacoustics,* vol. 2, pp. 87-101, 2014.

[114] A. N. S. I. Inc. (2007, December 12). *American National Standard for Safe Use of Lasers*. Available: https://www.lia.org/PDF/Z136_1_s.pdf

[115] C. Yoon, J. Kang, S. Han, Y. Yoo, T.-K. Song, and J. H. Chang, "Enhancement of photoacoustic image quality by sound speed correction: ex vivo evaluation," *Opt. Express,* vol. 20, pp. 3082-3090, 2012.

[116] M. K. A. Singh, M. Jaeger, M. Frenz, and W. Steenbergen, "In vivo demonstration of reflection artifact reduction in photoacoustic imaging using synthetic aperture photoacoustic-guided focused ultrasound (PAFUSion)," *Biomed. Opt. Express,* vol. 7, pp. 2955-2972, 2016.

[117] R. L. Siegel, K. D. Miller, and A. Jemal, "Cancer statistics, 2015," *CA Cancer J. Clin.,* vol. 65, pp. 5-29, 2015.

[118] D. Spano, C. Heck, P. De Antonellis, G. Christofori, and M. Zollo, "Molecular networks that regulate cancer metastasis," *Semin. Cancer Biol.,* vol. 22, pp. 234-249, 2012.

[119] S. K. Somasundaram, D. W. Chicken, and M. R. S. Keshtgar, "Detection of the sentinel lymph node in breast cancer," *Br. Med. Bull.,* vol. 84, pp. 117-131, 2007.

[120] M. Ahmed, A. D. Purushotham, and M. Douek, "Novel techniques for sentinel lymph node biopsy in breast cancer: a systematic review," *Lancet Oncol.,* vol. 15, pp. e351-e362, 2014.

[121] V. M. Moncayo, J. N. Aarsvold, and N. P. Alazraki, "Lymphoscintigraphy and Sentinel Nodes," *J. Nucl. Med.,* vol. 56, pp. 901-907, 2015.

[122] V. J. L. Kuijs, M. Moossdorff, R. J. Schipper, R. G. H. Beets-Tan, E. M. Heuts, K. B. M. I. Keymeulen, *et al.*, "The role of MRI in axillary lymph node imaging in breast cancer patients: a systematic review," *Insights Imaging*, vol. 6, pp. 203-215, 2015.

[123] A. Garcia-Uribe, T. N. Erpelding, A. Krumholz, H. Ke, K. Maslov, C. Appleton, *et al.*, "Dual-Modality Photoacoustic and Ultrasound Imaging System for Noninvasive Sentinel Lymph Node Detection in Patients with Breast Cancer," *Sci. Rep.*, vol. 5, p. 15748, 2015.

[124] C. Tourasse, J. F. Dénier, A. Awada, A.-C. Gratadour, K. Nessah-Bousquet, and J. Gay, "Elastography in the assessment of sentinel lymph nodes prior to dissection," *Eur. J. Radiol.*, vol. 81, pp. 3154-3159, 2012.

[125] B. Singh, S. Ezziddin, H. Palmedo, M. Reinhardt, H. Strunk, T. Tüting, *et al.*, "Preoperative 18F-FDG-PET/CT imaging and sentinel node biopsy in the detection of regional lymph node metastases in malignant melanoma," *Melanoma Res.*, vol. 18, pp. 346-352, 2008.

[126] A. R. Sever, P. Mills, S. E. Jones, K. Cox, J. Weeks, D. Fish, *et al.*, "Preoperative Sentinel Node Identification With Ultrasound Using Microbubbles in Patients With Breast Cancer," *Am. J. Roentgenol.*, vol. 196, pp. 251-256, 2011.

[127] M. A. Swartz, "The physiology of the lymphatic system," *Adv. Drug Deliv. Rev.*, vol. 50, pp. 3-20, 2001.

[128] P. S. Sheeran, J. D. Rojas, C. Puett, J. Hjelmquist, C. B. Arena, and P. A. Dayton, "Contrast-Enhanced Ultrasound Imaging and in Vivo Circulatory Kinetics with Low-Boiling-Point Nanoscale Phase-Change Perfluorocarbon Agents," *Ultrasound Med. Biol.*, vol. 41, pp. 814-831, 2015.

[129] A. Hannah, G. Luke, K. Wilson, K. Homan, and S. Emelianov, "Indocyanine Green-Loaded Photoacoustic Nanodroplets: Dual Contrast Nanoconstructs for Enhanced Photoacoustic and Ultrasound Imaging," *ACS Nano*, vol. 8, pp. 250-259, 2014.

[130] E. Strohm, M. Rui, I. Gorelikov, N. Matsuura, and M. Kolios, "Vaporization of perfluorocarbon droplets using optical irradiation," *Biomed. Opt. Express*, vol. 2, pp. 1432-1442, 2011.

[131] N. Rapoport, K.-H. Nam, R. Gupta, Z. Gao, P. Mohan, A. Payne, *et al.*, "Ultrasound-mediated tumor imaging and nanotherapy using drug loaded, block copolymer stabilized perfluorocarbon nanoemulsions," *J. Control. Release*, vol. 153, pp. 4-15, 2011.

[132] R. Asami and K. Kawabata, "Repeatable vaporization of optically vaporizable perfluorocarbon droplets for photoacoustic contrast enhanced imaging," in *Proc. IEEE Int. Ultrason. Symp.*, 2012, pp. 1200-1203.

[133] A. S. Hannah, G. P. Luke, and S. Y. Emelianov, "Blinking Phase-Change Nanocapsules Enable Background-Free Ultrasound Imaging," *Theranostics,* vol. 6, pp. 1866-1876, 2016.

[134] K. Christensen-Jeffries, R. J. Browning, M. X. Tang, C. Dunsby, and R. J. Eckersley, "In Vivo Acoustic Super-Resolution and Super-Resolved Velocity Mapping Using Microbubbles," *IEEE Trans. Med. Imag.,* vol. 34, pp. 433-440, 2015.

[135] C. Errico, J. Pierre, S. Pezet, Y. Desailly, Z. Lenkei, O. Couture, *et al.*, "Ultrafast ultrasound localization microscopy for deep super-resolution vascular imaging," *Nature,* vol. 527, pp. 499-502, 2015.

[136] M. A. O'Reilly and K. Hynynen, "A super-resolution ultrasound method for brain vascular mapping," *Med. Phys.,* vol. 40, pp. 110701-n/a, 2013.

[137] O. Couture, S. Bannouf, G. Montaldo, J.-F. Aubry, M. Fink, and M. Tanter, "Ultrafast Imaging of Ultrasound Contrast Agents," *Ultrasound Med. Biol.,* vol. 35, pp. 1908-1916, 2009.

[138] Y. Desailly, O. Couture, M. Fink, and M. Tanter, "Sono-activated ultrasound localization microscopy," *Appl. Phys. Lett.,* vol. 103, p. 174107, 2013.

[139] F. Lin, S. E. Shelton, D. Espíndola, J. D. Rojas, G. Pinton, and P. A. Dayton, "3-D Ultrasound Localization Microscopy for Identifying Microvascular Morphology Features of Tumor Angiogenesis at a Resolution Beyond the Diffraction Limit of Conventional Ultrasound," *Theranostics,* vol. 7, pp. 196-204, 2017.

[140] J. Foiret, H. Zhang, T. Ilovitsh, L. Mahakian, S. Tam, and K. W. Ferrara, "Ultrasound localization microscopy to image and assess microvasculature in a rat kidney," *Sci. Rep.,* vol. 7, p. 13662, 2017.

[141] V. Hingot, C. Errico, M. Tanter, and O. Couture, "Subwavelength motion-correction for ultrafast ultrasound localization microscopy," *Ultrasonics,* vol. 77, pp. 17-21, 2017.

[142] P. Song, J. D. Trzasko, A. Manduca, R. Huang, R. Kadirvel, D. F. Kallmes, *et al.*, "Improved Super-Resolution Ultrasound Microvessel Imaging with Spatiotemporal Nonlocal Means Filtering and Bipartite Graph-Based Microbubble Tracking," *IEEE Trans. Ultrason., Ferroelect., Freq. Control,* vol. PP, pp. 1-1, 2017.

[143] F. Lin, J. K. Tsuruta, J. D. Rojas, and P. A. Dayton, "Optimizing Sensitivity of Ultrasound Contrast-Enhanced Super-Resolution Imaging by Tailoring Size Distribution of Microbubble Contrast Agent," *Ultrasound Med. Biol.,* vol. 43, pp. 2488-2493, 2017.

[144] D. Ghosh, F. Xiong, S. R. Sirsi, P. W. Shaul, R. F. Mattrey, and K. Hoyt, "Toward optimization of in vivo super-resolution ultrasound imaging using size-selected microbubble contrast agents," *Med. Phys.*, vol. 44, pp. 6304-6313, 2017.

[145] K. Christensen-Jeffries, S. Harput, J. Brown, P. N. T. Wells, P. Aljabar, C. Dunsby, *et al.*, "Microbubble Axial Localization Errors in Ultrasound Super-Resolution Imaging," *IEEE Trans. Ultrason., Ferroelect., Freq. Control*, vol. 64, pp. 1644-1654, 2017.

[146] K. Christensen-Jeffries, J. Brown, P. Aljabar, M. Tang, C. Dunsby, and R. J. Eckersley, "3-D In vitro acoustic super-resolution and super-resolved velocity mapping using microbubbles," *IEEE Trans. Ultrason., Ferroelect., Freq. Control*, vol. 64, pp. 1478-1486, 2017.

[147] J. Yu, X. Chen, F. S. Villanueva, and K. Kim, "Vaporization and recondensation dynamics of indocyanine green-loaded perfluoropentane droplets irradiated by a short pulse laser," *Appl. Phys. Lett.*, vol. 109, p. 243701, 2016.

[148] R. E. Thompson, D. R. Larson, and W. W. Webb, "Precise Nanometer Localization Analysis for Individual Fluorescent Probes," *Biophys. J.*, vol. 82, pp. 2775-2783, 2002.

[149] K. Zell, J. I. Sperl, M. W. Vogel, R. Niessner, and C. Haisch, "Acoustical properties of selected tissue phantom materials for ultrasound imaging," *Phys. Med. Biol*, vol. 52, p. N475, 2007.

[150] M. N. Iizuka, M. D. Sherar, and I. A. Vitkin, "Optical phantom materials for near infrared laser photocoagulation studies," *Lasers Surg. Med.*, vol. 25, pp. 159-169, 1999.

[151] H. Yoon and S. Emelianov, "Multispectral ultrafast ultrasound imaging: A versatile tool probing dynamic phase-change contrast agents," in *Ultrasonics Symposium (IUS), 2017 IEEE International*, 2017, pp. 1-1.

[152] D. S. Li, S. J. Yoon, I. Pelivanov, M. Frenz, M. O'Donnell, and L. D. Pozzo, "Polypyrrole-Coated Perfluorocarbon Nanoemulsions as a Sono-Photoacoustic Contrast Agent," *Nano Lett.*, vol. 17, pp. 6184-6194, 2017.

[153] H. Yoon and S. Emelianov, "Combined multi-wavelength photoacoustic and plane-wave ultrasound imaging for probing dynamic phase-change contrast agents," *IEEE Trans. Biomed. Eng.*, pp. 1-1, 2018.

[154] U. Prabhakar, H. Maeda, R. K. Jain, E. M. Sevick-Muraca, W. Zamboni, O. C. Farokhzad, *et al.*, "Challenges and Key Considerations of the Enhanced Permeability and Retention Effect for Nanomedicine Drug Delivery in Oncology," *Cancer Res.*, vol. 73, pp. 2412-2417, 2013.

[155] T. O. Matsunaga, P. S. Sheeran, S. Luois, J. E. Streeter, L. B. Mullin, B. Banerjee, *et al.*, "Phase-Change Nanoparticles Using Highly Volatile Perfluorocarbons: Toward a Platform for Extravascular Ultrasound Imaging," *Theranostics,* vol. 2, pp. 1185-1198, 2012.

[156] D. Santiesteban, K. Hallam, S. Yarmoska, and S. Emelianov, "Multicolor perfluorocarbon nanodroplets for multiplexed ultrasound and photoacoustic imaging," in *Ultrasonics Symposium (IUS), 2017 IEEE International*, 2017, pp. 1-1.

[157] L. J. Rich and M. Seshadri, "Photoacoustic monitoring of tumor and normal tissue response to radiation," *Sci. Rep.,* vol. 6, p. 21237, 2016.

[158] H. Yoon and S. Y. Emelianov, "Combined multi-wavelength photoacoustic and plane-wave ultrasound imaging for probing dynamic phase-change contrast agents."

[159] S. Y. Emelianov, S. R. Aglyamov, J. Shah, S. Sethuraman, W. G. Scott, R. Schmitt, *et al.*, "Combined ultrasound, optoacoustic, and elasticity imaging," in *Proc. SPIE, Photons Plus Ultrasound: Imaging and Sensing*, 2004, p. 12.

[160] M. N. Nguyen, X. Ding, J. Yu, D. Park, F. Yu, and K. Kim, "Tri-modality Ultrasound Imaging System: Design and Phantom Experiment Results," in *Proc. IEEE Int. Ultrason. Symp.*, 2014, pp. 325-328.

[161] T. Loupas, R. B. Peterson, and R. W. Gill, "Experimental evaluation of velocity and power estimation for ultrasound blood flow imaging, by means of a two-dimensional autocorrelation approach," *IEEE Trans. Ultrason., Ferroelect., Freq. Control,* vol. 42, pp. 689-699, 1995.

[162] N. C. Rouze, M. H. Wang, M. L. Palmeri, and K. R. Nightingale, "Parameters affecting the resolution and accuracy of 2-D quantitative shear wave images," *IEEE Trans. Ultrason., Ferroelect., Freq. Control,* vol. 59, pp. 1729-1740, 2012.

[163] V. Ntziachristos, "Going deeper than microscopy: the optical imaging frontier in biology," *Nat. Meth.,* vol. 7, p. 603, 2010.

[164] H. Yoon, G. Luke P., and S. Emelianov Y., "Impact of depth-dependent optical attenuation on wavelength selection for spectroscopic photoacoustic imaging," *Photoacoustics,* 2018.

[165] M. L. Palmeri and K. R. Nightingale, "What challenges must be overcome before ultrasound elasticity imaging is ready for the clinic?," *Imaging in medicine,* vol. 3, pp. 433-444, 2011.

[166] K. D. Burman and L. Wartofsky, "Thyroid Nodules," *N. Engl. J. Med.,* vol. 373, pp. 2347-2356, 2015.

[167] M. C. Frates, C. B. Benson, J. W. Charboneau, E. S. Cibas, O. H. Clark, B. G. Coleman, *et al.*, "Management of Thyroid Nodules Detected at US: Society of Radiologists in Ultrasound Consensus Conference Statement," *Radiology*, vol. 237, pp. 794-800, 2005.